Simulating Baryte Nucleation and Crystallisation in Non-Stoichiometric Conditions: Applications of CrystalGrower, A Morphological Study

Robin Colbey

Earth Structure and Dynamics

Utrecht University

Master's Thesis

Dr. Mariette Wolthers, Dr. Paul Mason, MSc Sergej Seepma, Dr. Adam Hill[1]

23rd October 2020

30 ECTS

[1] Affiliation: Centre for Nanoporous Materials, The University of Manchester.

Abstract

The research questions asked were: What is the morphology of baryte synthesised in different laboratory concentrations and supersaturations? How accurately does CG simulate these morphologies? Can these simulations or morphologies constrain the depositional environment of Archean baryte?

Simulation software, CrystalGrower (CG), programmed to simulate growth of crystalline material has been developed at the Centre for Nanoporous Materials at the University of Manchester. To our knowledge, this is the first paper written for Utrecht University that involves CG. As well as finding an application for CG, this project has also involved nucleating and crystalising baryte at different concentrations and stoichiometries, using different reagents, in batch laboratory setups to compare the morphologies between simulated baryte and laboratory synthesised baryte. Experimenting with stoichiometry in a laboratory setting may also lead to constraints on Archean baryte deposits from 3.5 – 3.2 Ga as previous research shows the atmosphere was relatively depleted in Oxygen ($<10^{-5}$ Present Atmospheric Level) (Pavlov & Kasting, 2002), resulting in reducing conditions with low sulphate concentrations (<10 μM) (Busigny et al., 2017). Whilst comparing Archean baryte to simulated baryte is difficult for a variety of reasons, if more refinement could be carried out regarding CG and more constraints could be placed on the depositional environments of Archean baryte then future research could include CG in a variety of research regarding other salts such as other sulphates, carbonates, sulphides etc. The applications of CG could be extensive, but more background information regarding the interactions between barium and sulphate is necessary.

Simulating Baryte Growth in Non-Stoichiometric Conditions: Applications of Crystal Grower, A Morphological Study

1. Introduction

Baryte ($BaSO_4$) is a mineral with important commercial and environmental purposes. Due to its high specific gravity (4.48 g/cm^3) (Hanor, 2000) and low solubility product at ambient conditions (1.0842×10^{-10}) (Monnin & Galinier, 1988) it is an important salt in the petroleum extraction industry. Baryte is used in drilling muds, to maintain hole pressure above formation pressure and let sediment rise to the surface (Macdonald, 1982). Baryte can also become a type of scale, especially during marine petroleum recovery as two different water compositions mix. Sea water containing SO_4^{2-} and sub-surface brine containing Ba^{2+} can result in a solution supersaturated with respect to baryte (Risthaus et al., 2001). Additionally, Ba^{2+}, Sr^{2+} and Ra^{2+} have a similar atomic radius thus form a solid solution of $Ba_{1-X-Y}Ra_XSr_YSO_4$, immobilising radioactive isotopes such as ^{226}Ra and ^{210}Pb, making baryte an important mineral in the radioactive waste disposal industry (Martin & Akber, 1999, Uchida et al., 2012).

Beyond the commercial and environmental importance, baryte is also of geological importance, especially during the Archean eon around 3.5-3.2 Ga. The environment in which Archean baryte crystallised is thought to have been very different compared to recent baryte deposits. In the Archean, atmospheric O_2 was likely $<10^{-5}$ Present Atmospheric Level (Pavlov & Kasting, 2002), resulting in an abundance of reduced sulphur species (Busigny et al., 2017). Habicht et al., 2002, suggested an Archean sea water sulphate concentration of <200 µM, much lower than "modern" oceans, therefore the observation of Archean baryte is unusual. Hypotheses of Archean baryte formation includes the formation of pools of Ba^{2+} enriched fluids which extruded through terrestrial fissures to reach the surface (Lowe et al., 2019), the source of barium possibly being Ba-feldspars which underwent metasomatism to release Ba^{2+} into a brine solution (Nabhan et al., 2020). Due to intense volcanism at the time the atmosphere was enriched with SO_2 compared to the "modern" atmosphere. This gas then underwent photolytic reactions

to form atmospheric H_2SO_4 which precipitated into the Ba^{2+} rich pools, crystallising baryte (Lowe et al., 2019). Alternatively, Ba^{2+} enriched fluids were released into shallow marine environments from sub-surface brines and mixed with SO_4-containg, but limited, oceans (Busigny et al., 2017). Therefore, understanding the morphology of baryte in Ba^{2+} rich, SO_4^{2-} limiting conditions may provide possible constraints regarding the depositional environment.

The morphology of baryte in non-stoichiometric conditions has been analysed by previous master's students David Riedinger and Annet Baken by using scanning electron microscopy (SEM). This paper uses the term supersaturation ratio or Ω to convert the supersaturation index (SI) to a linear scale. Where SI and Ω are:

Equation 1

$$\mathrm{SI} = \log\left(\frac{\mathrm{IAP}}{\mathrm{K_{SP}}}\right)$$

Equation 2

$$\Omega = 10^{\mathrm{SI}} = \frac{\mathrm{IAP}}{\mathrm{K_{SP}}}$$

Where IAP is the ion activity product calculated by VMINTEQ and K_{SP} is the solubility product at ambient conditions, previously mentioned. Another term used throughout this paper is Δμ. This is measured in kcal/mol rather than kJ/mol and will be discussed in section 2.2.

Baken's results (Figure 1) show that at low Ω baryte develops a (210) face as the ratio of Ba^{2+}:SO_4^{2-} (r) increases as well as becoming more elongated and thinner. These experiments were carried out as a titration so continually grew crystals for a long period of time.

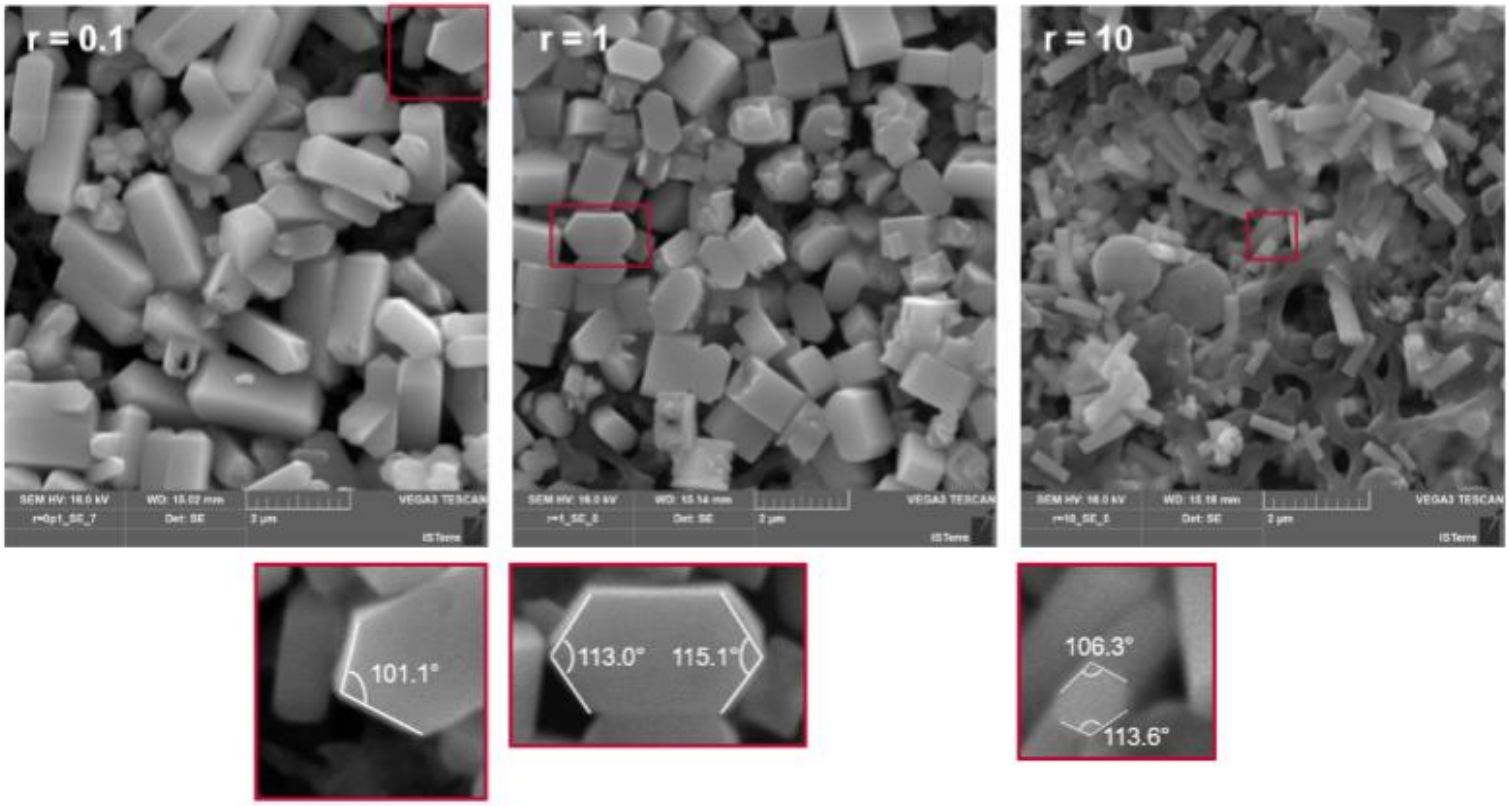

Figure 1: SEM images of baryte crystals. The scale shows that 1 crystal is approximately 2µm wide along the (001) face. Images were made by Annet Baken. Ω varies slightly throughout each ratio; Ω = ~200.

Riedinger. (2020) shows that at high Ω (500) baryte grows rapidly, regardless of the ratio. After 3 hours the solution reached equilibrium (Figure 2). r = 10 showed a similar morphology of the (001) and (210) faces to Baken's images however, when r < 1 the morphology was more different and not characteristic of what is observed in Archean baryte deposits (Lowe et al., 2019).

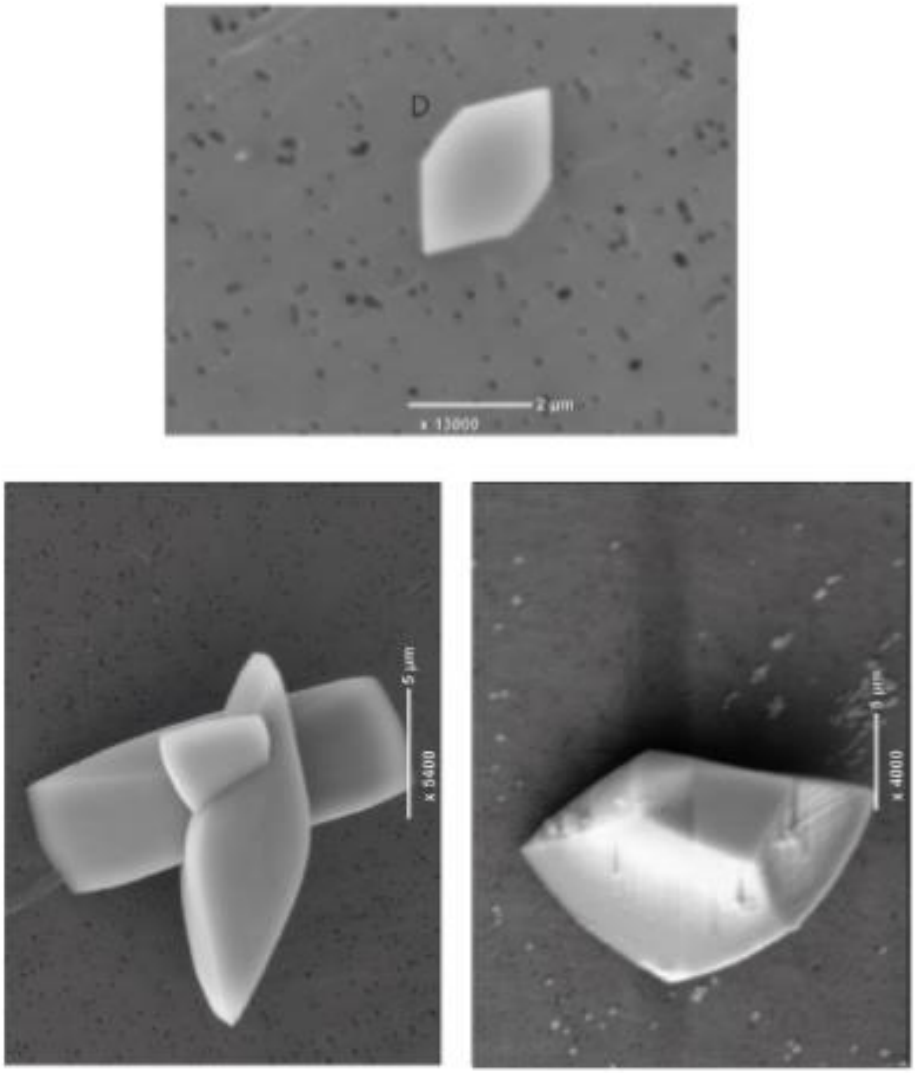

Figure 2: SEM images of Ω=500. The scale shows crystals varying between 2 µm in diameter to over 5 µm. r=10 (upper), r=0.01 (lower right) and r=0.1 (lower left). Images were edited from Riedinger. (2020).

This report will simulate baryte morphology in stoichiometric and non-stoichiometric environments using crystal simulation software: Crystal Grower (CG). This report will answer the following questions: What is the morphology of baryte when grown in these laboratory conditions? How accurately does CG simulate these baryte morphologies? Using Archean baryte as an example, what further developments could be made to apply CG to natural nucleation and crystallisation?

To our knowledge, no published documents associated with Utrecht University exist that include CG simulations, therefore the accuracy of CG will be explored. These simulations will be compared to SEM

images of laboratory synthesised baryte, also in an NaCl, KCl or $NaNO_3$ matrix to discuss the impact of different electrolytes and whether CG can replicate these baryte morphologies.

This project discusses the accuracy of CG, allows us to better understand the implications of non-stoichiometric environments on baryte morphology and potentially constrain baryte formation during the Archean era.

2. Background

2.1. Geological Background

The oldest deposits of baryte are dated back to the Archean eon between 3.54-3.20 Ga. The depositional environment at the time was notably different from modern depositional environments of baryte which contain excess SO_4^{2-} rather than Ba^{2+} (Gwiazda et al., 2019). Whilst SO_4^{2-} abundance was likely lower during the Archean, local excesses may have occurred due to ocean stratification or around volcanic activity (Busigny et al., 2017). Archean baryte outcrops occur in cratons across the globe, including the Barberton Greenstone Belt in South Africa (Lowe et al., 2019), the North Pole Dome in Western Australia (Van Kranendonk & Pirajno, 2004) and Ghattihosahalli Schist Belt, Dharwar Craton, India (Devaraju et al., 1999).

2.1.1. South Africa

The Barberton Greenstone Belt (BGB) is located at the border between South Africa and Eswatini, formerly known as Swaziland. Orientated SW-NE, the BGB is composed of three lithostratigraphic groups, the Onverwacht Group succeeded by the Fig Tree Group and then the Moodies Group. At the base of the BGB, the Onverwacht Group is largely composed of igneous rock with varying mafic, ultramafic and felsic plutonic rock dated from ~3.5 to ~3.4 Ga split into three formations: Theespruit, the oldest, is largely felsic and the only baryte-containing formation in the Onverwacht group, followed stratigraphically by Komati and Hooggenoeg which are more mafic to ultramafic (de Donde & de Wit, 1994). The Theespruit Formation contains a baryte deposit up to 12 m thick and dated at slightly more than 3.5 Ga (Roerdink et al., 2016).

The Fig Tree Group is where most Archean baryte is observed. Baryte deposits are constrained in this formation to ~3.26-3.23 Ga (Lowe et al., 2019). Uplift at the start of the Fig Tree Group formation resulted in the deposition of felsic rock, banded iron formations (BIFs) and eroded Onverwacht lithologies

first. Later, sedimentary rocks including greywackes, fine sandstones and shales were deposited. It is these deposits which contain baryte. (de Ronde & De Wit, 1994).

Above the Fig Tree Group is the Moodies Group. Like the Fig Tree Group, the Moodies Group is sedimentary consisting of conglomerates, clastic sandstones, and other sediment from the previously eroded Onverwacht Group. The Moodies Group also contains baryte in the form of nodules varying from 5 to 50 μm in diameter (Nabhan et al., 2020).

2.1.2. Australia

Whilst several Archean shields exist in Australia, only the Pilbara Craton contains primary baryte that was deposited during the Archean and not due to later weathering events (Anand & Paine, 2002, Schlegel et al., 2018). The North Pole Dome in Western Australia is where baryte deposits are located. The North Pole Dome is part of a halo surrounding multiple granitoid domes (Nijman & Valkering, 1998). These halos exhibit greenschist facies like the Barberton Greenstone Belt. The North Pole is a small batholith in the centre of the dome, around which, three grouped lithologies are identified between the North Pole batholith, Shaw batholith to the South and Carlindi to the North West.

The oldest group is the meso-Archean Warrawoona Group dated between ~3.5 to ~3.2 Ga. This group contains the baryte deposits, chert, and sandstone. Late Archean deposits, dated from ~3.3 to ~2.8 Ga, are identified as the Gorge Creek Group, consisting of chert, BIFs, siliclastic sediment and basalt (Nijman & Valkering, 1998).

The Fortescue Group consists of a basalt basement which deposited first, followed by tuff deposits and silt/clay laminations as well as sandstones and cherts (Macfarlane et al., 1994).

2.1.3. India

A greenstone belt is again the source of Archean baryte in India. The Dharwar Craton is divided into two domains, the younger East Dharwar Craton (EWC) and older West Dharwar Craton (WDC). Between these two sub-cratons, an area of mixing between the older and younger tonalite-trondhjemite-

granodiorite (TTG) basement rock occurs (Kunugiza et al., 1996). Neither the younger EDC nor the area of mixed TTG exhibits baryte deposits (Mukherjee et al., 2018). Only the WDC contains baryte deposits, however this sub-craton can be further split into two Groups: The oldest Sargur Group, ~3.25 to ~3.13 Ga (Basavarajappa et al., 2017) to the South and youngest Dharwar Group, ~2.91 to ~2.67 Ga, to the North (Jayandanda et al., 2016). Each defined group has again different tonalite-trondhjemite-granodiorite (TTG) basement rock (Kunugiza et al., 1996). Only the Sargur group consists of baryte deposits and is identified in the Eastern part of the WDC. The Sargur Group consists of a volcanic-sedimentary sequence including komatiites, amphibolites, quartzites and baryte (Basavarajappa et al., 2017) with TTG intrusions occurring after initial deposition around 2.96 Ga. The Dharwar Craton itself is overlain by the Deccan Traps to the North to the Granulite Terrain in the South (Muller et al., 2017).

2.2. CrystalGrower (CG) Background

CrystalGrower (CG) is a 3D growth simulator that was originally developed by Prof. Michael Anderson and his team, at the Centre for Nanoporous Materials, University of Manchester, UK, to simulate zeolites. However, CG has been recently adapted to simulate more general crystal structures including salts (Anderson et al., 2017). The programme relies on a kinetic Monte Carlo approach and calculates the probability of ions either attaching to (Equation 3) or detaching from (Equation 4) the surface of a mineral:

Equation 3

$$\mathrm{P}_{\mathrm{Site}}^{\mathrm{GROWTH}} = \exp\left(-0.5\frac{\Delta_{\mathrm{cry}}\mathrm{G}}{\mathrm{k_B T}} + 0.5\frac{\Delta\mu}{\mathrm{k_B T}}\right)$$

Equation 4

$$\mathrm{P}_{\mathrm{Site}}^{\mathrm{DISSOLUTION}} = \exp\left(+0.5\frac{\Delta_{\mathrm{cry}}\mathrm{G}}{\mathrm{k_B T}} - 0.5\frac{\Delta\mu}{\mathrm{k_B T}}\right)$$

Where P is the probability of growth or dissolution at a specific site on the surface of the simulated crystal (Anderson et al., 2017). This probability of growth or dissolution is calculated at each iteration, the number of which is determined by the user. $\Delta_{cry}G$ is the Gibbs free energy of crystallisation or the sum of the energy cost to desolvate a Ba^{2+} ion and the energy gained by attaching to an SO_4^{2-} neighbour in the

crystal and vice versa. Δμ is the supersaturation (kcal/mol), requiring conversion from kJ to kcal, k_BT represents the Boltzmann constant (k_B in kcal) multiplied by the temperature of the system in kelvin. These equations show that if the supersaturation exceeds Gibbs free energy of crystallisation then the probability of growth exceeds the probability of dissolution.

Calculating Gibbs Free Energy requires calculating each component of baryte separately, then adding them, assuming ideal gas behaviour:

Equation 5

$$\Delta_{cry}G_{Ba} + \Delta_{cry}G_{SO4} = T\Delta_{fus}S - RTLn(Ksp_{BaSO4})$$

Where $\Delta_{fus}S$ is the entropy of fusion of baryte. $\Delta_{fus}S$ is multiplied by temperature (in Kelvin) to convert the $\Delta_{fus}S$ unit (J/mol K) to the $\Delta_{cry}G$ unit (kJ/mol), or in the case of CG, kcal/mol. $T\Delta_{fus}S$ is the entropy change required to effectively "freeze" the isolated, fully solvated unit cell of baryte in the solid state (nucleation). $RTLn(Ksp_{BaSO4})$ represents the entropy cost of isolating a fully solvated ion and attaching it to the unit cell (crystallisation). Ksp is the solubility product constant of baryte, calculated by:

Equation 6

$$K_{SP} = \frac{[Ba^{2+}]_{eq} \times [SO_4{}^{2-}]_{eq}}{[BaSO_4]}$$

Where Ksp is an equilibrium constant between the precipitation and dissolution of baryte. When $[Ba^{2+}]*[SO_4^{2-}]$ exceeds the solubility product constant (~$1.08*10^{-10}$), baryte will precipitate. If the IAP does not exceed Ksp then precipitation will not occur.

Equation 5 is represented in Figure 3 which shows the energetic input required to simulate baryte precipitation conditions in CG. The $\Delta_{cry}G_{Ba/SO4}$ is shown in blue, the total Gibbs Free Energy is shown as the red dotted line, this is also the sum of $-RTLn(Ksp_{BaSO4}) + T\Delta_{fus}S$. Each step increase in $\Delta_{cry}G_{Ba/SO4}$ represents the energy required to replace a connection with a counterion with a connection to the solvent. A kink site, as described by Kossel (1927), is in equilibrium with the solid and solution phase therfore, all energy

levels below this site are likely to grow whilst all sites above this site are likely to dissolve. Δμ is then required to push the reaction towards growth on the kink site. The higher the Δμ the more likely growth will occur, and less likely dissolution will occur.

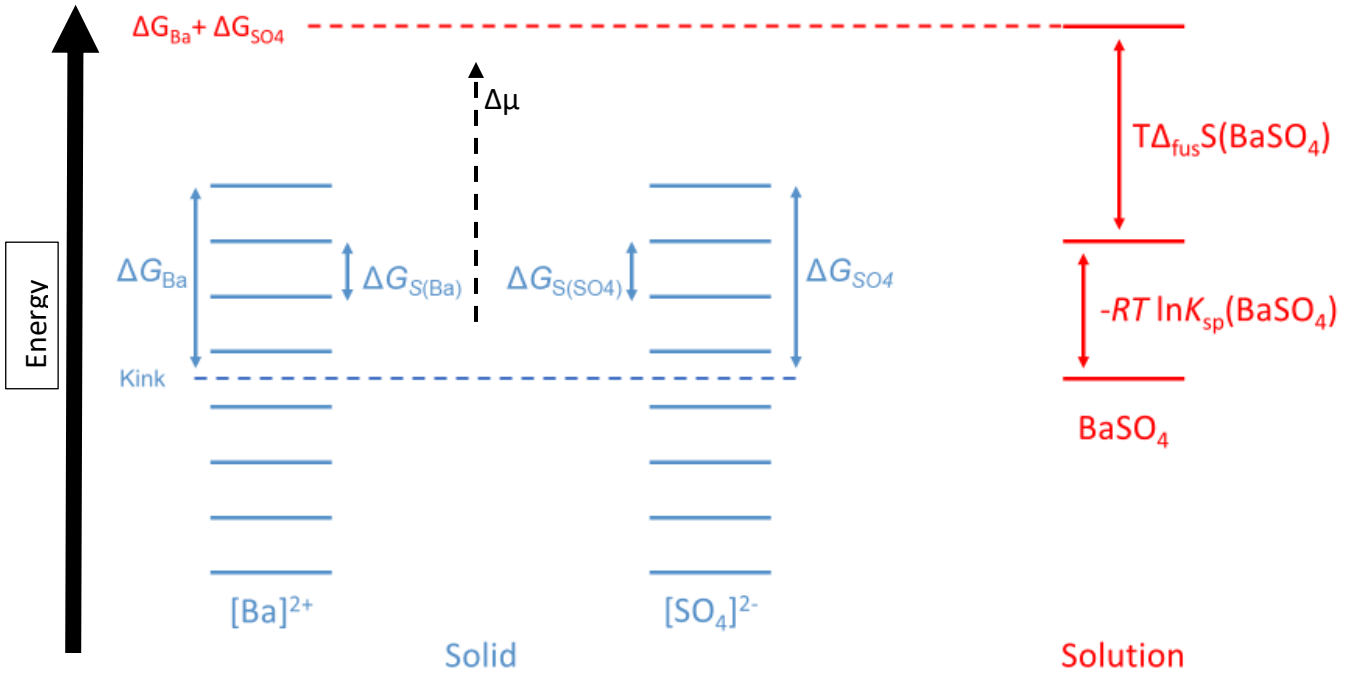

Figure 3: Energy diagram showing the enthalpic term of ΔG_s (blue) and the entropic term of ΔG_s (red) and Δμ (black). The enthalpy diagram shows the amount of energy required to attach or detach an ion to the unit cell whilst the entropy diagram shows the steps from a free ion in solution, to a fully solvated, isolated ion in solution to a fully solvated isolated ion in a solid. The dashed "kink" line represents the step where dissolution is as likely to occur as growth if Δμ = 0. Image taken from A. Hill, Personal Communication, August 29, 2020.

CG calculates $\Delta_{cry}G$ in terms of kcal/mol. The final value acquired for total $\Delta_{cry}G$ was ~15 kcal/mol. To calculate this value, firstly the $\Delta_{fus}S$ was calculated by:

Equation 7

$$\Delta_{fus}S = \frac{\Delta_{fus}H}{T_m}$$

Where $\Delta_{fus}H$ is the enthalpy of fusion of baryte, 40 kJ/mol or 9.56 kcal/mol (Haynes et al., 2017), T_m is the melting temperature of baryte, 1853.15 K (Haynes et al., 2017). Officially, $\Delta_{mixing}S$ is added to $\Delta_{fus}S$, increase the total $\Delta_{fus}S$. However, $\Delta_{mixing}S$ is negligible (<0.04 kcal/mol) compared to $\Delta_{fus}S$ so was not included. When Equation 7 is multiplied by the temperature of the system (T_s), which is approximately

294.15 K, $T_s\Delta_{fus}S$ is approximately 6.349 kJ/mol or 1.518 kcal/mol. This value was then added to the value -RTLn(Ksp) (~56.133 kJ/mol or 13.422 kcal/mol) to make ~15 kcal/mol. This is therefore the energy difference between the kink site and $\Delta_{cry}G_{Ba}$+ $\Delta_{cry}G_{SO4}$. Baryte was partitioned in ToposPro (Figure 4) by Dr. Adam Hill, showing the interactions between one Ba^{2+} in the bulk crystal and seven SO_4^{2-} which shows a coordination number of 12 due to five SO_4^{2-} interactions bonding with two oxygen atoms and two SO_4^{2-} interactions bonding with one oxygen atom (Jacobsen et al., 1998). These seven interactions were classified into "types" based on symmetry, where interaction types 2 and 3 occurred twice, making five different interaction types. Interaction types 1, 2 and 3 showed that two oxygen atoms originating from the same sulphate ion were bonded to a central barium whilst interaction types 4 and 5 showed one oxygen-barium bond. These interaction types can be described as bidentate and monodentate, respectively.

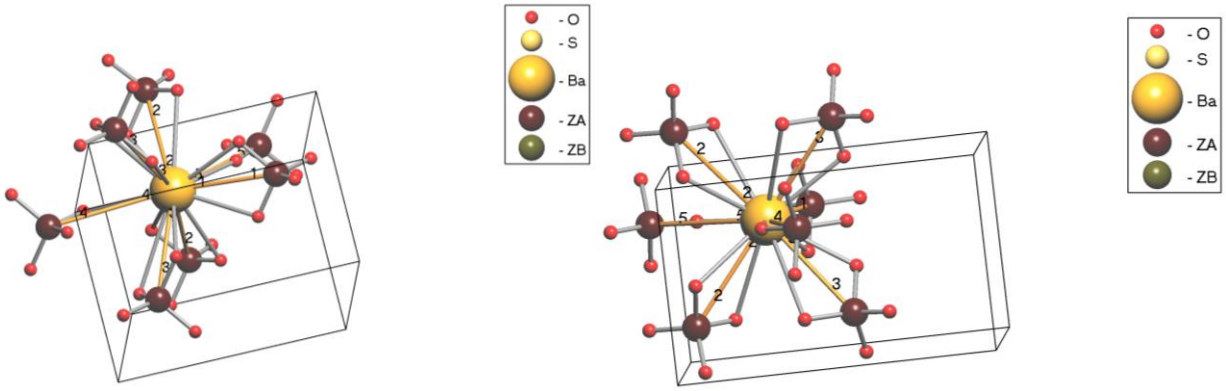

Figure 4: A single unit cell of baryte as modelled in ToposPro. Numbers represent different interaction types. Yellow = Ba, dark red = S, red = O, grey bonds are electronic between Ba and O, orange bonds are interactions between Ba and S. Images were produced by Dr. Adam Hill.

2.3. Defining Experimental Conditions for CG Simulations

Δμ represents the driving force or degree of supersaturation and can be calculated by:

Equation 8

$$\Delta\mu = \mathrm{RTln}\left(\frac{\mathrm{IAP}}{\mathrm{K_{SP}}}\right)$$

Where IAP is the ion activity product or $\{Ba^{2+}\}$ * $\{SO_4^{2-}\}$. To calculate the individual activities of barium and sulphate, the K_{SP} is multiplied by the saturation ratio (Ω) which is equivalent to:

Equation 9

$$\exp(\frac{\Delta\mu}{RT}) = \Omega$$

Equation 10

$$\Omega * K_{SP} = IAP$$

For stoichiometric systems:

Equation 11

$$\{Ba^{2+}\} = \{SO_4^{2-}\} = \sqrt{(\Omega * K_{SP})} = \sqrt{K_{SP} * e^{\Delta\mu/RT}}$$

This equation defines Δμ and Ω by the IAP calculated in VMINTEQ.

Calculating non-stoichiometric conditions in CG can be achieved by changing the initial Δμ of each component in a unit cell. This means that increasing Δμ of one ion requires a decrease of Δμ for the other component, resulting in a Δμ for sulphate and a Δμ for barium.

Where r > 1:

Equation 12

$$\Delta\mu_{SO4} = RT\ln\left(\frac{\{SO_4^{2-}\}^{2}}{K_{SP}}\right)$$

This calculates the Δμ of sulphate. Calculating the Δμ excess of Ba^{2+} is more complicated. The non-stoichiometric conditions calculated, shift the initial activities a certain amount, resulting in:

Equation 13

$$\{Ba^{2+}\}_{equilibrium} = \{Ba^{2+}\}_{initial} - x$$

$$\{SO_4^{2-}\}_{equilibrium} = \{SO_4^{2-}\}_{initial} - x$$

Where x represents the shift in activity due to the non-stoichiometric conditions. This is easily represented by a chemical reaction: $Ba^{2+} + SO_4^{2-} \rightarrow BaSO_4$. Increasing the concentration of one ion results in an excess of that ion: $Ba^{2+}_{excess} + SO_4^{2-} \rightarrow BaSO_4 + Ba^{2+}_{excess\text{-}consumed}$. Whilst the solubility of $BaSO_4$ does not change ($K_{SP} = \{Ba^{2+}\}_{equilibrium} * \{SO_4^{2-}\}_{equilibrium}$, the concentration of Ba^{2+} at equilibrium does. This excess is

also the difference between the starting Δμ of $\{Ba^{2+}\}$ and $\{SO_4^{2-}\}$. This results in Ksp = $(\{Ba^{2+}\}_{initial} - x)*(\{SO_4^{2-}\}_{initial} - x)$.

Calculating this excess Δμ of barium is achieved by:

Equation 14

$$\Delta\mu_{Barium} = RT\ln\left(\frac{\{Ba^{2+}\}_{initial} - x}{\{SO_4^{2-}\}_{initial} - x}\right)$$

Solving x requires a quadratic equation by taking Ksp = $(\{Ba^{2+}\}_{initial} - x)*(\{SO_4^{2-}\}_{initial} - x)$:

Equation 15

$$0 = x^2 - x(\{Ba^{2+}\}_{initial} + \{SO_4^{2-}\}_{initial}) + (\{Ba^{2+}\}_{initial} * \{SO_4^{2-}\}_{initial} - K_{SP})$$

Resulting in the equation:

Equation 16

$$x_{1,2} = \frac{-(\{Ba^{2+}\} + \{SO_4^{2-}\}) \pm \sqrt{(\{Ba^{2+}\} + \{SO_4^{2-}\})^2 - 4 * 1 * (\{Ba^{2+}\} * \{SO_4^{2-}\} - K_{SP})}}{2}$$

Whilst technically, this results in two values of x, only one value was used to calculate $\{Ba^{2+}\}_{equilibrium}$ and $\{SO_4^{2-}\}_{equilibrium}$. This is because $\{Ba^{2+}\}_{initial} - x_1 = -\{Ba^{2+}\}$; which cannot exist. Therefore, $\{Ba^{2+}\}_{initial} - x_2$ must also apply to $\{SO_4^{2-}\}$. Once these values are calculated, $\Delta\mu_{Barium}$ can be calculated. The results are shown in section 4.3.

Where r < 1 the process is the same but Ba^{2+} is the ion with a lower Δμ:

Equation 17

$$\Delta\mu_{Barium} = RT\ln\left(\frac{\{Ba^{2+}\}^2}{K_{SP}}\right)$$

2.3.1. CG Programming

The version of CG used for simulations relied on a command line interface rather than graphical user interface. This meant that editing the simulated environment required manual manipulation of parameters by accessing .txt files which were read by the command prompt. Firstly, the input data was edited to provide an accurate ΔG_s = 15 kcal/mol in molecular.txt whilst initial Δμ, number of iterations and

temperature were set in input.txt. Then the CG Application was run where excess Δμ (non-stoichiometric conditions) were incorporated. After the application ran, several output files were created which included any changes in Δμ, the size of each identified lattice vector in nm and a simulation output file or .XYZ file. This was read by the CG Visualiser (CGV) to simulate the results of the CG application. CGV also created .bmp files which could be opened as images.

2.3.1.1. input Data

2.3.1.1.1. *input.txt.* The input.txt file contained parameters that define the system in which crystal growth will be simulated, for example there were the options to add a screw dislocation or poison the system by introducing an inhibitor of crystallisation. This text file allowed for the input of the system temperature in Celsius, the number of times an ion attached or detached (iterations) and option to calculate the distances between faces and visualise the faces of a baryte crystal. The text file also allowed input for a starting Δμ and if any ion is in excess compared to the other. Pre-programmed Δμ pathways were available in CG determining the value of Δμ, the number of iterations at a given Δμ and the number of iterations to allow the simulated environment to reach equilibrium. There were seven Δμ pathways or "growth modes" designed to replicate different experimental setups (Figure 5). When modelling the morphology at non-stoichiometric conditions, growth modes 2, 3, 5 and 6 most closely represented laboratory experiments. Modes 2 and 5 represented titration experiment, where the concentration level of ions in solution is kept constant. Mode 5 allows the user to define two periods of different Δμ. This mode was designed to overcome the initial energy barrier for nucleation and then allowing the crystal to grow at a lower Δμ once the critical size had been succeeded. Modes 3 and 6 resembled batch experiments where excess ions would crystallise, resulting in a drop in degree of supersaturation and ultimately reaching equilibrium. Modes 3 and 6 differ in the same way to modes 2 and 5, respectively. The other modes were not used to simulate baryte morphology as these modes do not accurately represent laboratory synthesis or do not exceed the initial energy barrier for crystallisation.

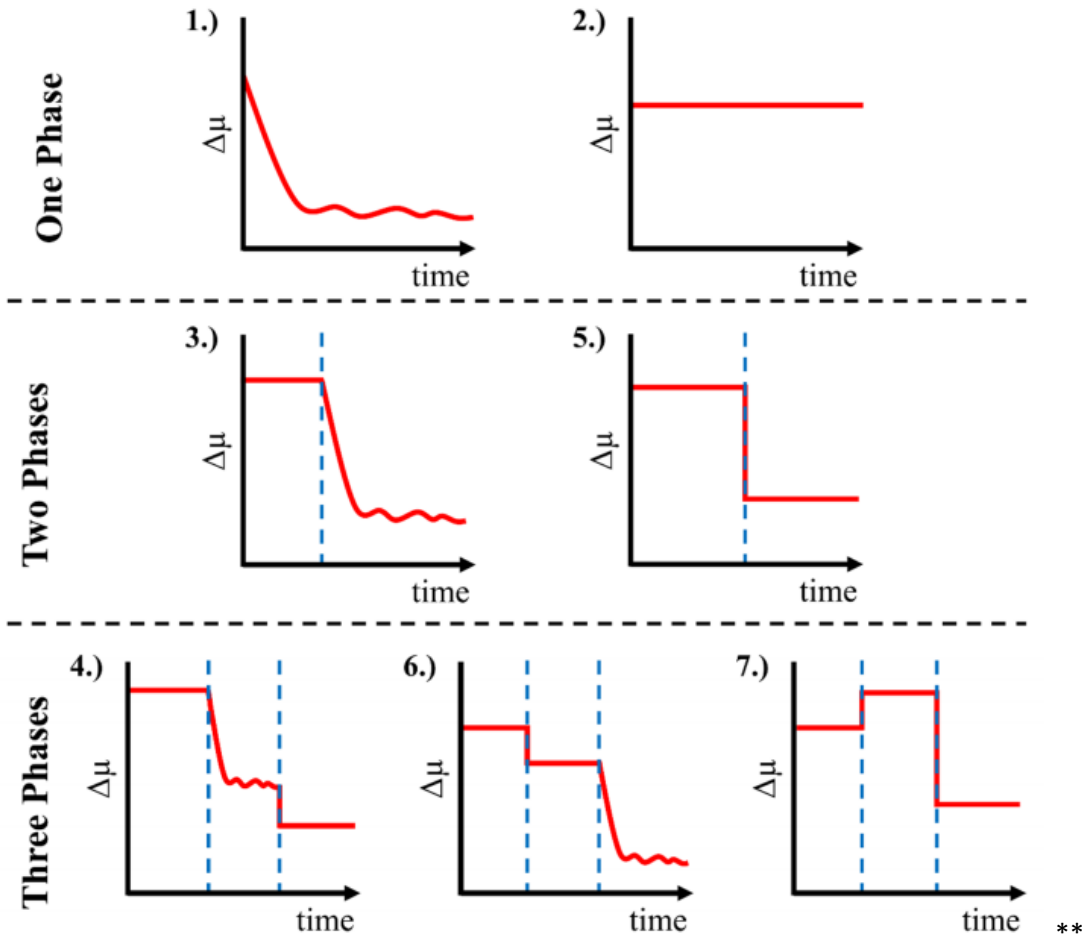

Figure 5: Types of growth modes available in CG. Red line shows the input Δμ value. Red oscillating lines show Δμ approaching equilibrium. Blue dashed lines show at what iteration the change in Δμ occurs.

2.3.1.1.2. *Molecular.txt.* CG exchanges information with the topology programme ToposPro (A. Hill, Personal Communication, May 5, 2020). Whilst ToposPro can partition a unit cell of baryte, CG takes this partitioned structure from ToposPro and simulates the statistical probability of growth vs dissolution (A. Hill, Personal Communication, May 5, 2020). To run an experiment using CG, a partitioned crystal structure is required. ToposPro generates a file described as a "structure file", this contains all the components in a unit cell and the components they connect to. The file molecular.txt defines the energy and types of connections from the structure file. Figure 4 shows the baryte model produced by ToposPro. Barium is bonded to 7 sulphate anions, 5 of which (represented by interactions 1, 2 and 3) show bidentate ligands where two oxygen atoms originating from the same sulphate ion bond to barium, and 2 of which (represented by interactions 4 and 5) show monodentate ligands where only one oxygen atom is bonded to barium. Whilst the distances between Ba^{2+} and SO_4^{2-} can be geometrically calculated, the sum of the energy of desolvation and crystallisation varies greatly depending on whether the ligand is bidentate or monodentate, whether SO_4^{2-} is connected to Ba^{2+} by one oxygen or two.

3. Methods

This work compared the morphology of baryte between simulations in CG and experimental nucleation and growth with SEM analysis. This research was carried out to test the validity of CG compared to baryte grown under specific conditions and compare, using tabletop SEM, the morphological features of these results to previous master students.

3.1. CG Simulations

Two input data files could be edited when running simulations: input.txt and molecular.txt. The latter allows the user to input $\Delta_{cry}G$ (kcal/mol) between neighbouring species. The former file, input.txt, is where parameters can be manipulated which are read by the CG application. Previous calculations show that the $\Delta_{cry}G$ was around 15 kcal/mol. This value was divided between 5 interaction types over 7 total interactions. The exact values were difficult to determine, however keeping interaction types 1, 4 and 5 lower than interaction types 2 and 3 showed similar morphologies to Stack et al., 2012. An example of molecular.txt can be seen in Figure 6. CG was programmed with the baryte unit cell crystal containing four Ba^{2+} and four SO_4^{2-} (Antao, 2012). Each $\Delta_{cry}G$ value was repeated for every individual ion.

```
1:[1A](1/2+x,1/2-y,1/2-z) R=3.466
2:[1A](-x,1/2+y,-z) R=3.539
2:[1A](-x,1/2+y,-z)(0,-1,0) R=3.539
3:[1A](1/2-x,-y,1/2+z)(0,-1,0) R=3.658
3:[1A](1/2-x,-y,1/2+z) R=3.658
4:[1A](1/2+x,1/2-y,1/2-z)(0,0,1) R=4.004
5:[1A](0,0,1) R=4.221
0.1
3.7
3.7
0.1
0.1
```

Figure 6: Example of molecular.txt showing five interaction types and $\Delta_{cry}G$ for each type.

To create a similar simulation environment to laboratory experiments, growth mode 3 was used as the baryte solution was assumed to reach approximate equilibrium within the laboratory incubation time of 180±20 minutes. To simplify non-stoichiometric simulations, the starting $\Delta\mu$ was determined by

Visual MINTEQ (Gustafsson, 2013) and excess Δμ were added when running the CG application. An example of input.txt is shown in Figure 7.

./Simulations/Robin/Baryte/	Directory to store data
1_Baryte	File root to store data
no	Do you want to load a checkpoint to start your simulation? yes/no
N/A	File path for checkpoint load
yes	Do you want to save a checkpoint at the end of your simulation? yes/no
./Structure_Files/Ionic/Baryte.txt	File path to structure file: e.g. ../LTA.txt (Must be a text file)
normal	normal/growth_modifier/ordered?
no	Screw dislocations? (yes / no)
1	How many checking sweeps, 1 is normal, 2 to clear internal defects. 1 or 2?
1	Method for determining multipliers for combinations. 1 or 2?
yes	Is this a molecular crystal? (yes / no)
yes	Do you want to calculate required memory for your calculation? yes/no
4000	What is the maximum memory in MBytes that you wish to use? Recommended default 10000 MBytes
21.0	Temperature in Celsius?
1000000	Number of iterations? (Must be an integer)?
3	Delta mu mode?
yes	Do you want an excess supersaturation of any component (always yes for a MOF)? yes/no
2.0	Starting delta mu [kcal/mol]?
1	MOVIE: The number of frames? (must be an integer)
1	MOVIE: Iteration at initial frame? (default is 1) (must be an integer)
1000000	MOVIE: Iteration at final frame? (default is number of iterations) (must be an integer)
1000000	Delta mu DATA: The number of outputs? (must be an integer)
1	Delta mu DATA: Iteration at initial output? (default is 1) (must be an integer)
1000000	Delta mu DATA: Iteration at final output? (default is number of iterations) (must be an integer)
no	Do you want to visualise crystal terraces? (yes/no)
N/A	File path for crystal terrace colouring

Figure 7: Example of input.txt with explanations of each line.

For the simulations, 1,000,000 iterations were calculated to simulate baryte. As growth mode 3 was used, an initial, constant Δμ was followed by a Δμ approaching equilibrium . To accurately represent the experimental conditions, the number of iterations set during the initial stage was 100,000 and the equilibrium stage was set to 900,000 for all simulations.

3.2. Implementing Non-Stoichiometric Conditions

Two possible ways of influencing stoichiometry were identified in CG. One of them being line seventeen in input.txt which contains the question "Do you want an excess supersaturation of any component (always yes for a MOF)? yes/no". Answering "yes" gives the possibility of changing the Δμ of Ba^{2+} and SO_4^{2-} in CG Application (Figure 8).

```
File path to read in checkpoint?
Do you want to create a checkpoint at the end of the simulation? yes/no
_____________________________________________________________________________
_____________________________________________________________________________
file_title  55:Barite
_____________________________________________________________________________
_____________________________________________________________________________
Do you want to have different weighting for multiple bonds? yes/no
no
How many periods of different supersaturation?
1
What is the excess for tiletype            1 (put -1 for solvent in a MOF)

1
What is the excess for tiletype            2 (put -1 for solvent in a MOF)
1
What is the excess for tiletype            3 (put -1 for solvent in a MOF)
1
What is the excess for tiletype            4 (put -1 for solvent in a MOF)
1
What is the excess for tiletype            5 (put -1 for solvent in a MOF)
1
What is the excess for tiletype            6 (put -1 for solvent in a MOF)
1
What is the excess for tiletype            7 (put -1 for solvent in a MOF)
1
What is the excess for tiletype            8 (put -1 for solvent in a MOF)
1
Do you want to find surfaces or colour surfaces? find/colour
```

Figure 8: Example of CG Application that shows how to edit the stoichiometry of each ion or "tiletype". Tiletypes 1 – 4 represent SO4 and tiletypes 5 – 8 represent Ba as described in the input file "Baryte". Supersaturation is measured as Δμ (kcal/mol).

Alternatively, molecular.txt could be manipulated to influence the amount of energy required for a Ba^{2+} or SO_4^{2-} ion to attach. Changing the ratio of interaction energies could also result in a change in stoichiometry. For this, both the SO_4^{2-} and Ba^{2+} components of a unit cell still had to equal ~15 kcal/mol so for every increase in the ladder for one component of a unit cell, the other would have to decrease

proportionally. This approach would change the relative energies for the interactions between neighbours as well as the stoichiometry. Figure 9 visualises these different ways of interpreting stoichiometry.

3.2.1. Changing Δμ in molecular.txt as a Function of Stoichiometry

For simplicity, only changing the relative Δμ values were simulated as few constraints were identified which suggested a different $\Delta_{cry}G$ between Ba^{2+} and SO_4^{2-}. The simulations were carried out using the activities calculated by VMINTEQ which were also used to calculate the activity of each ion. This resulted in the difference between the initial IAP and IAP at equilibrium. For calculating non-stoichiometric Δμ values, two separate values had to be calculated, Δμ 1 and Δμ 2 (Figure 9A). CG simulated non-stoichiometric solutions by assuming all components in a baryte unit cell start with the same Δμ value and then an excess is provided in the CG Application (Figure 8). The input values used are shown in Table 5.

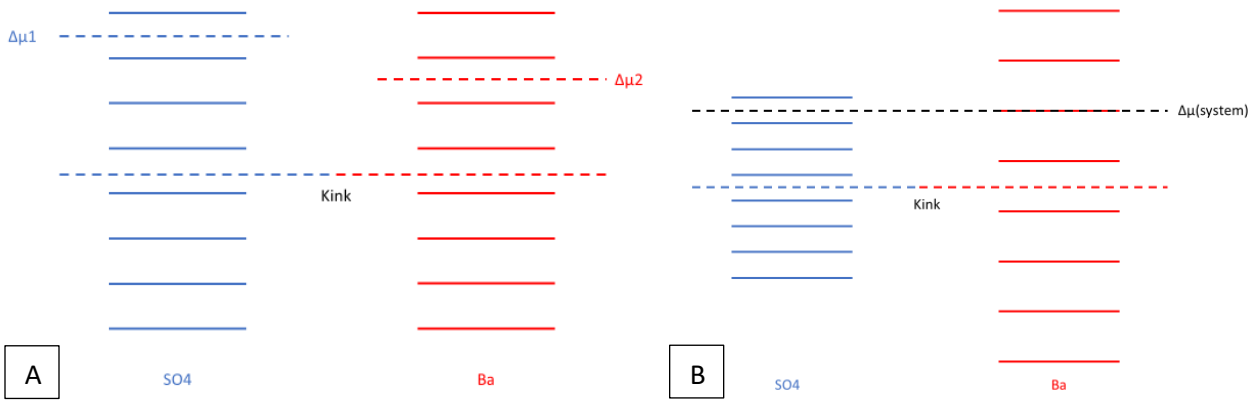

Figure 9: Visualisation of different ways of simulating stoichiometry with CG, either by changing the concentrations of each ion, A; or changing the amount of energy required to gain another ion to the bulk crystal, B.

3.3. Laboratory Techniques

3.3.1. Solution Calculations

The solution modelling software, Visual MINTEQ (VMINTEQ), was used to calculate the concentrations, activities, and ionic strengths (I) of Ba^{2+}, Cl^-, NO_3^-, K, Na^+ and SO_4^{2-} for each mixture created. Different batch experiments were carried out: one with independent ionic strength (I) or no

addition of any salt, the others with a total initial I of 0.02 M which would change little over the course of the experiment. I was calculated by VMINTEQ with the general formula:

Equation 18

$$I = \frac{1}{2}\sum c_i z_i^2$$

Where I, the ionic strength, is half the sum of c_i, which is the molar concentration of an ion, and z_i the charge of the ion squared (Lehmann et al., 1996).

Four different ways of crystallising baryte were analysed in the batch experiments. These included $BaCl_2$ + Na_2SO_4, $BaCl_2$ + Na_2SO_4 + NaCl, $BaNO_3$ + $NaSO_4$ + $NaNO_3$ and $BaCl_2$ + K_2SO_4 + KCl. These reactions were carried out at different supersaturations and five different concentration ratios (r).

3.3.2. Batch Experiments

3.3.2.1. $BaCl_2$ + Na_2SO_4 with no excess NaCl. Due to the COVID-19 pandemic, I was only able to observe the laboratory set-up with solutions of no additional salts. All solutions were made by S. Seepma.

Two stock solutions of 0.2M $BaCl_2$ (Barium Chloride Dihydrate; purity ≥99%; Sigma-Aldrich) and 0.24M Na_2SO_4 (Sodium Sulphate Decahydrate; purity ≥99%; Sigma-Aldrich) were made in 0.5L volumetric flasks (Figure 10A). These solutions were made by mixing 20.823g $BaCl_2$ and 14.204g Na_2SO_4 respectively with ultra-pure water until 0.5L was reached. To further dilute each batch an amount of each stock solution was diluted to an equivalent concentration of Δμ 2, 3, 4 or 7 with stoichiometries (r) of [Ba]:[SO_4] of 0.01, 0.1, 1, 10 and 100. 50 mL beakers were used for Δμ 4 and 7, 250 mL beakers for Δμ 3 and 1L beakers for Δμ 2 (Figure 10B). One dilution error was made for Δμ 2, r=0.01 and r=100, the batch was calculated for an initial beaker of 2L but a 1L beaker was used during dilution. This increased Ω or Δμ so was higher than initially anticipated. Further limitations included the high volume of stock solution required for Δμ 7 batches, as a 50 mL beaker was used to mix stock solutions, only when r = 1 did both

stock solution volumes fit into this beaker with a volume of 25 mL from each batch solution. All other experiments required too much stock solution. An overview of VMINTEQ calculations is shown in Table 1.

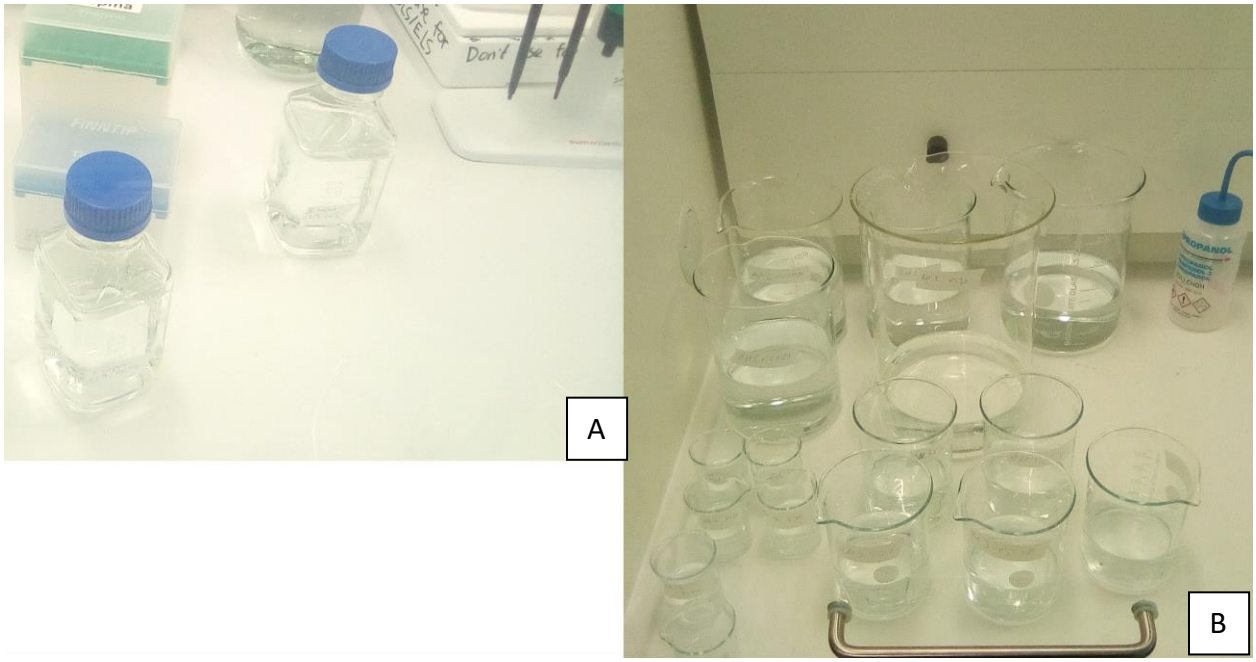

Figure 10: Stock solutions of $BaCl_2$ and Na_2SO_4, A. Sixteen batch experiments varying in Δμ and r, B.

Table 1: VMINTEQ calculations based on input including calculations based on VMINTEQ output, without added NaCl. VMINTEQ input was the basis for laboratory experiments.

VMINTEQ INPUT (mmol)					VMINTEQ OUTPUT					Calculations	
$[Ba^{2+}]:[SO_4^{2-}]$ (r)	$[Ba^{2+}]$	$[Cl^-]$	$[Na^+]$	$[SO_4^{2-}]$	$\{Ba^{2+}\}$	$\{SO_4^{2-}\}$	SI	pH	I	Ω	Δμ
0.01	0.0093	0.0186	1.86	0.93	6.85E-06	7.33E-04	1.727	7.1	2.80E-03	53.3	2
0.01	0.031	0.062	6.2	3.1	1.76E-05	2.04E-03	2.589	7.1	9.24E-03	388.2	3
0.01	0.123	0.246	24.6	12.3	4.44E-05	5.76E-03	3.433	7.1	0.0356	2710.2	4
0.1	0.026	0.052	0.52	0.26	2.22E-05	2.27E-04	1.737	7.1	8.54E-04	54.6	2
0.1	0.078	0.156	1.56	0.78	5.86E-05	6.17E-04	2.593	7.1	2.54E-03	391.7	3
0.1	0.257	0.514	5.14	2.57	1.52E-04	1.71E-03	3.449	7.1	8.25E-03	2811.9	4
1.0	0.08	0.16	0.16	0.08	7.18E-05	7.18E-05	1.747	7.1	4.77E-04	55.8	2
1.0	0.23	0.46	0.46	0.23	1.91E-04	1.91E-04	2.596	7.1	1.36E-03	394.5	3
1.0	0.7	1.4	1.4	0.7	5.06E-04	5.03E-04	3.44	7.1	4.05E-03	2754.2	4
1.0	50	100	100	50	1.08E-02	9.63E-03	6.053	7.2	0.2327	~1E+6	7
10	0.26	0.52	0.052	0.026	2.27E-04	2.22E-05	1.738	7.1	8.55E-04	54.7	2
10	0.78	1.56	0.156	0.078	6.21E-04	5.86E-05	2.595	7.1	2.55E-03	393.6	3
10	2.53	5.06	0.506	0.253	1.71E-03	1.50E-04	3.442	7.1	8.19E-03	2766.9	4
100	0.94	1.88	0.0188	0.0094	7.43E-04	6.90E-06	1.745	7.1	2.84E-03	55.6	2
100	3.09	6.18	0.0618	0.0309	2.06E-03	1.75E-05	2.592	7.1	9.32E-03	390.8	3
100	12.09	24.18	0.2418	0.1209	5.94E-03	4.31E-05	3.444	7.1	3.62E-02	2779.7	4

Neither the stock solutions nor the diluted samples were filtered prior to mixing.

3.3.2.2. Batch Experiments with Excess Salts. I was not able to observe the laboratory set-ups of the batches with a controlled amount of excess salt or Δμ = 5. In total, three different reactions were tested when crystallising baryte: $BaCl_2 + Na_2SO_4 + NaCl$, $BaNO_3 + Na_2SO_4 + NaNO_3$, and $BaCl_2 + K_2SO_4 + KCl$. Similarly, these experiments were carried out at ~21°C with multiple stock solutions to dilute each solution efficiently, rather than diluting two stock solutions for longer. Δμ of 2, 3, 4 and 5 were calculated from VMINTEQ at r of 0.01, 0.1, 1, 10 and 100. Two mixtures from each reaction had more extreme r values of 0.001 and 1000 and were made at a concentration of Δμ = 4. No additional salts were added as I > 0.02M for these mixtures. Δμ 2 r = 0.01 and 100 were diluted in a 2L solution whilst r = 0.1, 1 and 10 were diluted in 1L. All Δμ 3 mixtures in this batch were diluted in a 500 mL solution. Δμ 4, r = 0.001 and 1000 were also diluted in a 500 mL solution whilst r = 0.01, 0.1, 1, 10 and 100 were diluted in a 100 mL solution. All Δμ 5 experiments were diluted in 30 mL solutions. Table 2 - Table 4 show the conditions at which baryte was nucleated and crystallised.

Table 2: VMINTEQ calculations based on input including calculations based on VMINTEQ output, with added NaCl. VMINTEQ input was the basis for laboratory experiments.

VMINTEQ INPUT (mmol)					VMINTEQ OUTPUT					Calculations	
$[Ba^{2+}]:[SO_4^{2-}]$ (r)	$[Ba^{2+}]$	$[Cl^-]$	$[Na^+]$	$[SO_4^{2-}]$	$\{Ba^{2+}\}$	$\{SO_4^{2-}\}$	SI	pH	I	Ω	Δμ
0.001	3.26E-5	6.52E-5	6.52E-2	3.26E-2	8.0E-6	1.11E-2	3.0	7.2	0.09	1000	4
0.01	5.98E-5	3.12E-3	1.5E-2	5.98E-3	2.74E-5	3.27E-3	3.0	7.1	0.02	1002	4
0.1	1.76E-4	1.5E-2	1.82E-2	1.76E-3	9.38E-5	9.53E-4	3.0	7.1	0.02	1000	4
1.0	5.48E-4	1.82E-2	1.82E-2	5.48E-4	3.06E-4	2.92E-4	3.0	7.1	0.02	1000	4
10	1.76E-3	1.83E-2	1.52E-2	1.76E-4	9.95E-4	8.99E-5	3.0	7.1	0.02	1000	4
100	5.9E-3	1.46E-2	2.92E-3	5.9E-5	3.35E-3	2.67E-5	3.0	7.1	0.02	1002	4
1000	3.16E-2	6.32E-2	6.32E-5	3.16E-5	1.18E-2	7.56E-6	3.0	7.1	0.09	1000	4
0.01	2.52E-5	1.3E-2	1.8E-2	2.52E-3	1.3E-5	1.37E-3	2.3	7.1	0.02	200	3
0.1	7.74E-5	1.82E-2	1.96E-2	7.74E-4	4.27E-5	4.18E-4	2.3	7.1	0.02	200	3
1.0	2.42E-4	1.92E-2	1.92E-2	2.42E-4	1.37E-4	1.3E-4	2.3	7.1	0.02	200	3
10	7.7E-4	1.91E-2	1.78E-2	7.7E-5	4.39E-4	4.8E-5	2.3	7.1	0.02	200	3
100	2.5E-3	1.77E-2	1.28E-2	2.5E-5	1.43E-3	1.25E-5	2.3	7.1	0.02	200	3
0.01	9.6E-6	1.73E-2	1.92E-2	9.6E-4	5.28E-6	5.22E-4	1.49	7.1	0.02	31	2
0.1	3.01E-5	1.94E-2	1.99E-2	3.01E-4	1.7E-5	1.63E-4	1.49	7.1	0.02	31	2
1.0	9.5E-5	2.0E-2	2.0E-2	9.5E-5	5.4E-5	5.13E-5	1.49	7.1	0.02	31	2
10	3.0E-4	1.98E-2	1.92E-2	3.01E-5	1.72E-4	1.62E-5	1.49	7.1	0.02	31	2
100	9.6E-4	1.92E-2	1.73E-2	9.6E-6	5.48E-4	5.05E-6	1.49	7.1	0.02	31	2
0.01	2.18E-4	4.36E-4	4.36E-2	2.18E-2	6.31E-5	8.52E-3	3.78	7.2	0.06	6000	5

0.1	4.54E-4	4.54E-3	1.51E-2	4.54E-3	2.19E-4	2.46E-3	3.78	7.1	0.02	6000	5
1.0	1.38E-3	1.53E-2	1.53E-2	1.38E-3	7.46E-4	7.18E-4	3.78	7.1	0.02	6000	5
10	4.49E-3	1.47E-2	6.7E-3	4.49E-4	2.53E-3	2.13E-4	3.78	7.1	0.02	6000	5
100	2.12E-2	4.24E-2	4.24E-4	2.12E-4	8.9E-3	6.02E-5	3.78	7.1	0.06	6000	5

Table 3: VMINTEQ calculations based on input including calculations based on VMINTEQ output, with added $NaNO_3$. VMINTEQ input was the basis for laboratory experiments.

VMINTEQ INPUT (mmol)					VMINTEQ OUTPUT					Calculations	
$[Ba^{2+}]:[SO_4^{2-}]$ (r)	$[Ba^{2+}]$	$[NO_3^-]$	$[Na^+]$	$[SO_4^{2-}]$	$\{Ba^{2+}\}$	$\{SO_4^{2-}\}$	SI	pH	I	Ω	Δμ
0.001	3.26E-5	6.52E-5	6.52E-2	3.26E-2	8.03E-06	1.11E-02	3.0	7.2	0.09	1000	4
0.01	6.0E-5	3.12E-3	1.5E-2	6.0E-3	2.72E-05	3.28E-03	3.0	7.1	0.02	1002	4
0.1	1.79E-4	1.485E-2	1.8E-2	1.79E-3	9.20E-05	9.70E-04	3.0	7.1	0.02	1000	4
1.0	5.6E-4	1.8E-2	1.8E-2	5.6E-4	2.99E-04	2.99E-04	3.0	7.1	0.02	1000	4
10	1.79E-3	1.798E-2	1.48E-2	1.79E-4	9.71E-04	9.21E-05	3.0	7.1	0.02	1000	4
100	6.0E-3	1.5E-2	3.12E-3	6.0E-5	3.28E-03	2.72E-05	3.0	7.1	0.02	1002	4
1000	3.26E-2	6.52E-2	6.52E-5	3.26E-5	1.11E-02	8.03E-06	3.0	7.1	0.09	1000	4
0.01	2.57E-5	1.305E-2	1.81E-2	2.57E-0	1.28E-05	1.40E-03	2.3	7.0	0.02	200	3
0.1	7.92E-5	1.806E-2	1.95E-2	7.92E-4	4.18E-05	4.28E-04	2.3	7.0	0.02	200	3
1.0	2.48E-4	1.92E-2	1.92E-2	2.48E-4	1.34E-04	1.34E-04	2.3	7.1	0.02	200	3
10	7.92E-4	1.948E-2	1.81E-2	7.92E-5	4.28E-04	4.18E-05	2.3	7.1	0.02	200	3
100	2.57E-3	1.814E-2	1.31E-2	2.57E-5	1.39E-03	1.28E-05	2.3	7.1	0.02	200	3
0.01	9.85E-6	1.732E-2	1.93E-2	9.85E-4	5.18E-06	5.35E-04	1.49	7.0	0.02	31	2
0.1	3.08E-5	1.926E-2	1.98E-2	3.08E-4	1.65E-05	1.67E-04	1.49	7.0	0.02	31	2
1.0	9.75E-5	1.988E-2	1.99E-2	9.75E-5	5.26E-05	5.27E-05	1.49	7.1	0.02	31	2
10	3.08E-4	1.972E-2	1.92E-2	3.08E-5	1.67E-04	1.66E-05	1.49	7.1	0.02	31	2
100	9.85E-4	1.927E-2	1.73E-2	9.85E-6	5.35E-04	5.18E-06	1.49	7.1	0.02	31	2
0.01	2.18E-4	4.360E-4	4.36E-2	2.18E-2	6.30E-05	8.52E-03	3.78	7.3	0.06	6000	5
0.1	4.57E-4	6.814E-3	1.5E-2	4.57E-3	2.17E-04	2.47E-03	3.78	7.1	0.02	6000	5
1.0	1.41E-3	1.52E-2	1.52E-2	1.41E-3	7.32E-04	7.32E-04	3.78	7.1	0.02	6000	5
10	4.57E-3	1.504E-2	6.81E-3	4.57E-4	2.47E-03	2.17E-04	3.78	7.1	0.02	6000	5
100	2.18E-2	4.35E-2	4.35E-4	2.18E-4	8.50E-3	6.30E-5	3.78	7.1	0.06	6000	5

Table 4: VMINTEQ calculations based on input including calculations based on VMINTEQ output, with added KCl. VMINTEQ input was the basis for laboratory experiments.

VMINTEQ INPUT (mmol)				VMINTEQ OUPUT						Calculations	
$[Ba^{2+}]:[SO_4^{2-}]$ (r)	$[Ba^{2+}]$	$[Cl^-]$	$[K^+]$	$[SO_4^{2-}]$	$\{Ba^{2+}\}$	$\{SO_4^{2-}\}$	SI	pH	I	Ω	Δμ
0.001	3.28E-5	6.56E-5	6.56E-2	3.28E-2	8.12E-6	1.1E-2	3.0	7.2	0.09	1000	4
0.01	6.0E-5	3.12E-3	1.5E-2	6.0E-3	2.75E-5	3.26E-3	3.0	7.1	0.02	1000	4
0.1	1.77E-4	1.51E-2	1.82E-2	1.77E-3	9.43E-5	9.49E-4	3.0	7.1	0.02	1000	4
1.0	5.5E-4	1.81E-2	1.81E-2	5.5E-4	3.07E-4	2.91E-4	3.0	7.1	0.02	1000	4
10	1.77E-3	1.82E-2	1.51E-2	1.77E-4	9.99E-4	8.96E-5	3.0	7.1	0.02	1000	4
100	5.88E-3	1.43E-2	2.62E-3	5.88E-5	3.35E-3	2.67E-5	3.0	7.1	0.02	1000	4
1000	3.16E-2	6.32E-2	6.32E-5	3.16E-5	1.18E-2	7.56E-6	3.0	7.1	0.09	1000	4

0.01	2.53E-5	1.3E-2	1.8E-2	2.53E-3	1.31E-5	1.37E-3	2.3	7.1	0.02	200	3
0.1	7.75E-5	1.79E-2	1.93E-2	7.75E-4	4.29E-5	4.16E-4	2.3	7.1	0.02	200	3
1.0	2.44E-4	1.94E-2	1.94E-2	2.44E-4	1.38E-4	1.30E-4	2.3	7.1	0.02	200	3
10	7.75E-4	1.93E-2	1.79E-2	7.75E-5	4.41E-4	4.06E-5	2.3	7.1	0.02	200	3
100	2.51E-3	1.76E-2	1.27E-2	2.51E-5	1.43E-3	1.25E-5	2.3	7.1	0.02	200	3
0.01	9.7E-6	1.76E-2	1.95E-2	9.7E-4	5.32E-6	5.2E-4	1.49	7.1	0.02	31	2
0.1	3.03E-5	1.94E-2	1.99E-2	3.03E-4	1.71E-5	1.62E-4	1.49	7.1	0.02	31	2
1.0	9.54E-5	1.99E-2	1.99E-2	9.54E-5	5.42E-5	5.10E-5	1.49	7.1	0.02	31	2
10	3.03E-4	1.99E-2	1.94E-2	3.03E-5	1.73E-4	1.61E-5	1.49	7.1	0.02	31	2
100	9.65E-4	1.92E-2	1.73E-2	9.65E-6	5.51E-4	5.03E-6	1.49	7.1	0.02	31	2
0.01	2.19E-4	2.19E-2	4.38E-2	2.19E-2	6.36E-5	8.43E-3	3.78	7.2	0.06	6000	5
0.1	4.55E-4	4.55E-3	1.5E-2	4.55E-3	2.2E-4	2.44E-3	3.78	7.1	0.02	6000	5
1.0	1.39E-3	1.39E-3	1.52E-2	1.39E-3	7.50E-4	7.16E-4	3.78	7.1	0.02	6000	5
10	4.49E-3	4.49E-4	6.5E-3	4.49E-4	2.53E-3	2.12E-4	3.78	7.1	0.02	6000	5
100	2.12E-2	2.12E-4	4.24E-4	2.12E-4	8.9E-3	6.02E-5	3.77	7.1	0.06	6000	5

3.3.2.3. Filtering. After 180±20 minutes of letting each batch experiment reach equilibrium, the solutions were filtered using a vacuum filter (Figure 11). During the filtrations I observed, two different filters of Ø 0.2 nm were used during the filtration process: Δμ 2, r = 0.01, 0.1, 1, 10, 100 and Δμ 3, r = 0.01, r = 0.1 were all filtered with a cellulose acetate filter whilst all other solutions were filtered with a

polycarbonate filter. These filters were kept in a sealed container overnight to dry and heated to 40°C for thirty minutes to fully dry before a sample was taken for imaging.

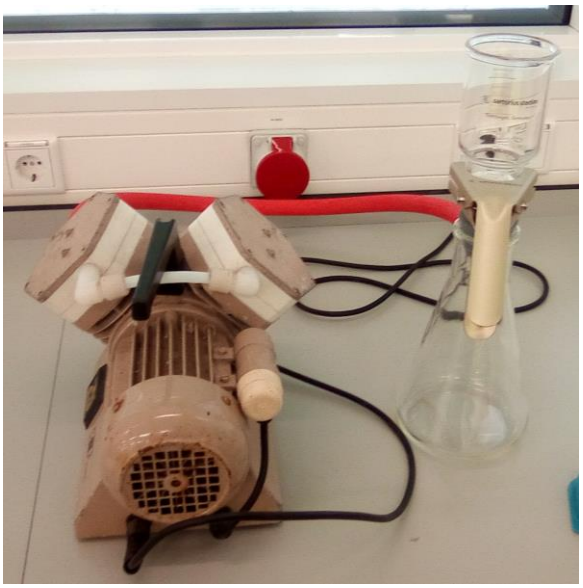

Figure 11: Vacuum pump (left) attached to sealed flask for wastewater (right). Above this container is a filter which is clamped in place along with a beaker allowing the $BaSO_4$ solution to filter through.

3.3.3. SEM Imaging

Limited time in the laboratory resulted in the observation of sixteen filters under tabletop SEM. S. Seepma collected images from tabletop SEM for baryte grown in I ≥ 0.02M conditions. A double-sided conductive carbon sticker was placed on a Ø12.7 diameter top, standard aluminium stub, a piece of filter was then cut to fit on the stub. Once all stubs had a carbon disk with a piece of filter, they were put into a sputter coater (Figure 12A). This produced a conductive layer on the sample to avoid electrostatic charging of the sample due to the electron beam, which enhances the SEM imaging procedure. The conductive coating of 80:20 Pt/Pd alloy was approximately 8 nm in thickness. After sputtering, the stubs were stored in a fume hood to reduce contamination of the samples (Figure 12B). The stubs were analysed in a JEOL JCM-6000 Tabletop SEM. In total sixteen stubs were sputtered and analysed with an electron beam voltage of 15 keV at room temperature or ~21°C.

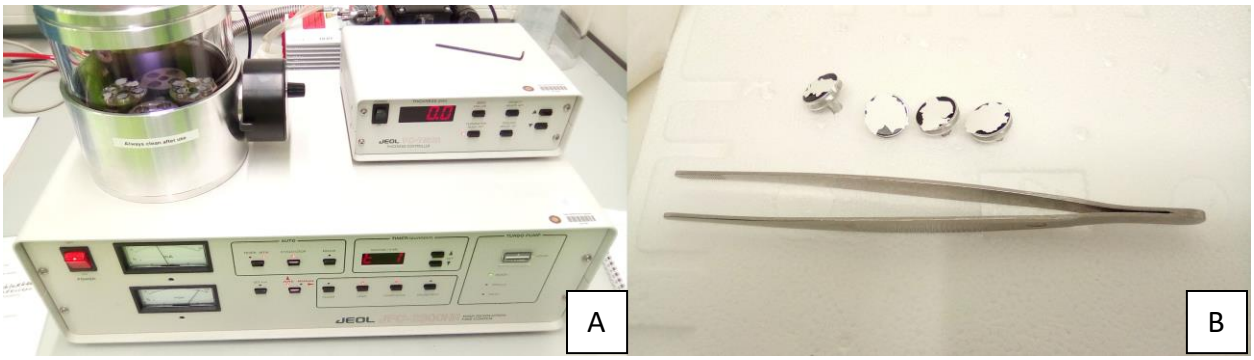

Figure 12: The sputter which ionises the surface of samples. The samples spin in the argon-filled vacuum chamber (top left) the thickness of the ionised layer is shown in nm (top right). Examples of stubs with carbon disk and filter, B.

4. Results

4.1. Selecting Δμ and Iterations for CG

Throughout all simulations, the number of iterations was 1,000,000, growth mode 3 was used, the initial number of iterations was 100,000 and the number of iterations approaching equilibrium was 900,000. This iteration sequence and the growth mode were decided, based on the laboratory setup where solutions were incubated to equilibrium. To overcome the immediately high energy of nucleation, the Δμ had to be maintained for several iterations to stabilise the crystal nucleus, allowing for further crystallisation. A crystal nucleus could be identified at 1000 iterations but did not show any easily definable surfaces (Figure 13A), therefore the number of iterations was increased to allow for the beginning of plane formation (Figure 13B).

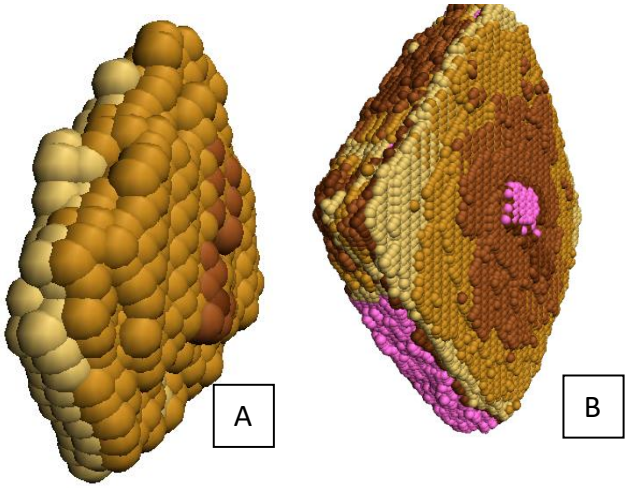

Figure 13: A - Example of a simulated baryte nucleus at Δμ = 3, r = 1, with a screw dislocation visible in the (001) plane, for 1000 iterations. B – Same conditions but for 100,000 iterations. Images are not in the same scale.

Selecting the Δμ values were also a challenge. Due to time restraints in the laboratory, only a small variety of batches could be crystallised. The low K_{SP} of baryte meant that Δμ values did not need to be incredibly high as this would prevent adequate crystal growth (Table for Δμ 7). Although simulations where Δμ = 2 were run, previous simulations where Δμ = 2 showed no baryte crystallisation (Figure 14A). Only when a screw dislocation was included; did simulations result in crystallisation (Figure 14B).

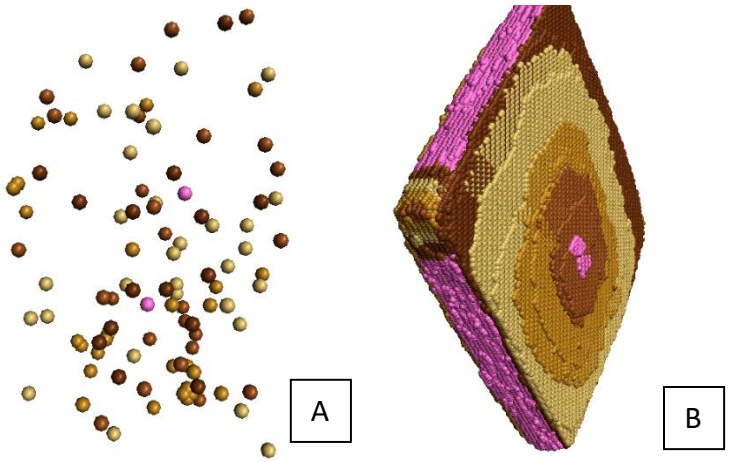

Figure 14: A – Example of simulation with Δμ = 2, growth mode 3, for 1,000,000 iterations with no screw dislocation. B – Example of simulation in the same conditions as A but with a single screw dislocation visible on the (001) plane.

4.2. Constraining molecular.txt

The blue diagram in Figure 3 shows a sketch of the amount of energy required to remove a water molecule from a central barium cation and replace it with a sulphate anion and vice versa. As more water molecules are removed, the amount of energy required to successfully achieve this reaction increases. These energies can be changed in CG in the file molecular.txt (Figure 6), the total of which has been previously calculated to ~15 kcal/mol. Whilst there is an approximate constraint of the total energy, the way this value is spread out between barium – sulphate interactions is unknown. Simulations show that changing the ratio of interaction energies can change the morphology observed significantly. If all energies were considered the same, then the result would be that each interaction energy be approximately 2.14 kcal/mol. This creates a compact structure (Figure 15), identifying the planes (001), (010), (100), (101), (110) and (210) and (211)**.** Due to CG running on a laptop for these simulations, only crystals on the nanometre scale were simulated. CG did calculate the distance between respective parallel planes. To calculate these distances on a micron-scale a supercomputer should be used to increase the number of iterations per simulation.

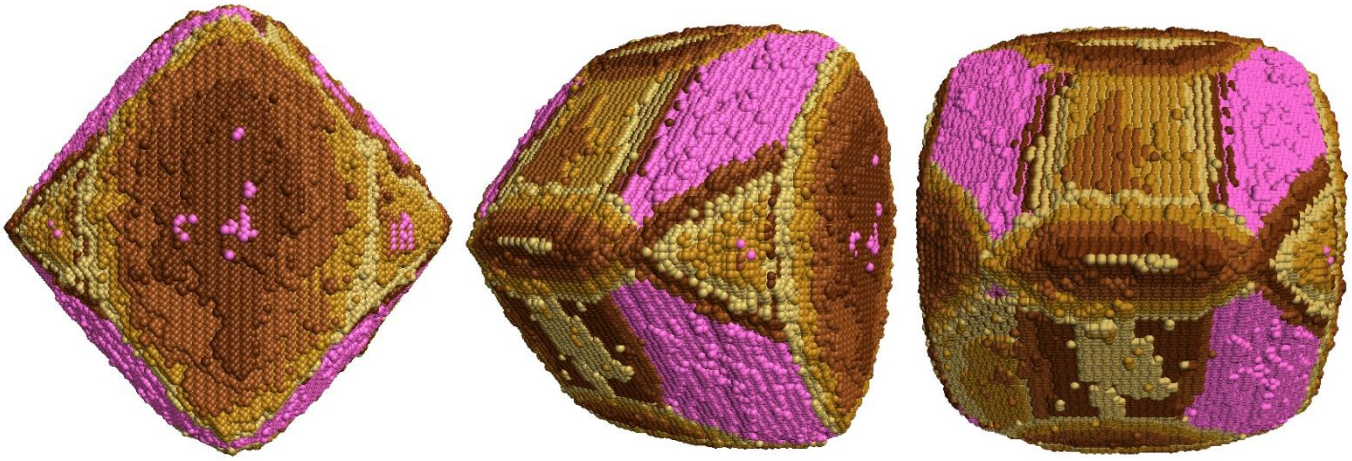

Figure 15: Example of simulated $BaSO_4$ in CG. Faces are identified by shades of brown; pink represents an undetermined face. A screw dislocation of 1 translation is included to show the effect on morphology and is observed in multiple AFM studies e.g. Bosbach et al., 1998, Pina et al., 1998, Risthaus et al., 2001.

As this compact structure does not accurately represent any morphology observed under SEM imagery, it must be understood how this structure originated and how to more accurately simulate a structure more closely representative of the SEM images or the AFM images of baryte, taken by Pina et al., 1998. This requires an understanding of the growth directions and more importantly, the organisation of interactions regarding growth.

The interaction types described in molecular.txt have a preferred orientation, therefore preference in growth direction is due to varying energies of these interaction types. An example of how these

interaction types grow is shown in Figure 16 where interaction type 1 grows in the c direction, types 2 and 3 grow in the b direction, type 4 grows in the c direction and type 5 grows in the a and c directions.

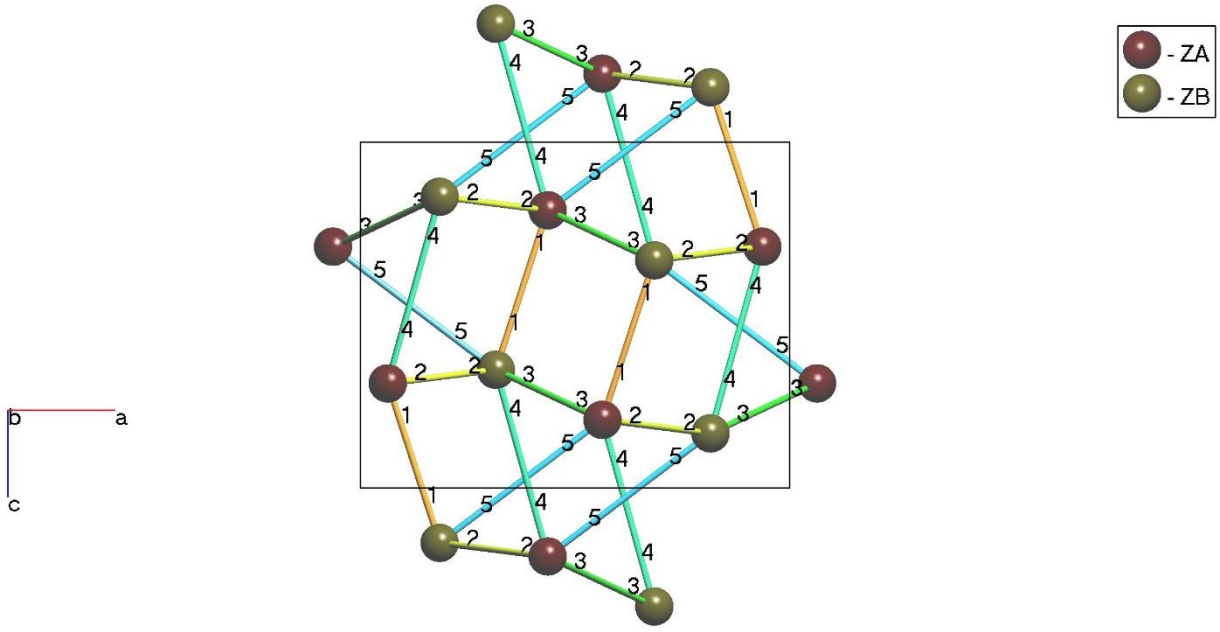

Figure 16: ToposPro model of Ba & SO4 interaction types. This model shows five different interaction types even though seven occur, this is because interaction types 2 and 3 are symmetrical, so repeated.

This distinction in growth directions helps as this further constrains the energy values in molecular.txt.

Another way of determining approximate energies includes the distinction between monodentate and bidentate interactions that sulphates with two Ba-O bonds are stronger than sulphates with one Ba-O bond (Figure 4). By this definition, interaction types 4 and 5 are weaker than interaction types 1, 2 and 3. Due to hindered growth observed in the a direction, limiting the thickness of the baryte crystals, it was determined that interaction types 2 and 3 were higher energy than type 1 which had a higher energy than types 4 and 5. For the sake of simplicity, interaction type 4 = 5 and interaction type 2 = 3 where type 4 (= 5) < 1 < 2 (= 3). Through trial and error, it was determined that to refine the thickness of the simulations, interaction types 4 and 5 could not be higher than 0.5 kcal/mol. To refine the length and breadth of the simulations, interaction types 2 and 3 could not be lower than 3.0 kcal/mol. Interaction type 1 was more difficult to constrain as the only rules in place so far were < 3 kcal/mol and > 0.5 kcal/mol. Due to the

relatively similar results of simulations constraining interaction type 1, the median value of 1.75 kcal/mol was decided.

4.3. CG Simulation Δμ Determination

In total 23 simulations were run at different Δμ and r values. Table 5 shows the Δμ values of both the starting and excess components, replicating different stoichiometric conditions.

Table 5: Δμ values determined for each simulation with activities taken from VMINTEQ calculations. Activities at Δμ = 5 were taken from the $BaCl_2$ + Na_2SO_4 + NaCl solution.

	Δμ (Ω)									
Ratio $[Ba^{2+}]$:$[SO_4^{2-}]$	2 (55)		3 (390)		4 (2800)		5 (5200)		7 (1000000)	
	Starting Δμ	Excess Δμ	Starting Δμ	Excess Δμ	Starting Δμ	Excess Δμ	Starting Δμ	Excess Δμ	Starting Δμ	Excess Δμ
0.001	N/A	N/A	N/A	N/A	3.730	4.036	N/A	N/A	N/A	N/A
0.01	2.20	2.69	3.30	2.69	4.38	2.690	4.79	2.69	N/A	N/A
0.1	2.17	1.345	3.30	1.345	3.850	1.345	4.84	1.345	N/A	N/A
1.0	2.0	0.0	3.0	0.0	4.0	0.0	5.0	0.0	7.0	0.0
10.0	2.17	1.345	3.30	1.345	3.800	1.345	4.81	1.345	N/A	N/A
100.0	2.20	2.69	3.29	2.69	3.780	2.69	4.73	2.69	N/A	N/A
1000.0	N/A	N/A	N/A	N/A	3.660	4.036	N/A	N/A	N/A	N/A

4.3.1. Description of Simulations

Due to limitations in constraining the energies of the interactions between barium and sulphate in a unit cell, defined in molecular.txt, one set of values was used throughout all simulations. This resulted in a previously described structure (Figure 14B) and a similar morphology throughout all simulations. However, specific planes were defined for example, all simulations contained a (001) (Figure 18) and (100) plane (Figure 19). (210) (Figure 20), (2-10) and (101) (not shown) planes were also identified in certain simulations. Examples of each plane are shown in Figure 17.

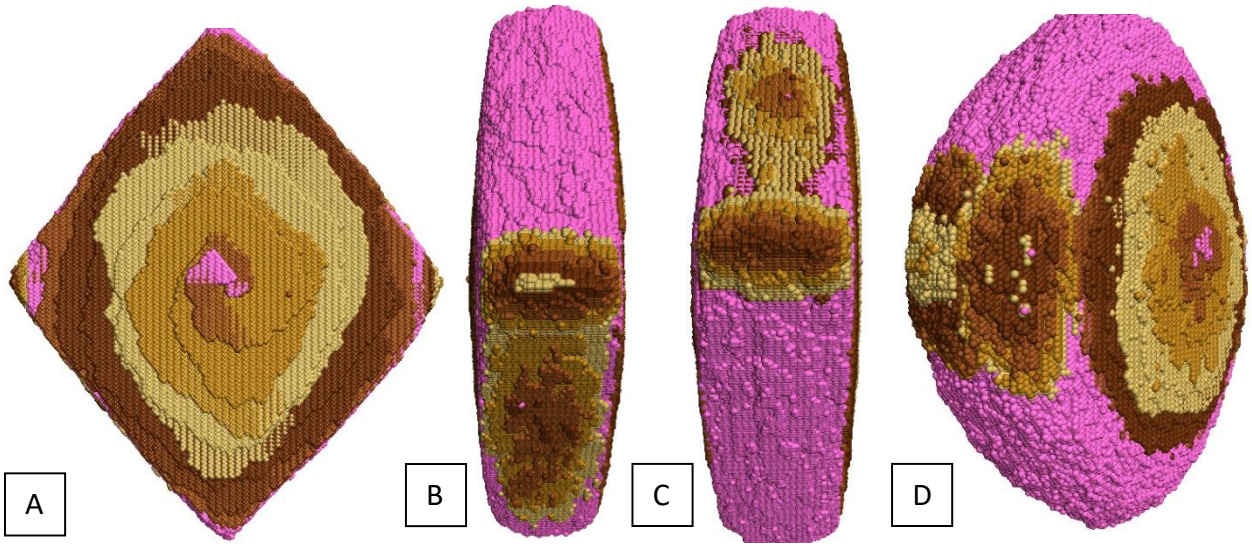

Figure 17: Example of planes identified: A – (001) plane of Δμ = 4, r = 0.1 showing a screw dislocation through the centre of the (001) plane. B – (100) and (210) of Δμ = 4, r = 0.1 showing the (100) plane as the coloured, horizontal area half way on the crystal and the (210) plane as the coloured, vertical area on the underside of the crystal. C – (100) and (2-10) of Δμ = 4, r = 10 showing the (2-10) plane as the coloured, vertical area on the upper side of the crystal. D – (001), (100) and (101) planes of Δμ = 4, r = 1000. The (101) plane was identified between the (001) and (100) plane on the front and side of the crystal.

4.3.1.1. Sizes of the (001) Plane. The (001) plane was observed in all CG simulations with the previously determined energy values in molecular.txt. Whilst all non-stoichiometric simulations resulted in slight growth on the scale of a few nm from Δμ = 2 to Δμ = 5, remaining between 15 – 25 nm, the simulation at r = 1 resulted in significant growth between Δμ = 2 and Δμ = 3, from ~15 nm to almost 60 nm, before becoming a more constant size (Figure 18). The extreme stoichiometries of 0.001 and 1000 did not significantly influence the size of (001) plane.

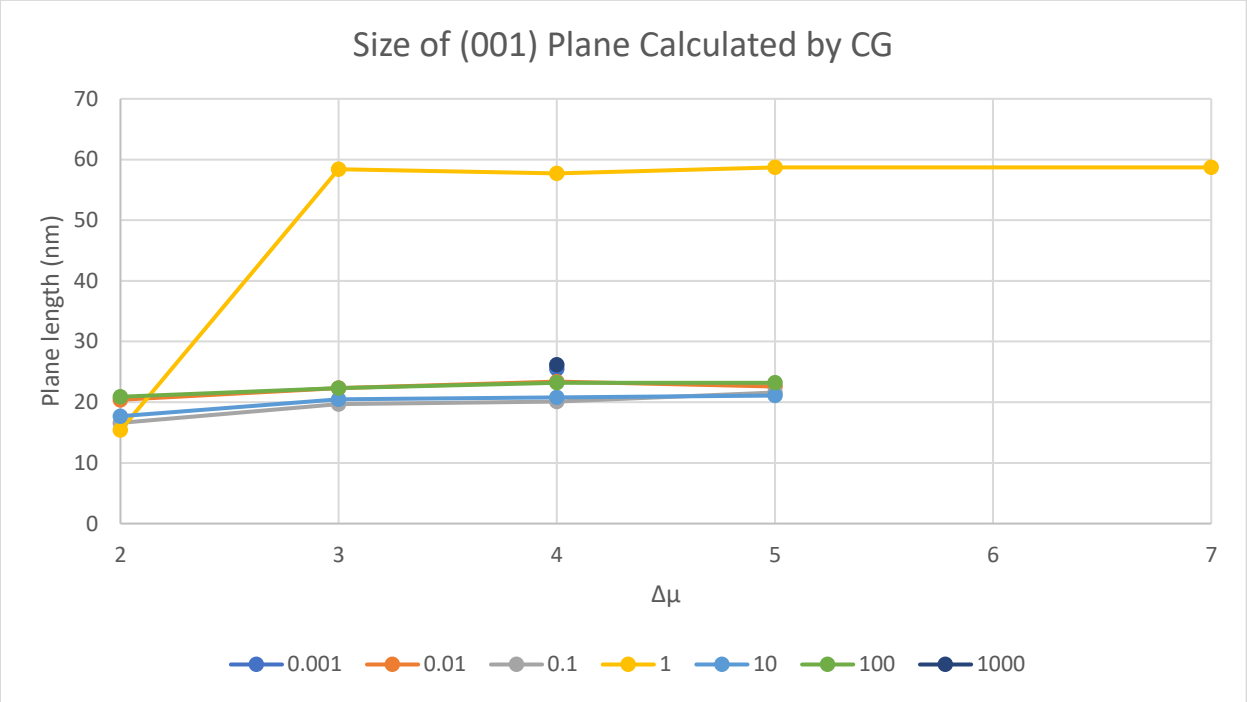

Figure 18: Lengths of the (001) plane identified in all CG simulations.

4.3.1.2. Sizes of the (100) Plane. All CG simulations also identified a (100) plane. Again, growth was primarily observed when r = 1 between Δμ = 2 and Δμ = 3, with extreme stoichiometries not greatly influencing the size of the (100) plane. The (100) plane remained a similar size throughout all Δμ values in non-stoichiometric simulations at around 60 nm but when r = 1, growth increased from ~15 nm to almost 60 nm, similar to the (001) plane (Figure 19).

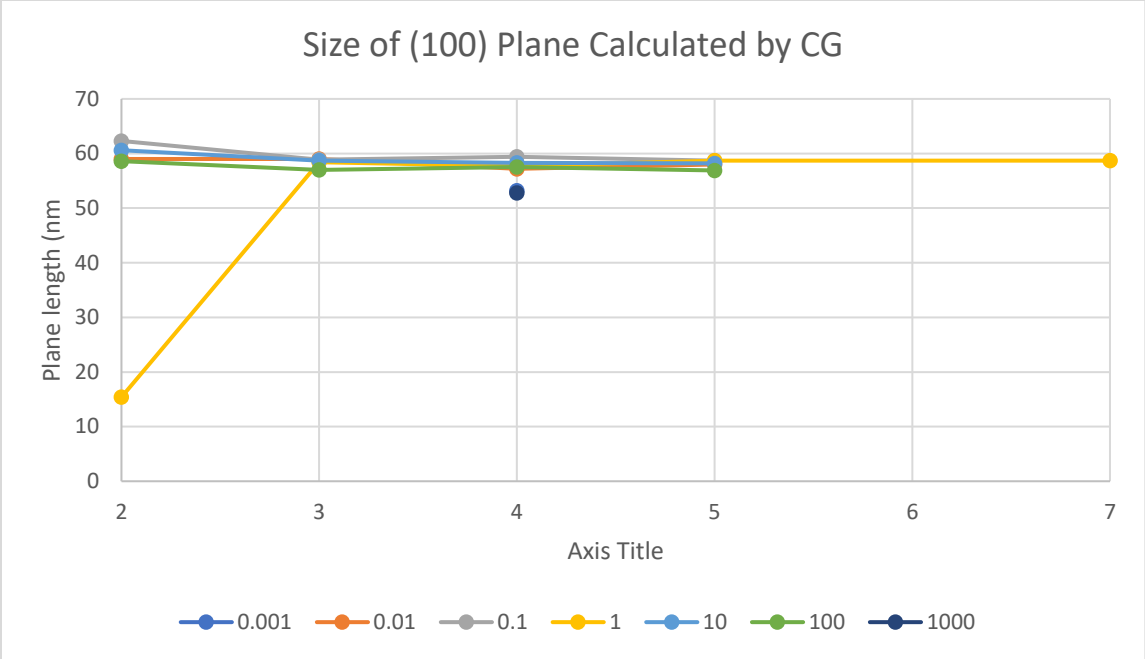

Figure 19: Lengths of the (100) plane identified in all CG simulations.

4.3.1.3. Sizes of the (210) Plane. The (210) plane was not observed in most simulations and only occurred between $\Delta\mu = 3$ and $\Delta\mu = 5$ and only between r = 0.1 and r = 10. This rather elusive plane also did not vary greatly in size varying between 46 and 49 nm in length (Figure 20).

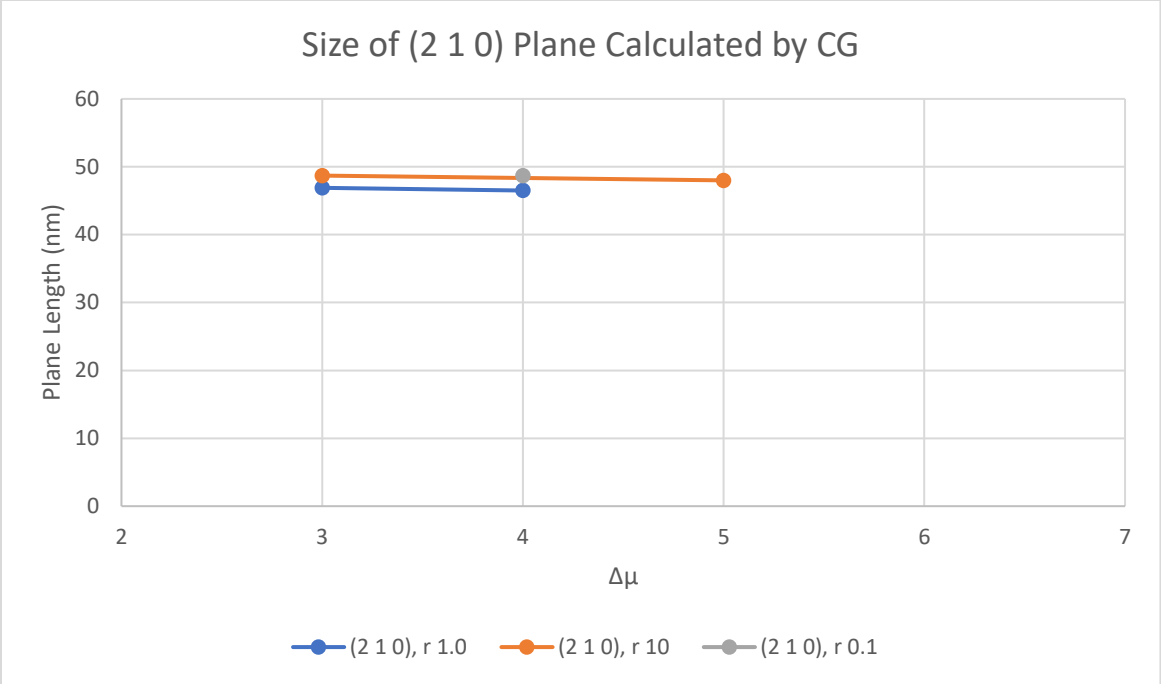

Figure 20: Lengths of the (210) plane identified in all CG simulations.

4.3.1.4. Other Planes Occasionally Identified. Other planes also observed included the (101) and (2-10) planes. The (101) planes were only observed at Δμ = 4, r = 0.001 and r = 1000 with a size of 40.0 and 40.1 nm, respectively. The (2-10) planes were identified at Δμ = 4, Δμ = 5 and Δμ = 7 at r = 10, r = 1 and r = 1, respectively. The sizes of which varied between 47 – 49 nm.

4.4. SEM Images

This results section shows the SEM Images for each batch with different reagents, concentrations, and ionic strengths. Firstly, this section will show experiments without additional salt. These experiments were supervised by S. Seepma. The following sections include experiments with additional salt. These experiments were carried out by S. Seepma.

4.4.1. Crystallising Baryte without additional Background Electrolyte (BE)

4.4.1.1. Crystal Sizes. Figure 21 shows the changes in crystal sizes as a function of Δμ, showing that when r > 1, size increases slightly with Δμ between Δμ = 2 and Δμ = 4, both increasing by around 5 μm^2. Big size increases occurred for r = 0.1 and r = 1 between Δμ = 2 and Δμ = 4 with r = 0.1 doubling in size by Δμ = 3 and tripling from Δμ = 3 to Δμ = 4, reaching 60 μm^2. The size increase of r = 1 is less dramatic increasing linearly from Δμ = 2 to Δμ = 4. The outliers in this batch were the r = 0.01 experiments which varied in crystal size as Δμ increased. Due to all crystals being difficult to measure in thickness, only width and length were measured to create a surface area calculation.

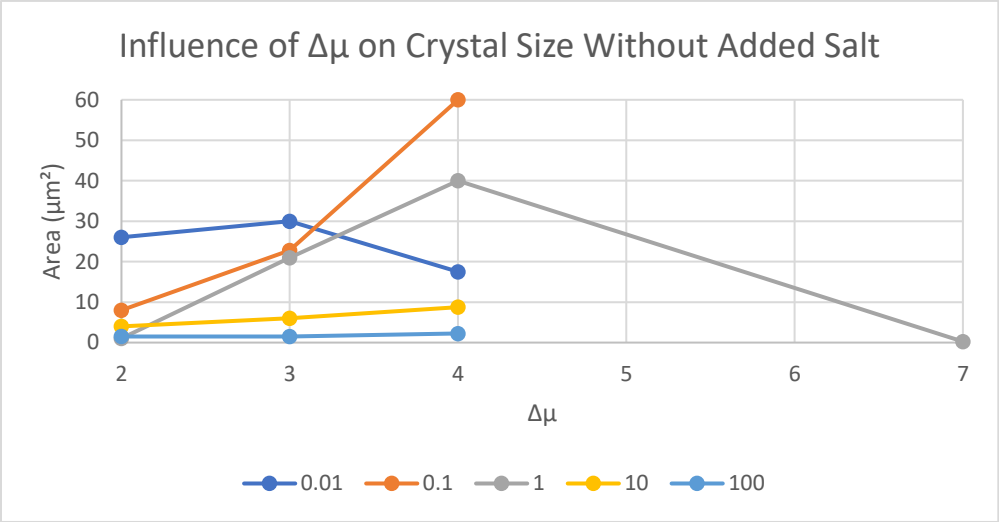

Figure 21: Change in crystal size as a function of Δμ for each stoichiometric system in the solutions without additional salt. Note that no accurate line can be drawn between Δμ 4 and Δμ 7 as experiments at Δμ 5 and 6 were not carried out in these conditions.

4.4.1.2. Crystal Morphologies. Figure 22 shows the crystals at r = 0.01 exhibited a tabular morphology with an increase in both rounded edges and twinning as Δμ increases. Twinning was never dominant in any r = 0.01 experiment and the occurrence of rounding was more obvious between Δμ = 3 and Δμ = 4 than between Δμ = 2 and Δμ = 3. The SEM results at Δμ = 3 are not extremely clear due to

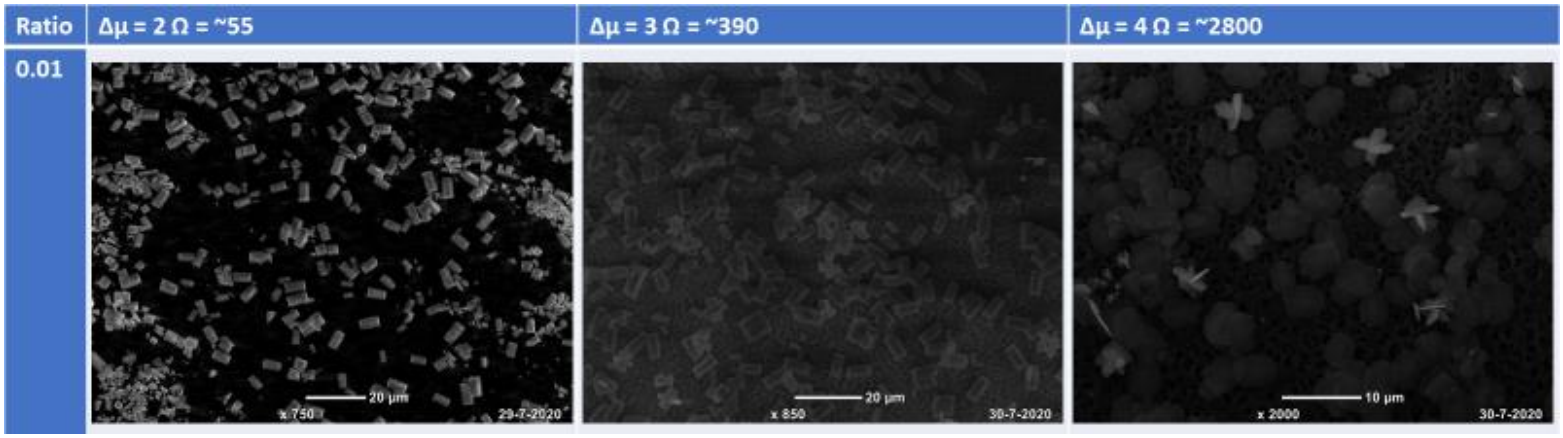

Figure 22: Tabletop SEM results of no additional BE baryte mixtures with a [Ba^{2+}]:[SO_4^{2-}] ratio of 0.01.

problems with the sputter coating.

Figure 23 shows that the experiments at r = 0.1 exhibit a similar pattern to crystals grown at r = 0.01, with tabular crystals becoming more twinned and rounded as Δμ increases. Twinning was more abundant at Δμ = 3 and Δμ = 4 compared to the r = 0.01 batches. At Δμ = 4, perpendicular crystal growth was observed in r = 0.1. This growth was not present at lower Δμ values or at r = 0.01.

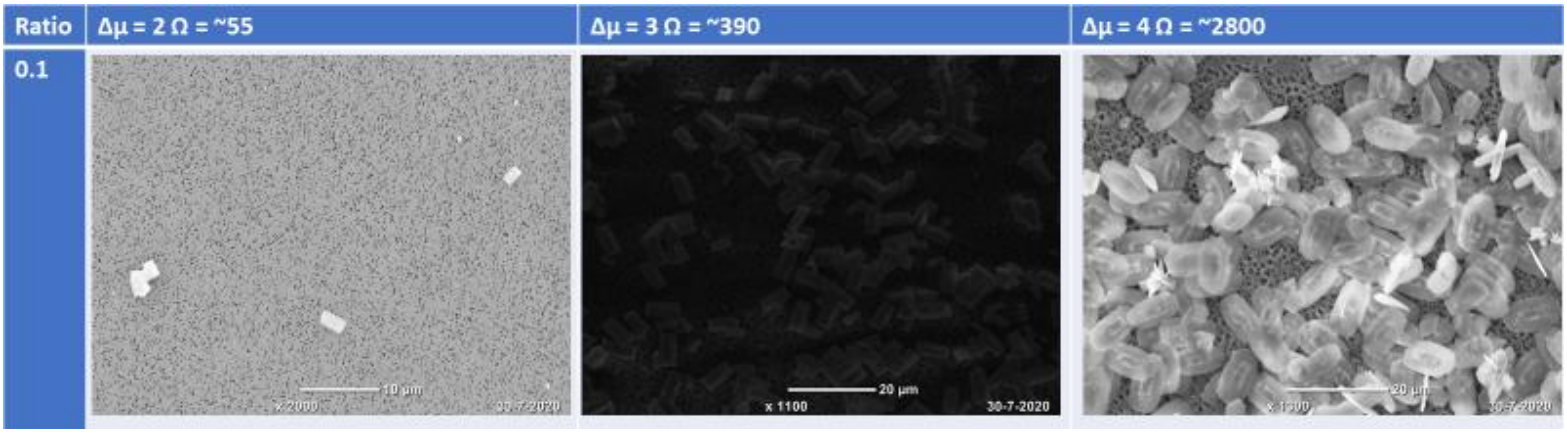

Figure 23: Tabletop SEM results of no additional BE baryte mixtures with a [Ba^{2+}]:[SO_4^{2-}] ratio of 0.1.

Figure 24 shows that again, at r = 1, tabular baryte was the dominant morphology observed in this batch. Interestingly, at Δμ = 2 baryte was more abundant at organic substrates rather than free in solution. More twinning was observed at r = 1 than in r = 0.1 and 0.01 mixtures. Twinning also increased as Δμ increased. Rounding of baryte also occurred with Δμ increase and perpendicular growths were observed at Δμ = 4, like r = 0.1. Again, these growths did not occur at lower Δμ values. The only Δμ = 7 mixture created was with an r value of 1. The baryte morphology observed at this concentration was small, highly rounded, tabular crystals. These formed one continuous layer of baryte.

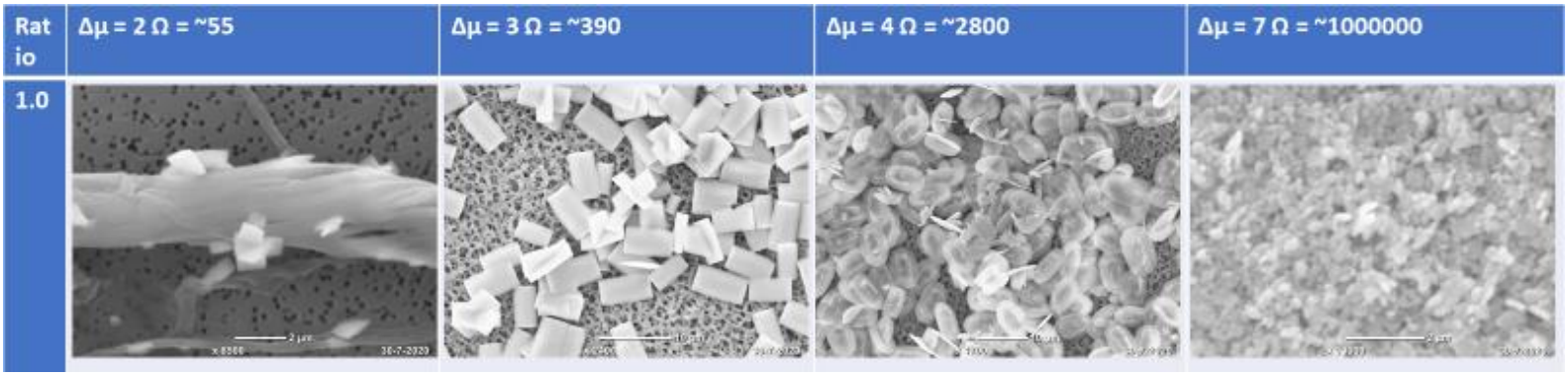

Figure 24: Tabletop SEM results of no additional BE baryte mixtures with a $[Ba^{2+}]$:$[SO_4^{2-}]$ ratio of 1.

Figure 25 shows tabular baryte crystallisation especially on organic substrates at Δμ = 2 for r = 10 mixtures. Twinning was difficult to identify under the SEM because the crystals were small and scarce at Δμ = 2. Tabular crystals with occasional twinning were observed at both at Δμ = 3 and 4. Rounding also increases with Δμ. At Δμ = 4, the perpendicular growth had disappeared, resulting in a flat, rounded morphology.

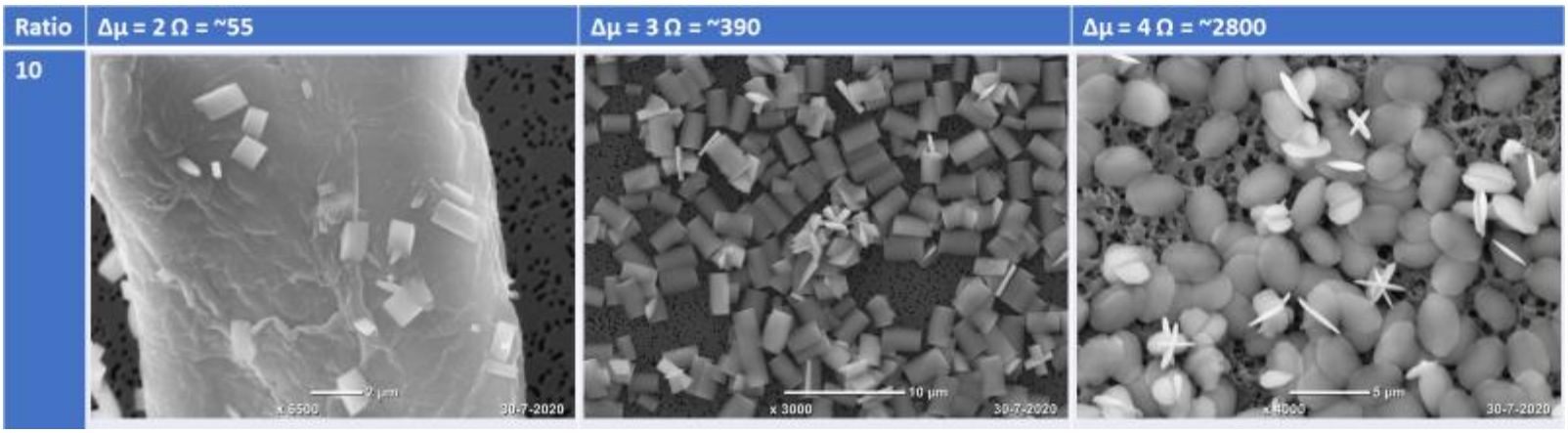

Figure 25: Tabletop SEM results of no additional BE baryte mixtures with a $[Ba^{2+}]:[SO_4^{2-}]$ ratio of 10.

Figure 26 shows that for the r = 100 mixture, a similar tabular morphology was observed at Δμ = 2 compared to lower r values but twinning was more abundant than in other Δμ = 2 mixtures. Another baryte morphology was also observed, this structure was shorter and narrower than tabular baryte with more rounded edges resembling the morphology identified in Δμ = 7. A tabular morphology was observed at Δμ = 3 with an increase in twinning compared to Δμ = 3 at lower r values and at lower Δμ values. At Δμ = 4, twinning was highly abundant forming small rosettes, highly characteristic of abiotic baryte growth (Widanagamage et al., 2018).

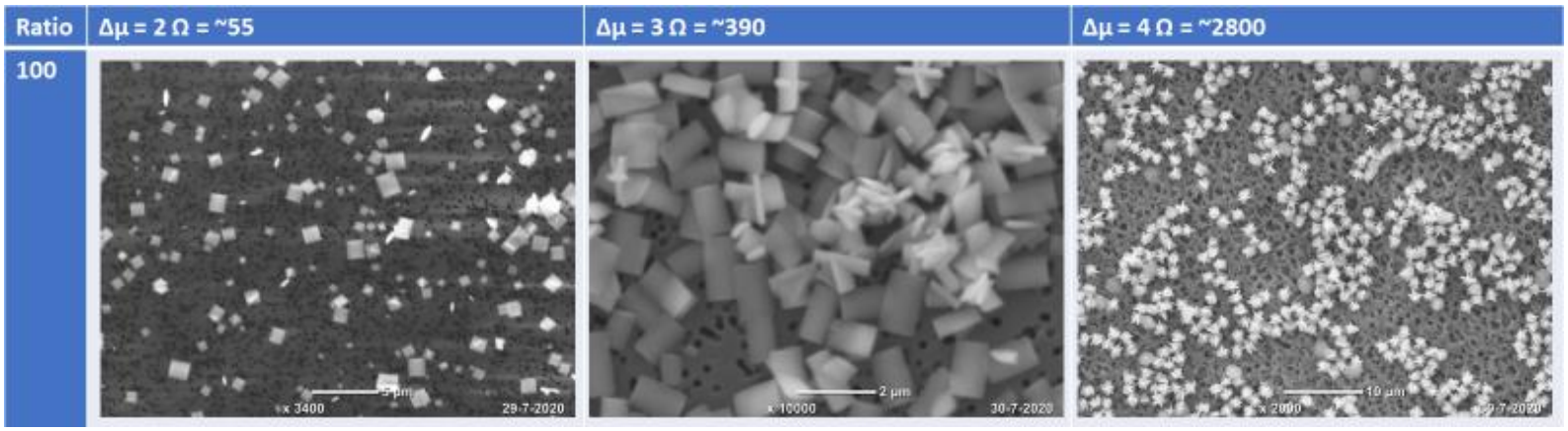

Figure 26: Tabletop SEM results of no additional BE baryte mixtures with a $[Ba^{2+}]:[SO_4^{2-}]$ ratio of 100.

4.4.2. Crystallising Baryte with Additional NaCl as Background Electrolyte (BE)

4.4.2.1. Crystal Sizes. Figure 27 shows the changes in crystal sizes as a function of Δμ, showing that growth increases as Δμ increases. At Δμ = 2, growth is limited for all mixtures but at Δμ = 5, r = 1 showed the largest crystals whilst baryte in solutions with an r values of 0.1 and 10 were on average larger than baryte in solutions of r = 0.01 and r = 100. In all cases in this batch, a SO_4^{2-} rich environment resulted in larger crystals than a Ba^{2+} rich environment.

Extreme stoichiometries resulted in no difference in crystal size at Δμ = 4.

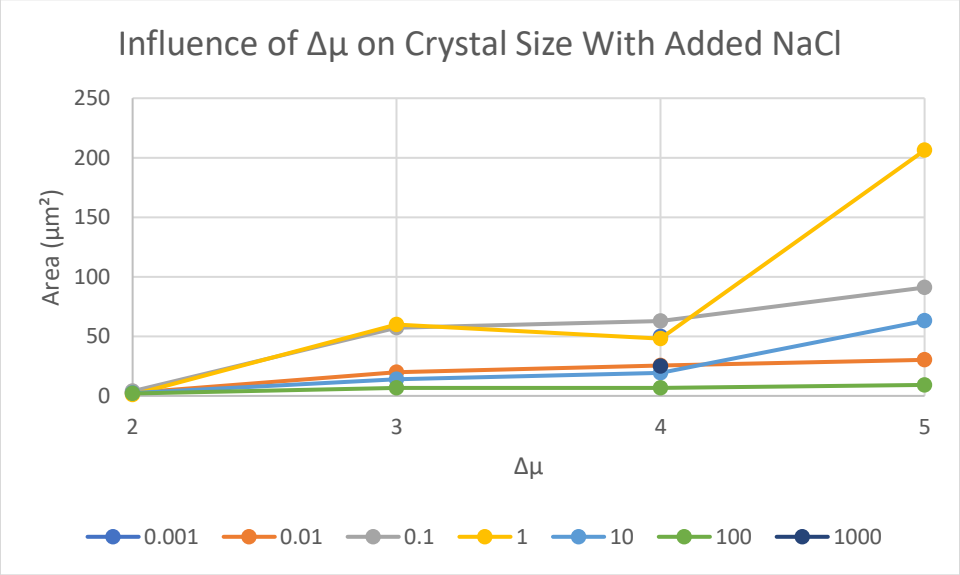

Figure 27: Change in crystal size as a function of Δμ for each stoichiometric system in the solutions with additional NaCl.

4.4.2.2. Crystal Morphologies. Two more non-stoichiometric mixtures were created for all additional BE solutions. These included r = 0.001 (Figure 28A) and r = 1000 (Figure 28B). These solutions were only created in a Δμ = 4 solution. The crystal habit identified at r = 0.001 was tabular with pointed edges and very little twinning was observed. Unlike at r = 1000 which exhibited primarily twinning to create a rosette crystal habit. Some crystals also exhibited a more tabular crystal habit which were slightly larger than the rosettes.

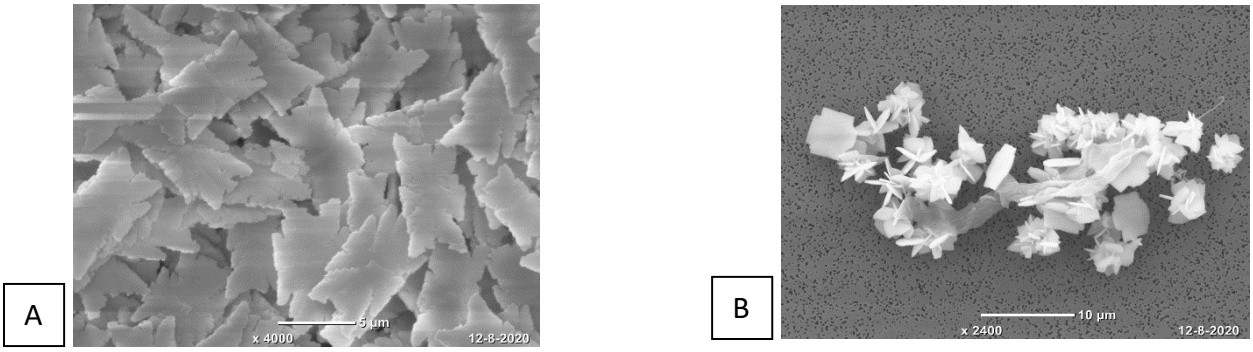

Figure 28: Tabletop SEM results with additional NaCl as BE baryte mixtures with a $[Ba^{2+}]:[SO_4^{2-}]$ ratio of 0.001 (A) and 1000 (B), both at Δμ = 4.

Figure 29 shows that tabular crystals are observed at different Δμ at r = 0.01, ranging in size and shape. At Δμ = 2, tabular crystals are narrow with straight sides with little twinning observed. Δμ = 3 shows an increase in twinning compared to Δμ = 2 and baryte which is almost hexagonal. This sides of which also are more equal in length. At Δμ = 4, a more tabular shape is observed with irregular edges and little twinning and at Δμ = 5 a more rounded, tabular morphology is observed, also with little twinning.

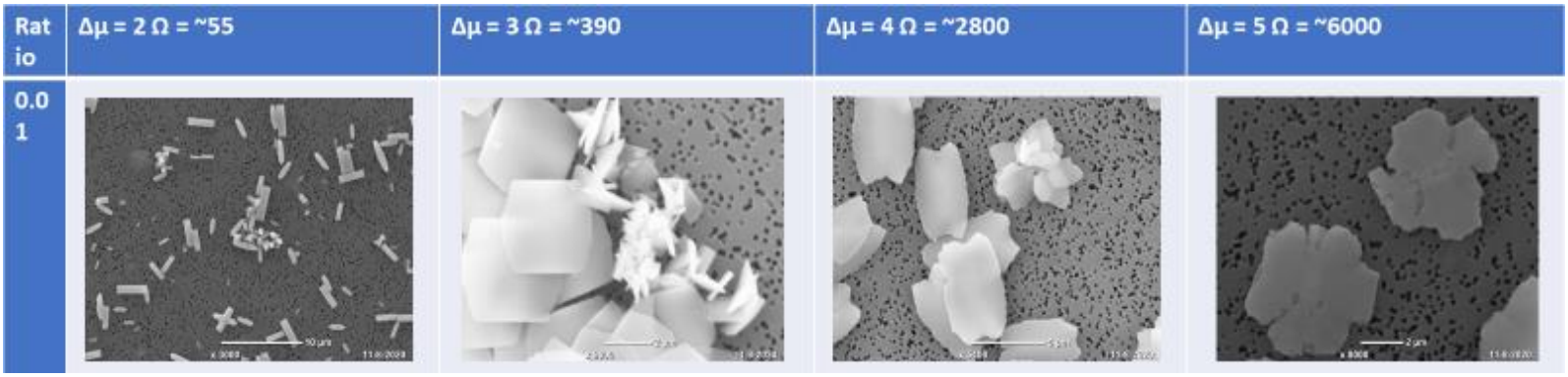

Figure 29: Tabletop SEM results with additional NaCl as BE baryte mixtures with a $[Ba^{2+}]:[SO_4^{2-}]$ ratio of 0.01.

Figure 30 shows that tabular crystals are also observed at r = 0.1. At Δμ = 2, small, narrow, straight sided tabular crystals were observed. Small amounts of twinning were also identified. At Δμ = 3, the tabular baryte was wider than at Δμ = 2 with more twinning. At Δμ = 4, baryte was more rounded than at Δμ = 3 but twinning was not observed as much. At Δμ = 5, baryte was observed to be more rhombic than at lower Δμ, whilst the thickness of baryte was still negligible. Small perpendicular growths were also observed at Δμ = 5 in the centre of the crystals.

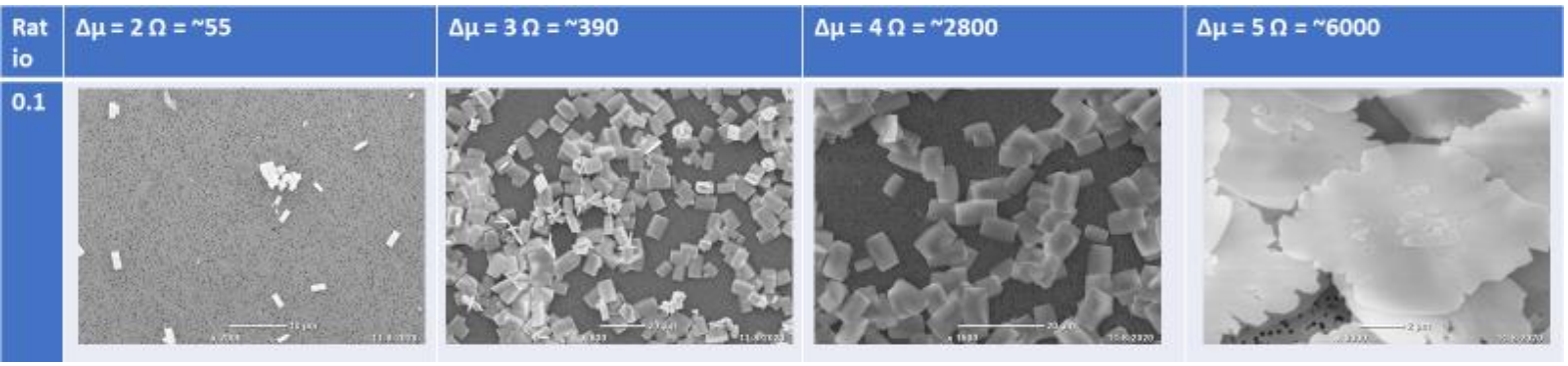

Figure 30: Tabletop SEM results with additional NaCl as BE baryte mixtures with a $[Ba^{2+}]:[SO_4^{2-}]$ ratio of 0.1.

Figure 31 shows tabular baryte at Δμ = 2, 3 and 4. Δμ = 2 shows small, narrow tabular baryte with straight edges and some twinning. Again, at Δμ = 3, baryte was wider and more twinning was observed than at Δμ = 2. Both more rounding and more twinning was observed at Δμ = 4 than at Δμ = 3. Baryte at Δμ = 5 was more different. The morphology of baryte at Δμ = 5 was more representative of a wheat sheaf crystal habit with perpendicular growth mainly at the centre of the baryte crystals.

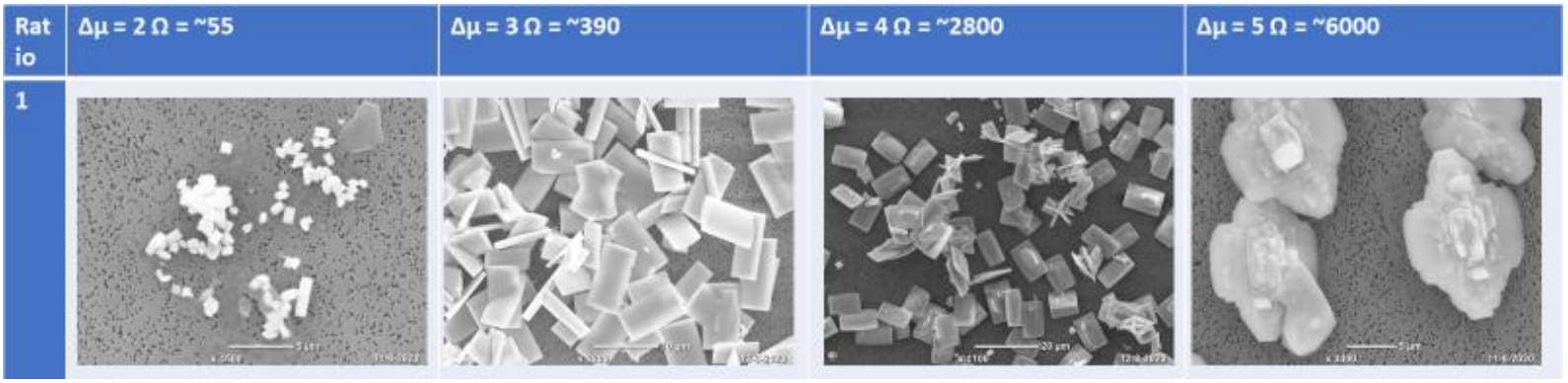

Figure 31: Tabletop SEM results with additional NaCl as BE baryte mixtures with a $[Ba^{2+}]:[SO_4^{2-}]$ ratio of 1.0

Figure 32 shows similar morphologies between r = 1 and r = 10 at all equivalent Δμ values. Tabular morphologies were observed at Δμ = 2, 3 and 4 whilst Δμ = 5 exhibited more of a wheat sheaf crystal habit. Twinning also increased with Δμ and baryte was more rounded at Δμ = 4 than at Δμ = 3, which was more rounded than at Δμ = 2.

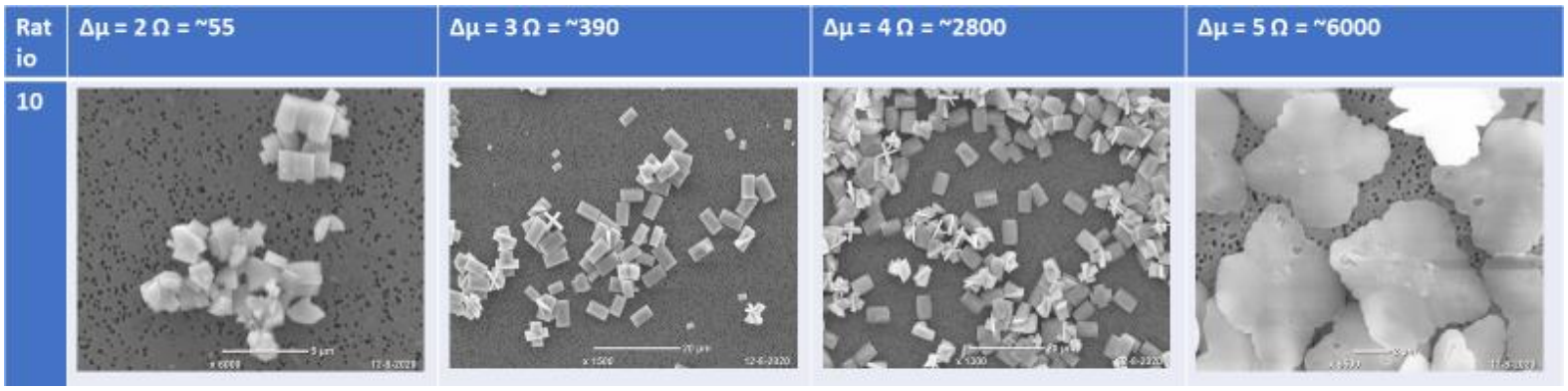

Figure 32: Tabletop SEM results with additional NaCl as BE baryte mixtures with a $[Ba^{2+}]:[SO_4^{2-}]$ ratio of 10.

Figure 33 shows a tabular morphology at all Δμ values. Twinning was abundant in all mixtures at r = 100. A uniform tabular crystal is difficult to identify at Δμ = 2 due to the high amount of twinning. At Δμ = 3, the sample contained a mixture of tabular non-twinned baryte and twinned rosette baryte. The twinned rosette baryte was more abundant but tabular baryte was still observable. At Δμ = 4, twinned, rosette baryte was the primary morphology observed with very few tabular crystals. The Δμ = 5 mixture was again different, very little twinning was observed, the tabular crystals were highly rounded, and no perpendicular growth was observed on the surface of the crystals.

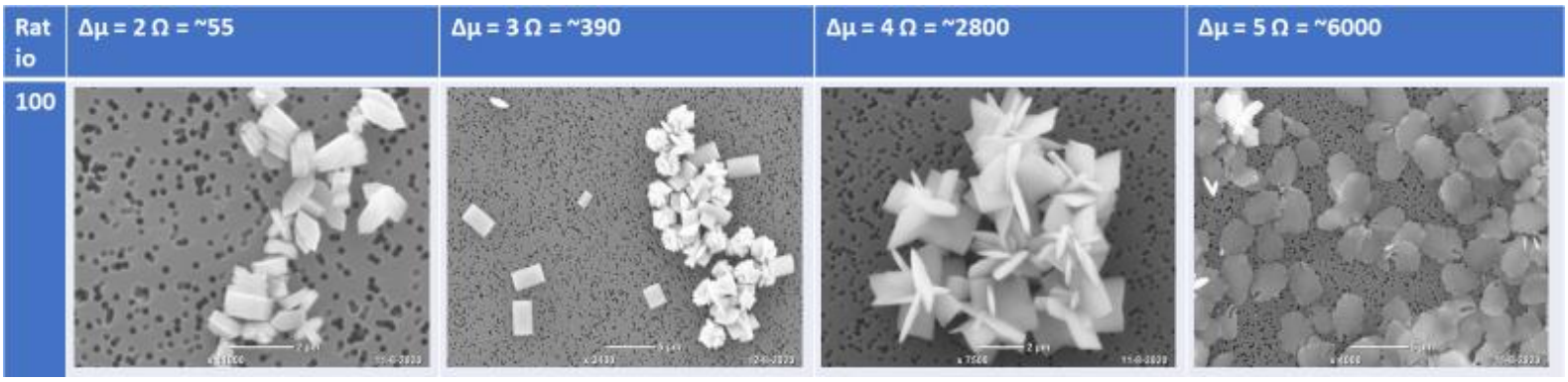

Figure 33: Tabletop SEM results with additional NaCl as BE baryte mixtures with a $[Ba^{2+}]:[SO_4^{2-}]$ ratio of 100.

4.4.3. Crystallising Baryte with Additional $NaNO_3$ as Background Electrolyte (BE)

4.4.3.1. Crystal Sizes. The crystal sizes in general increased as Δμ increased when Na^+ and NO_3^- were the background electrolytes (BE). The size of baryte at r = 0.01 increase from ~2 μm^2 to ~20 μm^2 to ~800 μm^2 to over 1200 μm^2 from Δμ = 2 to Δμ = 5. A similar pattern was observed for the other stoichiometric systems: r = 0.1 increased from 1.5 μm^2 to 48 μm^2 to 560 μm^2 to almost 1400 μm^2 between Δμ = 2 and Δμ = 5. Baryte growth was less intense for r = 1 from indetermined sizes at Δμ = 2, 48 μm^2 at Δμ = 3, 256 μm^2 at Δμ = 4 and 625 μm^2 at Δμ = 5. For r = 10, the largest crystal growth was observed between Δμ = 4 and Δμ = 5 with crystal sizes increasing from ~2 to ~80 to ~220 μm^2 between Δμ = 2 and Δμ = 4 but 1350 μm^2 at Δμ = 5. Baryte grew modestly in the r = 100 mixtures increasing from 8 to ~24 to ~230 to 450 μm^2 between Δμ = 2 and Δμ = 5. For extreme non-stoichiometric values of r = 0.001 and r = 1000, growth was significantly hindered compared to smaller stoichiometric differences. In both cases, baryte neither at r = 0.001 nor r = 1000 exceeded a height x width of 10 μm^2 with r = 1000 growing a crystal of 2 μm^2 and r = 0.001 growing a crystal of ~8 μm^2 (Figure 34).

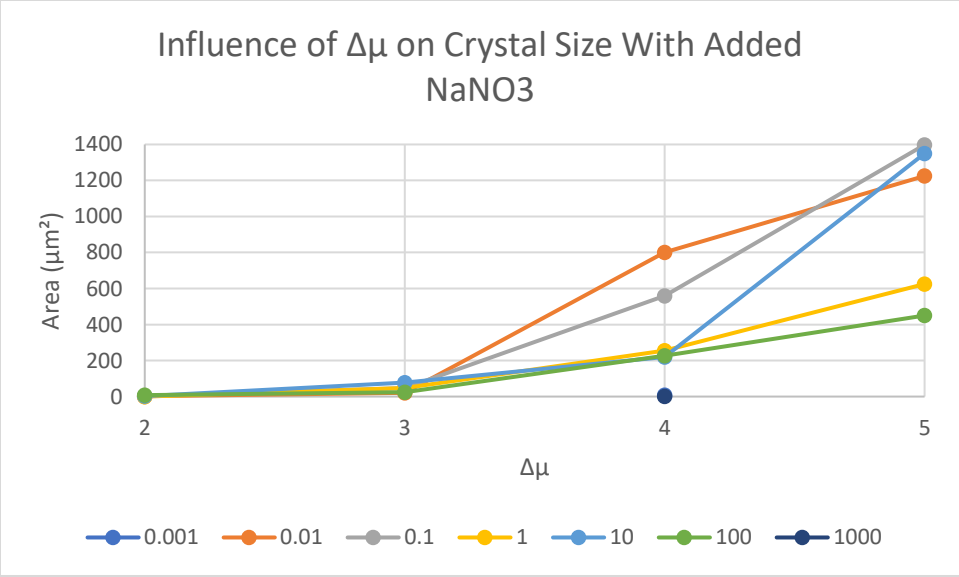

Figure 34: Change in crystal size as a function of Δμ for each stoichiometric system in the solutions with additional $NaNO_3$.

4.4.3.2. Crystal Morphologies. SEM results of non-stoichiometric extremes of r = 0.001 and r = 1000 are shown in Figure 35A and B, respectively. An 'x – shaped', tabular crystal habit was observed in baryte at r = 0.001 with slight twinning. At r = 1000, rosettes were the common crystal habit observed with occasional tabular crystals.

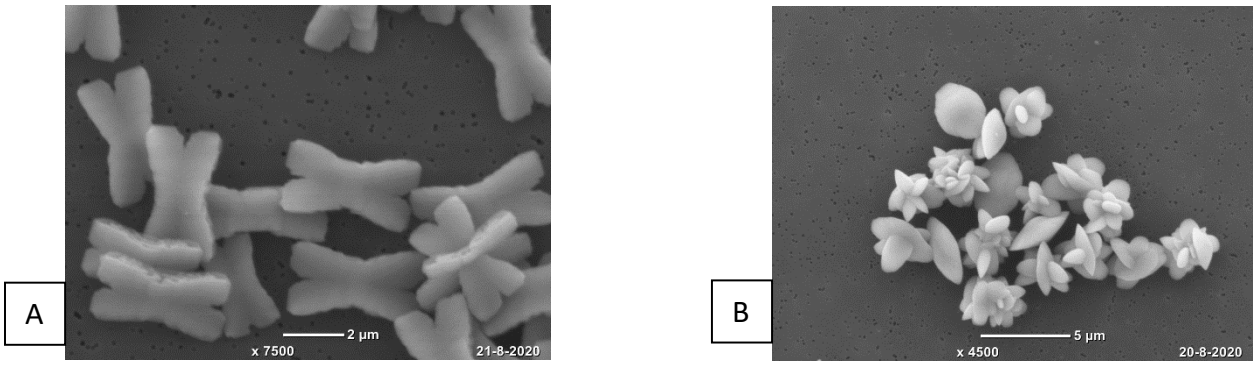

Figure 35: Tabletop SEM results with additional NaCl as BE baryte mixtures with a $[Ba^{2+}]:[SO_4^{2-}]$ ratio of 0.001 (A) and 1000 (B). Both solutions were grown at Δμ = 4.

Figure 36 shows the influence of Δμ on the r = 0.01 mixtures with additional $NaNO_3$. More unusual morphologies were observed at r = 0.01 compared to NaCl as BE and without additional BE. At Δμ = 2, the baryte exhibited a rhombic crystal habit as a 'diamond' shape was observed. Tabular baryte was observed at Δμ = 3 with more twinning observed than at Δμ = 2. At Δμ = 4, an 'x – shaped' morphology was observed. This morphology is more common in baryte saturated solutions with excess sulphate (Boon & Jones, 2016), however was not observed in the no additional BE batch or the additional NaCl batch. At Δμ = 5, a wheat sheaf crystal habit was observed with almost dendritic limbs growing away from the centre of the crystal. This created uneven and pointed edges, not characteristic of a wheat sheaf crystal habit. These crystals were unusually large with very little twinning observed.

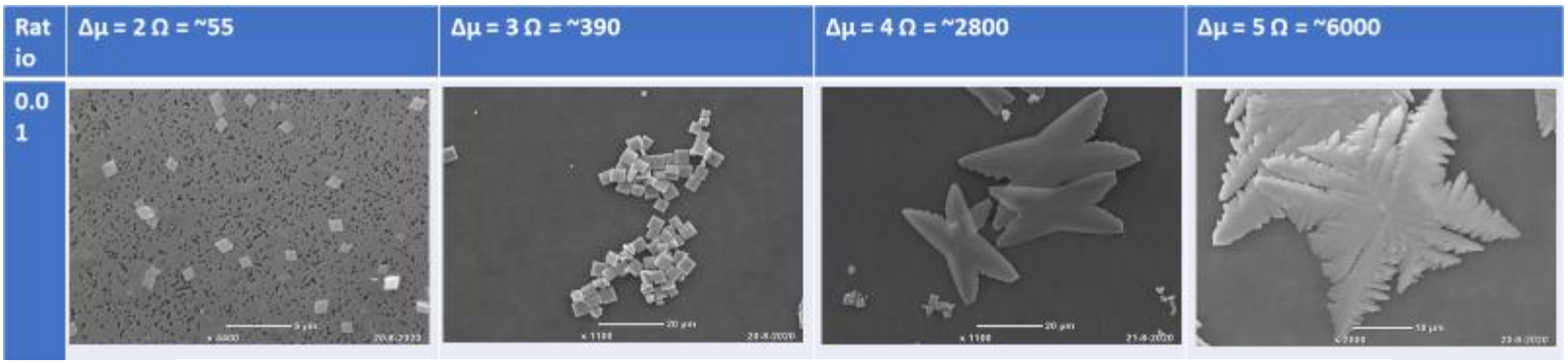

Figure 36: Tabletop SEM results with additional NaCl as BE baryte mixtures with a $[Ba^{2+}]:[SO_4^{2-}]$ ratio of 0.01.

Figure 37 shows a similar morphology of baryte between Δμ = 2, r = 0.01 and 0.1. A small, rhombic crystal habit was observed with little twinning. At Δμ = 3, crystals were more tabular and exhibited more twinning than at Δμ = 2, r = 0.1. A similar 'x – shaped' morphology was observed at Δμ = 4 and a more characteristic wheat sheaf morphology was observed at Δμ = 5. Twinning was not widespread at either Δμ = 4 or 5.

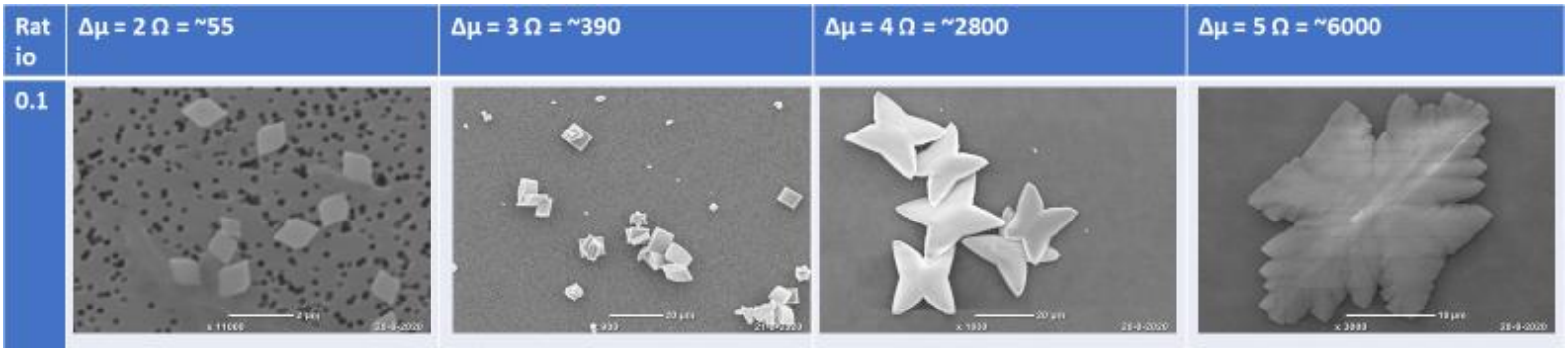

Figure 37: Tabletop SEM results with additional NaCl as BE baryte mixtures with a $[Ba^{2+}]:[SO_4^{2-}]$ ratio of 0.1.

Figure 38 shows the morpohlogy of baryte at r = 1. Unfortunately, due to a lack of crystals forming no data was made available for Δμ = 2. Tabular crystals were observed at both Δμ = 3 and Δμ = 4 with more twinning observed at Δμ = 4. At Δμ = 5, a wheat sheaf crystal habit was observed. A very small amount of perpendicular growth was present at both Δμ = 4 and Δμ = 5.

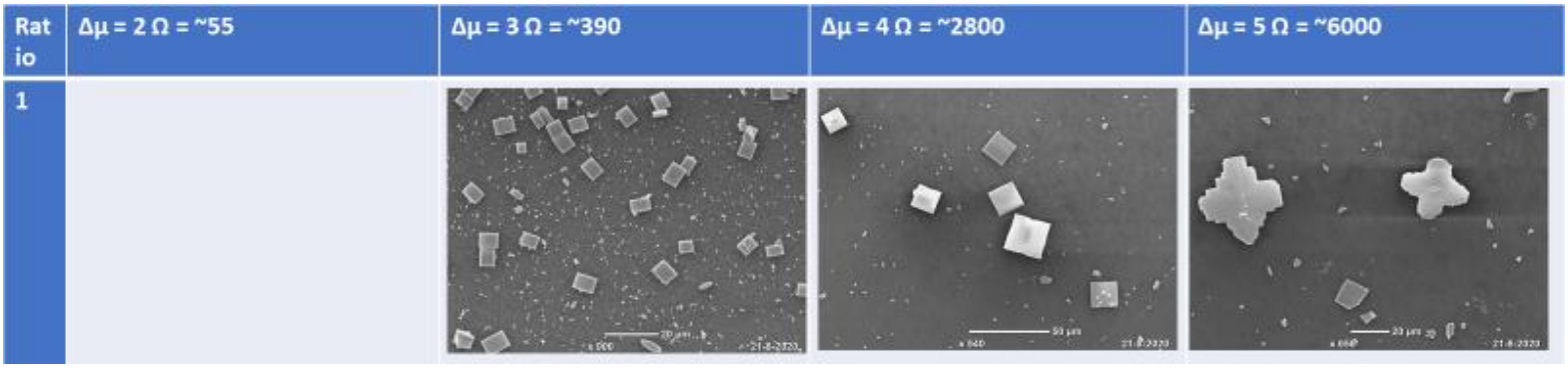

Figure 38: Tabletop SEM results with additional NaCl as BE baryte mixtures with a $[Ba^{2+}]:[SO_4^{2-}]$ ratio of 1.0.

Figure 39 shows baryte crystallised at r = 10 with a rhombic crystal habit at Δμ = 2, a highly twinned, tabular crystal habit at Δμ = 3, a hexagonal, tabular crystal habit with occasion perpendicular

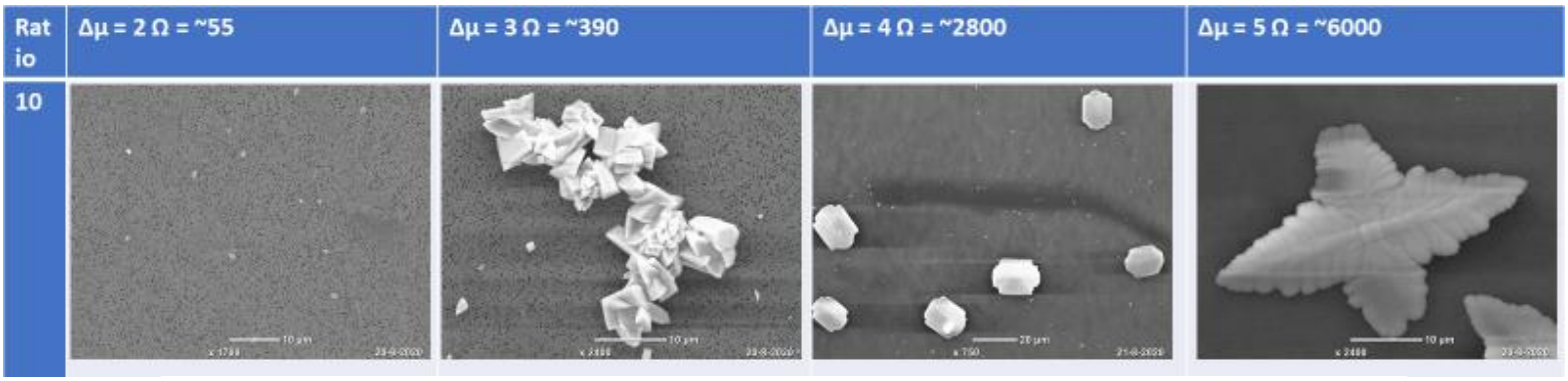

Figure 39: Tabletop SEM results with additional NaCl as BE baryte mixtures with a $[Ba^{2+}]:[SO_4^{2-}]$ ratio of 10.

growth at Δμ = 4 and an elongated wheat sheaf crystal habit at Δμ = 5 exhibiting very little twinning.

Figure 40 shows the morphology of baryte crystals at r = 100 showing rounded, tabular crystals at Δμ = 2, with very little twinning. At Δμ = 3, highly twinned tabular crystals were observed at Δμ = 3. A wheat sheaf crystal habit was observed at Δμ = 4 and an elongated, pointed wheat sheaf crystal habit was observed at Δμ = 5. Again, at both Δμ = 4 and 5, very little twinning was observed.

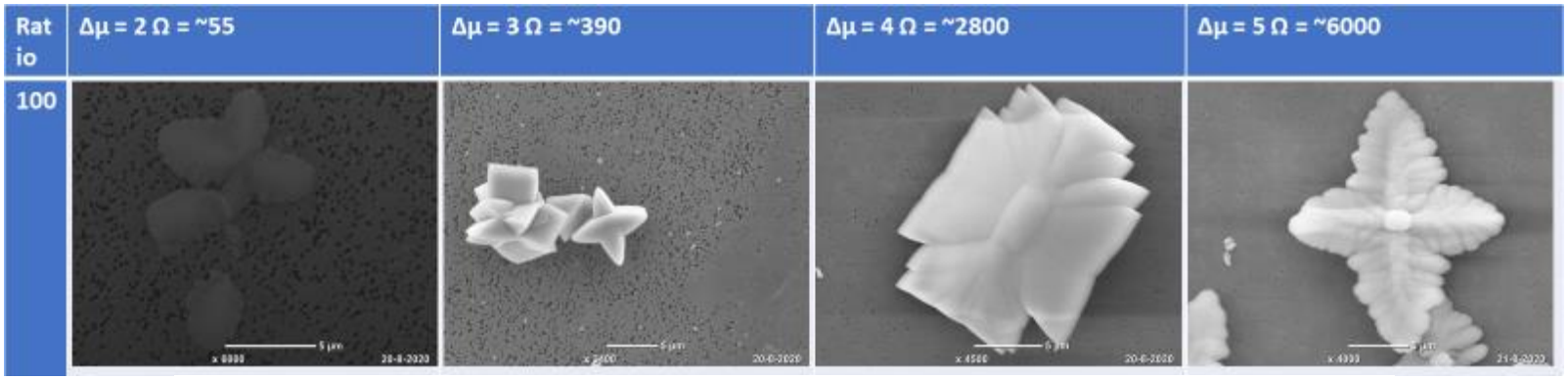

Figure 40: Tabletop SEM results with additional NaCl as BE baryte mixtures with a [Ba^{2+}]:[SO_4^{2-}] ratio of 100.

4.4.4. Crystallising Baryte with Additional KCl as Background Electrolyte (BE)

4.4.4.1. Crystal Sizes. When KCl was the BE, the largest crystal observed were found in the r = 1 solutions. All other solutions grew in crystal size until Δμ = 5 when the baryte crystals in the r = 0.1 solution grew, containing larger crystals than r = 10, r = 100 and r = 0.01. The crystal size did not change much between Δμ = 4 and 5 in the r = 10 solution, whilst the crystal sizes of r = 0.01 and 100 both decreased between Δμ = 4 and 5. Extreme r values of 0.001 and 1000 resulted in small crystals compared to the other solutions with less extreme r values at the same Δμ (Figure 41).

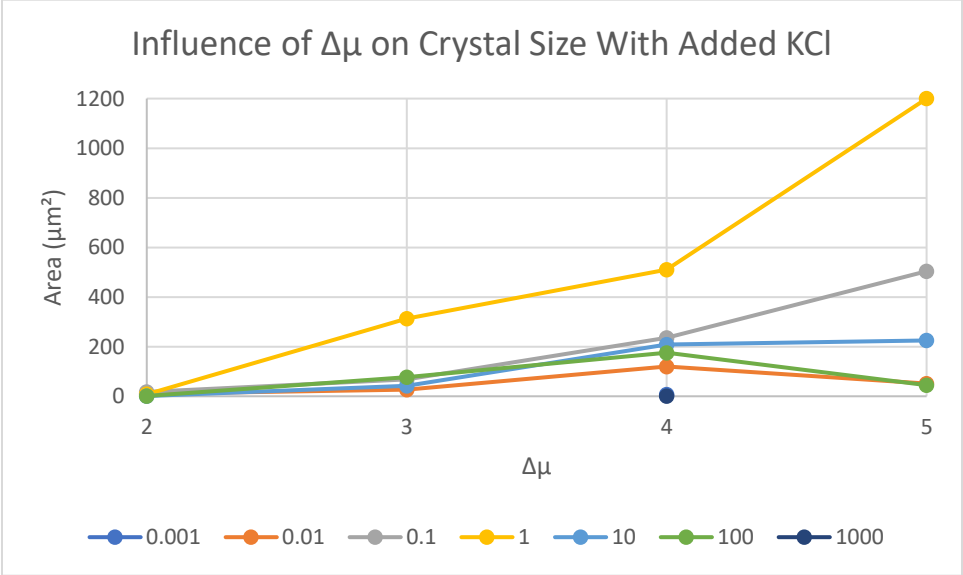

Figure 41: Change in crystal size as a function of Δμ for each stoichiometric system in the solutions with additional NaNO3.

4.4.4.2. Crystal Morphologies. The SEM results of r = 0.001 and r = 1000 for the Δμ = 4 solutions with added KCl are shown in Figure 42A and B. At r = 0.001, a straight sided, tabular crystal habit was identified and at r = 1000, mainly rosettes with few, highly rounded, tabular crystals were observed, the tabular plates being larger than the rosettes.

A

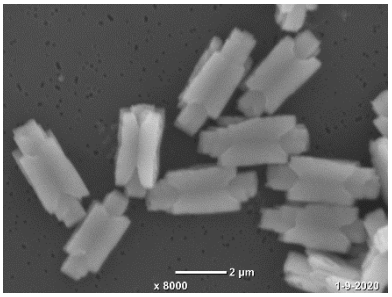

B

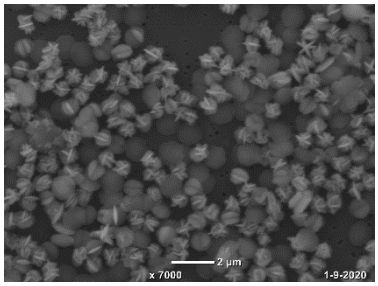

Figure 42: Tabletop SEM results with additional NaCl as BE baryte mixtures with a $[Ba^{2+}]:[SO_4^{2-}]$ ratio of 0.001 (A) and 1000 (B). Both solutions were grown at Δμ = 4.

Approximately hexagonal, tabular crystals were observed at all concentrations when KCl was the BE (Figure 43). Twinning was not widely observed in any r = 0.01 experiments, but the morphology of these tabular crystals did change. The smoothness of the sides of baryte decreased with increasing Δμ. At Δμ = 2 and 3, the baryte crystals were more hexagonal whilst at Δμ = 4 and 5, a wheat sheaf crystal habit began to develop, more so at Δμ = 5 than at Δμ = 4.

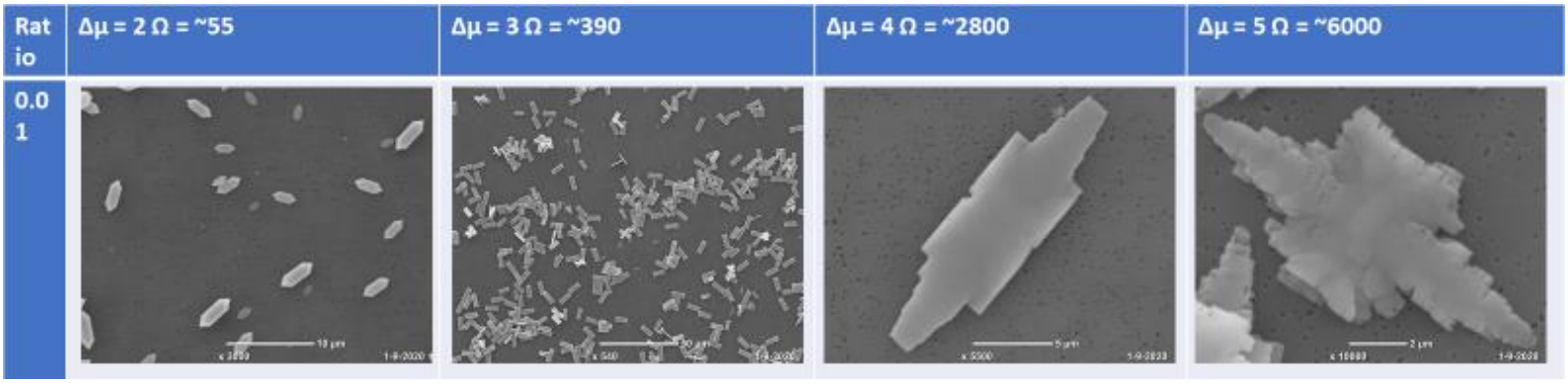

Figure 43: Tabletop SEM results with additional NaCl as BE baryte mixtures with a $[Ba^{2+}]:[SO_4^{2-}]$ ratio of 0.01.

Figure 44 shows tabular crystals increasing with irregularity as Δμ increases. At Δμ = 2, baryte exhibited a slight hexagonal shape. At Δμ = 3, baryte was less hexagonal, more tabular as crystals were wider. At Δμ = 4, a wheat sheaf crystal habit began to develop but the sides were unusual and concave.

At Δμ = 5 a wheat sheaf crystal habit had developed but less elongation was observed compared to r = 0.01.

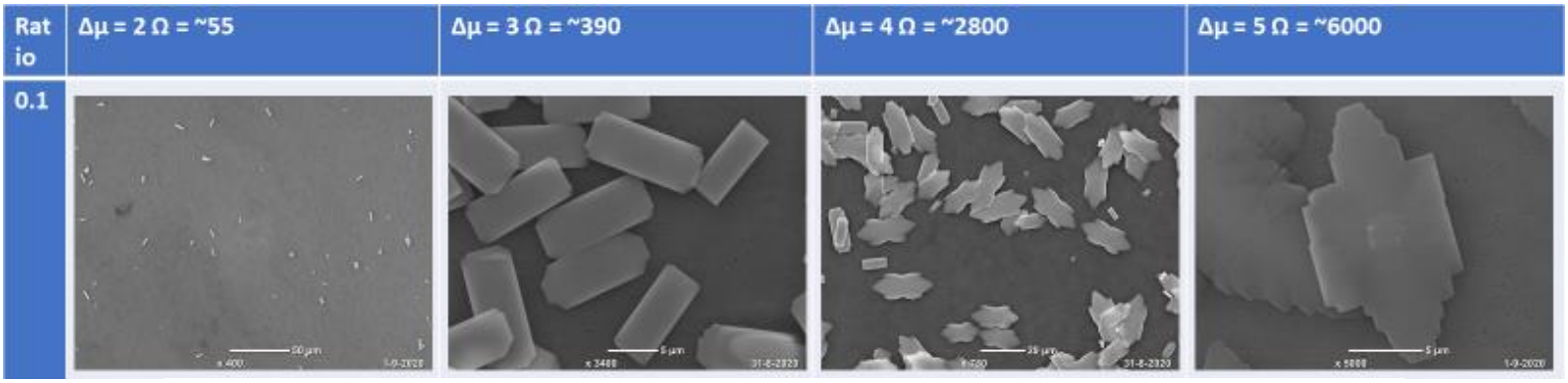

Figure 44: Tabletop SEM results with additional NaCl as BE baryte mixtures with a $[Ba^{2+}]:[SO_4^{2-}]$ ratio of 0.1.

The baryte crystalised at r = 0.1 is like baryte crystallised at r = 1. Tabular crystals were observed at Δμ = 2, 3 and 4 with baryte at Δμ = 4 being more hexagonal. This baryte exhibited perpendicular growth on the surface. A wheat sheaf crystal habit was observed at Δμ = 5 with dominant perpendicular growth on the crystal surface. Twinning is present but not dominant at r = 1 the amount of twinning does not increase with Δμ (Figure 45).

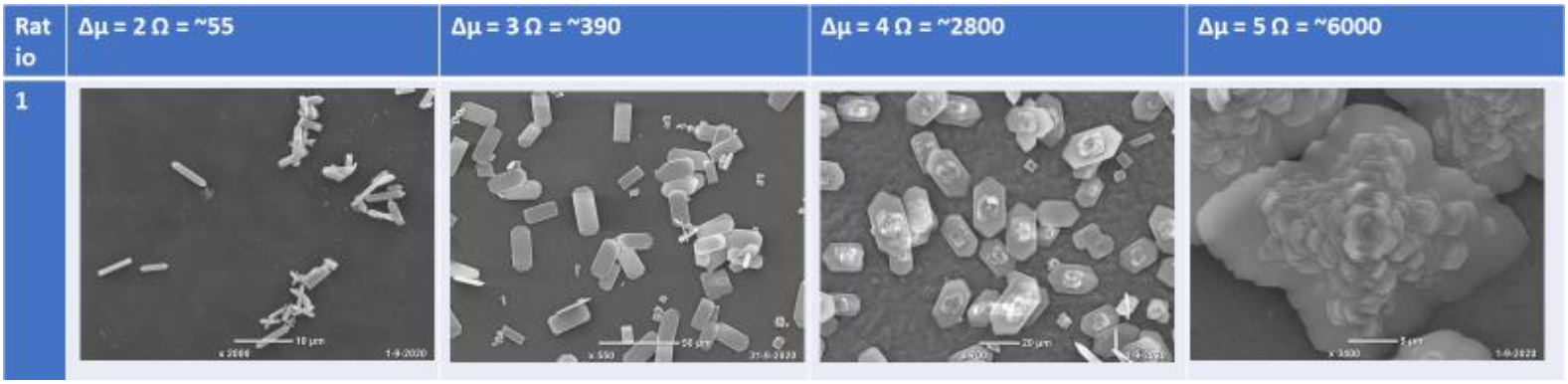

Figure 45: Tabletop SEM results with additional NaCl as BE baryte mixtures with a $[Ba^{2+}]:[SO_4^{2-}]$ ratio of 1.0.

The baryte crystallised at r = 10 was largely tabular but more hexagonal at lower Δμ values and more rounded as Δμ increased. At Δμ = 5 a wheat sheaf crystal habit was observed, and twinning was not abundant in any sample (Figure 47).

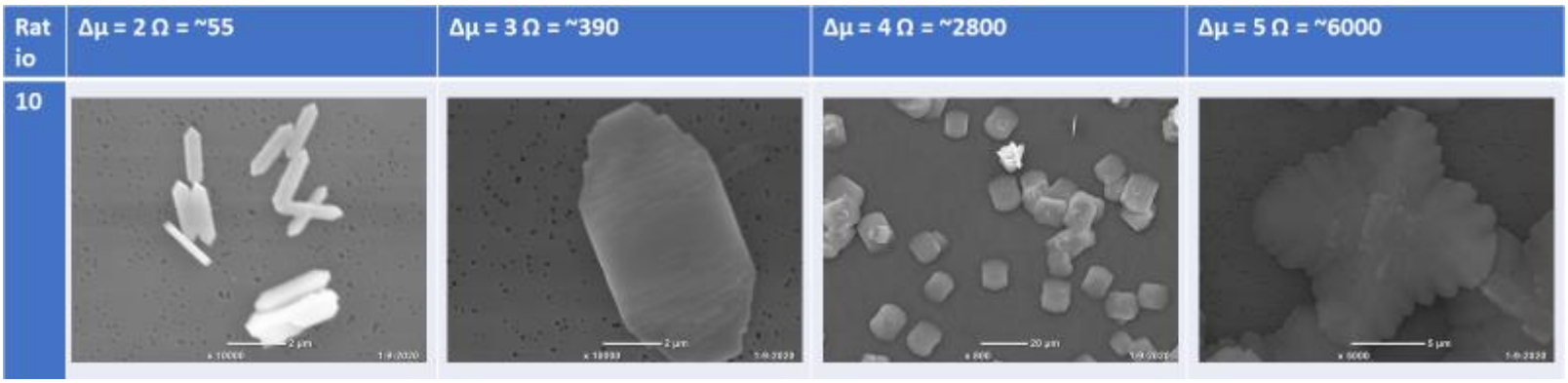

Figure 47: Tabletop SEM results with additional NaCl as BE baryte mixtures with a $[Ba^{2+}]:[SO_4^{2-}]$ ratio of 10.

At r = 100, more twinning was observed compared to lower r values (Figure 46). Whilst tabular crystals were observed at Δμ = 2 and 3, small, highly twinned rosettes were observed at Δμ = 4 and wheat sheafs were observed at Δμ = 5. Tabular crystals were more hexagonal at Δμ = 2 and more rounded at Δμ = 3.

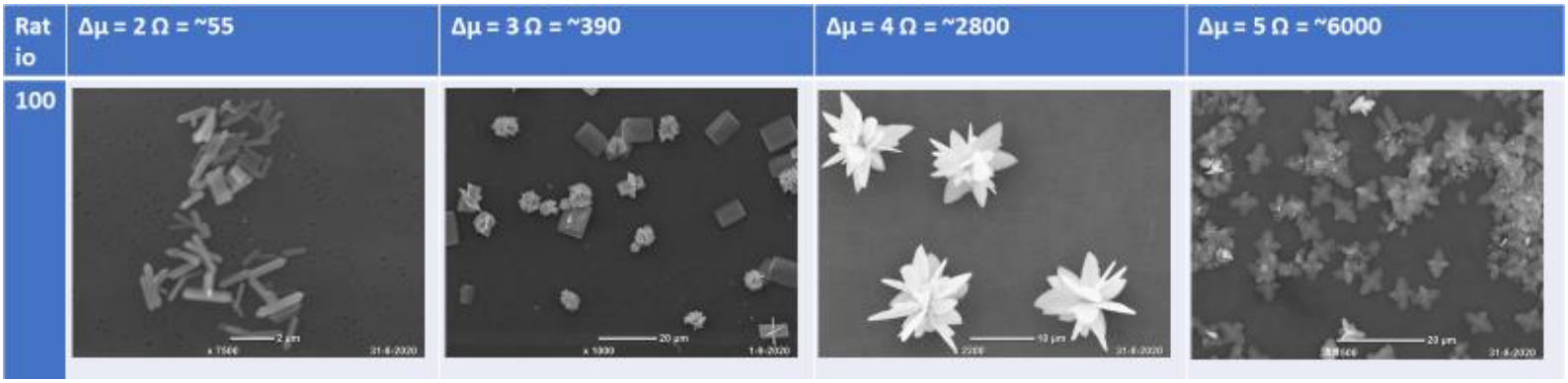

Figure 46: Tabletop SEM results with additional NaCl as BE baryte mixtures with a $[Ba^{2+}]:[SO_4^{2-}]$ ratio of 100.

5. Discussion

5.1. Accuracy of CG Simulations

As far as we were aware, this was the first instance of baryte simulation using CG. This resulted in a limited determination of appropriate interaction energies, crucial to determining the morphology of simulated baryte. Another set-back at the time of writing this report included the fact that no graphic user interface was present, increasing the complexity of running simulations and the time taken to set-up a simulation to run. Regardless, patterns emerged from crystallographic information provided by CG showing that in all simulations, a (001) and (100) plane were identified. This observation was shared by Sánchez-Pastor et al. (2006) and Bosbach et al.(1998). However, differences also occur including the topography of the (001) surface as the presence of a screw dislocation results in “growth in opposite directions in different 1 half-unit cell layers” (Bosbach et al., 1998, Pina et al., 1998). This meant specifically that for a half-unit cell grown on the surface of the screw dislocation, a growth direction of either [100] or [-100] is preferred sequentially, referred to as a 2_1 screw dislocation (Figure 48). A screw dislocation is commonly observed growing on the (001) plane as this plane is described as a perfect cleavage plane (Alpers et al., 2018, Patel & Koshy, 1968).

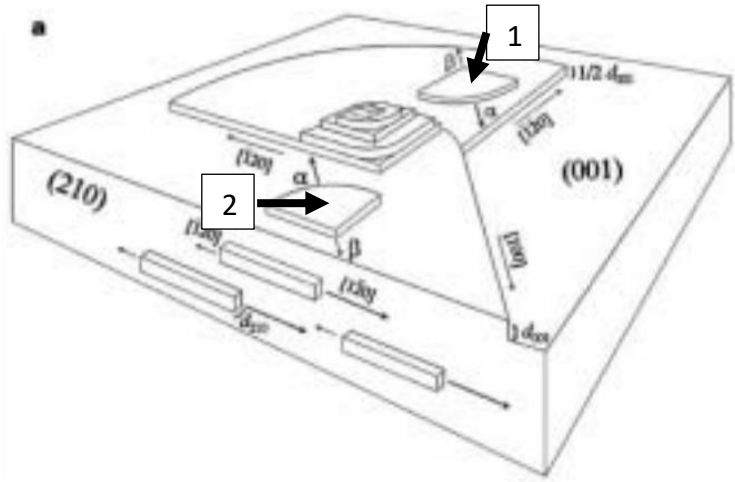

Figure 48: Example of baryte crystallography showing a single crystal with a 2_1 screw dislocation. Image edited from Pina et al. (1998). 1 – preferential growth in the [100] direction. 2 – preferential growth in the [-100] direction.

To replicate this topography the bond energies between interaction type 2 and interaction type 3, determined in molecular.txt, would have to be slightly different, however the exact difference could not be constrained. Other inconsistencies include the recurring observation of a (210) plane and (101) plane (Vitel et al., 2020). Whilst CG did recognise these faces occasionally, namely the (101) plane at extreme non-stoichiometric conditions and the (210) plane between $\Delta\mu = 3$ and 5 between $r = 0.1$ and $r = 10$, these planes are commonly observed in AFM results (Bracco et al., 2016, Vital et al., 2020, Weber et al., 2018). The fact that these planes were not more observed shows that the interaction energies constrained were not entirely accurate.

5.2. SEM Results (This Research) Compared to Previous Research

To replicate the observed baryte morphology in the SEM images, the experiments performed had to be reproducible. The morphology of baryte has been widely researched at varying conditions and experimental set-ups. To determine whether this research was reproducible, similar morphologies had to have been observed by previous research to show that the current results are not unusual.

Kucher et al., 2006, shows that when the concentration of $BaCl_2$ and Na_2SO_4 are kept constant (with no added electrolytes) in a titration set-up, the concentrations required for what was observed at $\Delta\mu = 7$

or on the scale of 10^5 Ω in this research was observed at Ω = 750 or a Δμ ~3.857. At Ω = 750, Kucher et al., 2006, observed many small (<0.5 μm) baryte nodules, making one continuous baryte sheet. The reason why the morphologies are similar at such different supersaturations is likely due to the controlled supersaturation of titration experiments, resulting in a continuous abundance of both Ba^{2+} and SO_4^{2-}, whilst the batch experiments which were performed in this research eventually reached equilibrium, requiring a higher initial concentration to increase baryte crystallisation before the growth rate decreases to the point no baryte growth occurs.

Other experiments where baryte nanoparticles were observed include Schwarzer & Peukert, 2002, where baryte nanoparticles began to form on the scale of microseconds at supersaturations of ~17400 Ω or ~6 Δμ in batch experiments. Ruiz-Agudo et al., 2015, provides a model behind baryte nanoparticle crystallisation and includes two occasions of oriented aggregation of nanoparticles, firstly during the transition from baryte nuclei to nanoparticles and secondly during the aggregation of these nanoparticles (Figure 49). Whilst the morphology of nanoparticles is poorly defined, the aggregations of nanoparticles often vary in morphology. Multiple authors including Kucher et al., 2006 and Ruiz-Agudo et al., 2015, made similar SEM observations of baryte having a flat surface with growths extending away. Kucher et al., 2006, showed a morphology more like Δμ = 5, r = 1 and r = 10 (with added NaCl), whilst Ruiz-Agudo et al., 2015, showed baryte morphology more representative of Δμ = 4, r = 1 (with added NaCl) or Δμ = 4, r = 0.1 and r = 1 (without added NaCl).

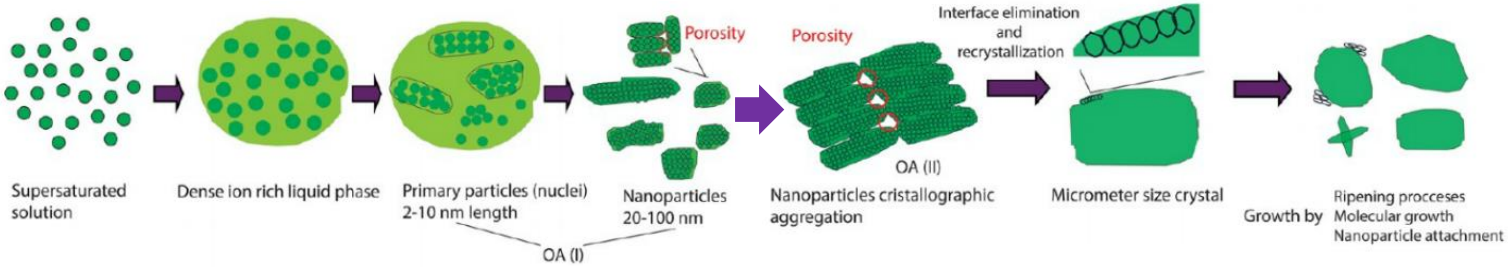

Figure 49: Diagram of baryte nucleation, crystallisation, and ripening. Diagram edited from Ruiz-Agudo et al., 2015. Encircled red regions indicate porosity, OA = oriented aggregation.

Judat & Kind, 2004, observed similar morphologies to Kucher et al., 2006 and Ruiz-Agudo et al., 2015, in their titration experiments as well as morphologies in this research (Figure 50). Again, these experiments kept the supersaturation constant at Ω = 50, 250, 1000, 2500 and 5000. These values equate to approximately Δμ = 2.279, 3.216, 4.024, 4.558 and 4.961, respectively. Judat & Kind, 2004, found that at their lowest supersaturation (Ω = 50), the morphologies observed closely represented experiments at Δμ = 4, r = 0.1 and 1 with no additional NaCl and r = 0.1 with additional NaCl, where baryte is a flat plate with a growth on the surface. At higher Ω, Judat & Kind, 2004, observed baryte morphology akin to, but more pronounced than this experiment at Δμ = 5, r = 1 and r = 10, the shape being an irregular four-sided star with platelets growing on the surface. Judat & Kind, 2004, also identify nanoparticles of baryte at Ω = 5000.

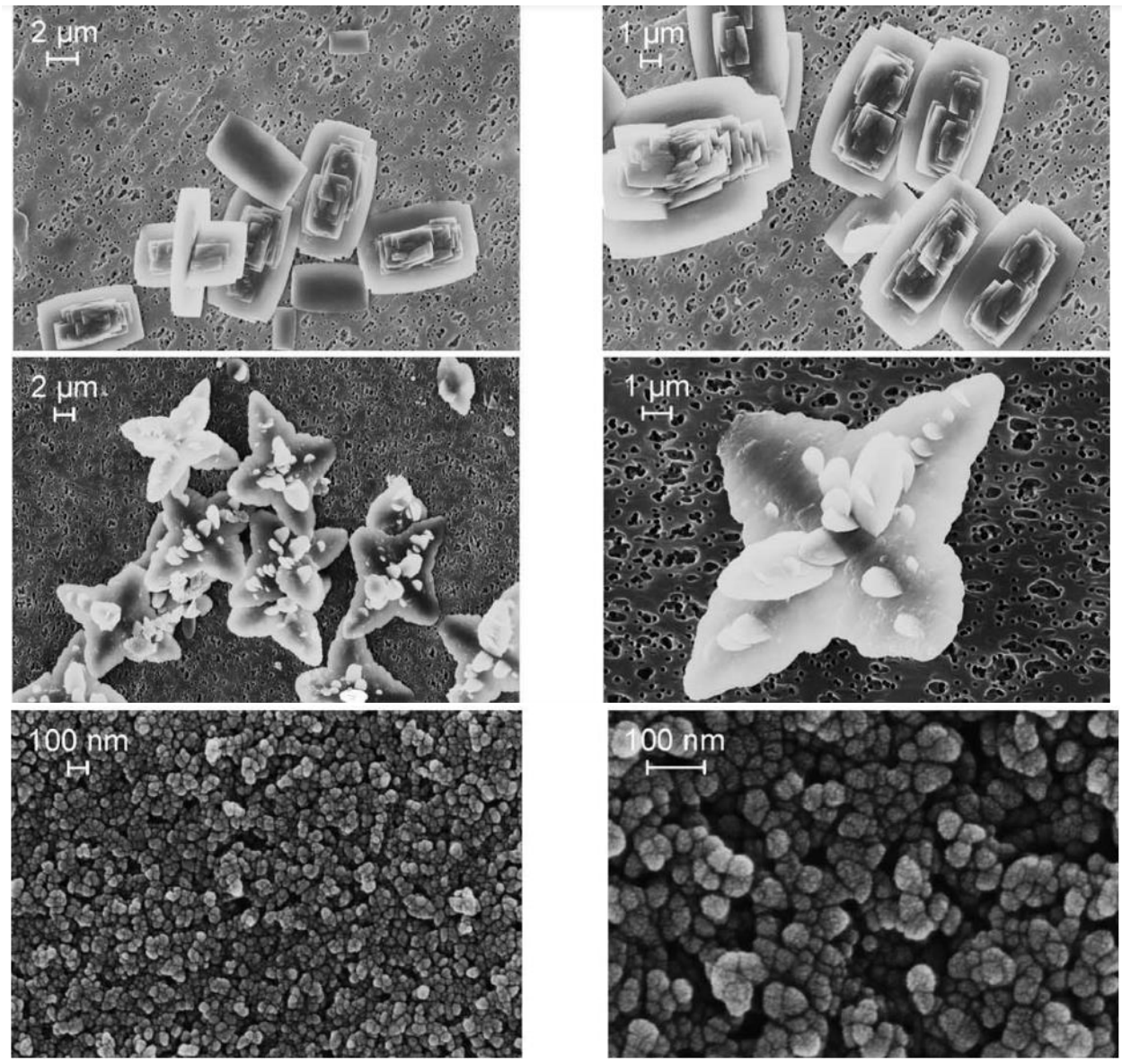

Figure 50: SEM images of baryte at Ω = 50, 250 and 5000. Images were edited from Judat & Kind, 2004.

Suito & Takiyama, 1952, showed that using different reagents to crystalise baryte resulted in similar morphologies documented in this research (Figure 51). Their technique involved the mixing of $BaOH_2$ and H_2SO_4. Whilst the surfaces of baryte are unclear in the electron micrographs produced, the outline of baryte crystals showed similar patterns to what was synthesised for this research. The range of concentrations for $BaSO_4$ ranged from 1.0 mol/L to 0.0001 mol/L. Whilst exact sizes of crystals are difficult to determine, when the concentration of $BaSO_4$ = 0.1 mol/L, the results were similar to Judat & Kind, 2004, with an irregular cross shape. The pointed edges are less prominent in the electron micrographs of Suito

& Takiyama, 1952, compared to Judat & Kind, 2004, and more closely represent baryte observed in this research. Twinning, platy baryte and rounded baryte is also observed throughout different $BaSO_4$ concentrations. Another pattern observed is that at highest concentrations, the crystals are smaller, the exact sizes were difficult to determine but like Judat & Kind, 2004, Ruiz-Agudo et al., 2015, Kucher et al., 2006 and this study, no obvious morphological features were discernible.

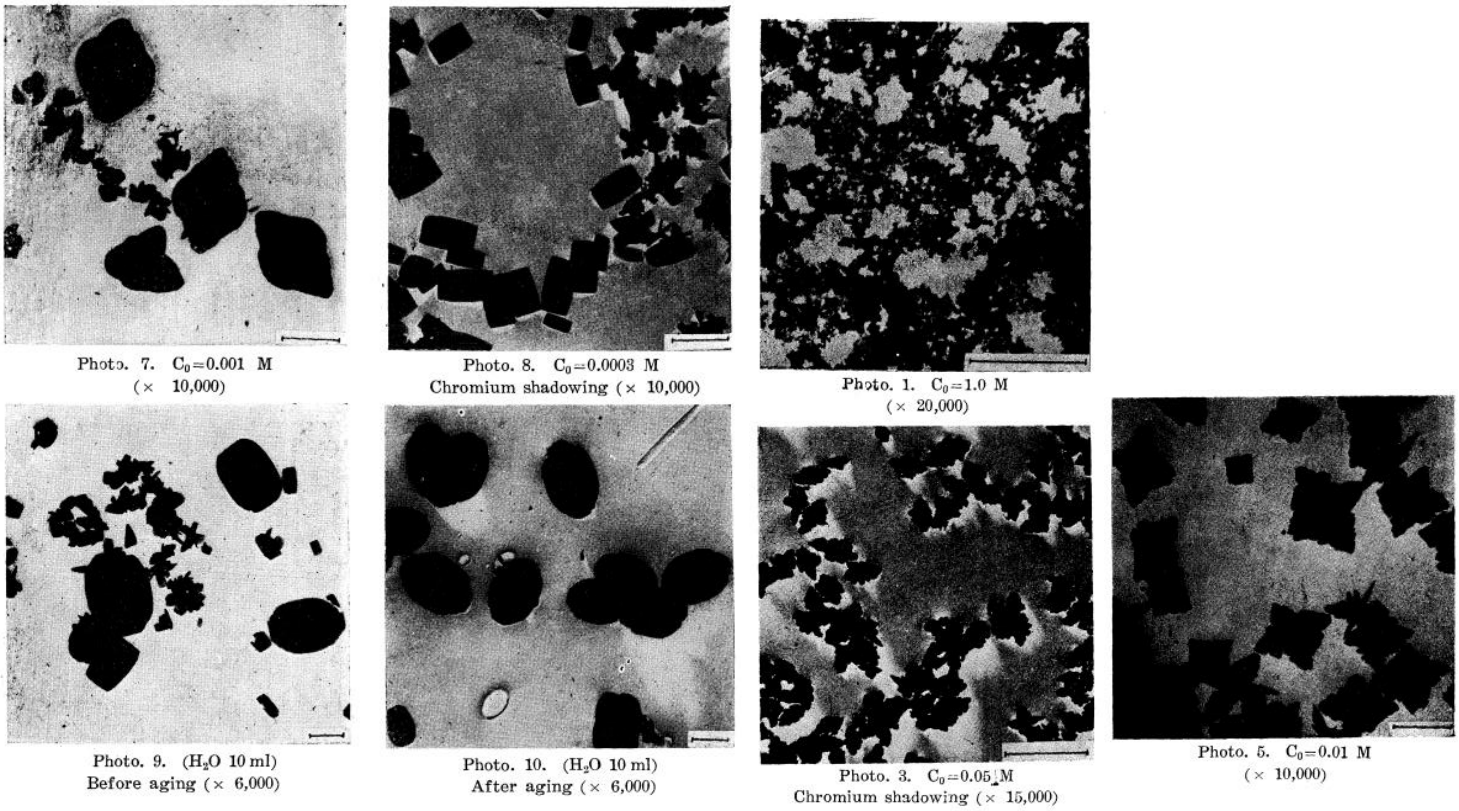

Figure 51: Electron Micrographs of $BaSO_4$ from mixing $BaOH_2$ and H_2SO_4. C_0 shows the concentration of $BaSO_4$. Images were edited from Suito & Takiyama, 1952.

Comparing the SEM images from this research with SEM images of other master students A. Baken and D. Riedinger, shows that the method of growing baryte influences the morphology of baryte greatly. Baken, who used a titration setup used a similar Ω to this research and created enough individual baryte crystals to determine a morphology whilst Riedinger. (2020), used a batch setup, and created more dissimilar morphologies to both this research and that of Baken. Clearly the experimental setup has a

significant influence on the morphology of baryte. Using the forementioned examples, this SEM research and CG simulations, how can the depositional environment of Archean baryte be constrained?

5.3. How can CG or SEM Results Help Constrain the Archean Environment for Future Research?

This project tested concentration, stoichiometry, and ionic strength to identify these factors' influences on the crystal habit of baryte. Extrapolating these crystal habits to Archean baryte is challenging due to the lack of constraints inferred because of deformation and metamorphic events that occurred between baryte deposition and current baryte observations. Another important factor to remember is that the Archean environment was very different to what we can observe today, in that in the Archean eon, gypsum ($CaSO_4$ $2H_2O$) and anhydrite ($CaSO_4$) deposits were rare compared to baryte (Busigny et al., 2017, Pavlov & Kasting, 2002). The area of discussion focussed on in this project is the precipitation of baryte in low ionic strength or high ionic strength. This has been interpreted as either meteoric water (Lowe et al., 2019) or shallow marine water (Roerdink et al., 2012). Their research suggests that baryte deposition was limited by sulphate concentrations rather than barium unlike what is observed today in ocean water with sulphate concentrations of approximately 0.0282 mol/kg (Morris & Riley, 1966).

Archean baryte has largely been researched on the macroscopic scale (cm to m) to show the baryte structures formed during deposition. There is a striking between baryte structures observed in South Africa (Lowe et al., 2019) and Western Australia (Nijman et al., 1999) with diagrams compared in Figure 52. Both diagrams show the source of baryte growth coming from a fault, resulting in baryte "mounds" directly above the fault and forming "bladed" baryte away from the fault. Lowe et al., 2019, shows a decrease in coarsening of baryte blades as the distance from the fault increases, whilst Nijman et al., 1999, shows coarser baryte blades stratigraphically above finer baryte blades. Both models are potentially accurate as weathering and erosion can decrease the coarseness of baryte at the surface whilst burial of baryte would result in compression, causing a possible decrease in grin size. The source of barium in these

models was probably the fluid reaching the surface through the fault, the question remains however, was the source of sulphate meteoric water (Lowe et al., 2019) or was a stratified shallow ocean present (Nijman et al., 1999)?

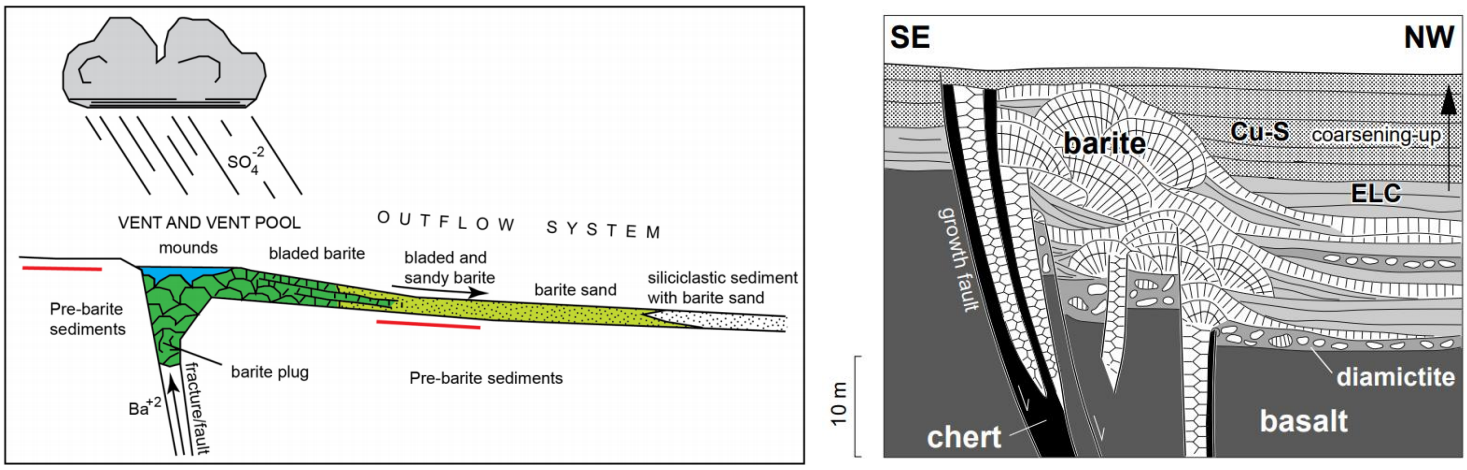

Figure 52: Diagrams of baryte formation in South Africa (Left, edited from Lowe et al. (2019)) and Western Australia (Right, edited from Nijman et al. (1999).

To answer this question, further microscopy studies on Archean baryte crystals are required to help identify the morphology of individual baryte crystals, especially if any screw dislocations are visible at the surface. Whilst previous research has attempted to comprehend the depositional environments of baryte, the morphology of baryte has not been used to constrain the factors that influence these environments. For example, salinity of the Archean ocean has been constrained to within an order of magnitude higher than the current average ocean salinity (De Ronde et al., 1997), calculated by fluid inclusions in quartz grains between the contact of the Onverwacht Group and Fig Tree Group in the Barberton Greenstone Belt. Alternatively, a newer study by Marty et al. (2018) suggested Archean ocean salinity was lower, more equivalent to modern ocean salinities.

A similar story exists with determining the Archean ocean and atmospheric temperatures. Previous estimates interpreted ocean temperatures between 55-85°C (Knauth & Lowe, 2003), however more resent evident suggests a more moderate ocean temperature between 26-40°C (Catling & Zahnle, 2020). Oceanic pH variation between 6.4 and 7.4 and atmospheric temperatures between 0 – 40°C were based on computer models by Krissansen-Totton et al. (2018). However, studies have also argued for lower ocean temperatures of ~26°C to 40°C (Blake et al., 2010), based on $\delta^{18}O$ values from phosphates found in the BGB. Another issue with determining atmospheric conditions include the composition of the atmosphere, whilst consensus agrees with an anoxic atmosphere, Catling & Zahnle (2020), modelled the composition of the Archean atmosphere including N_2, O_2, CO_2 and CH_4 (Figure 53). Whilst not likely influencing the morphology of baryte greatly, nucleation and crystallisation would have occurred in a significantly different atmosphere to the present, the effects of which could have included the buffering of oxygen entering the atmosphere (Krissansen-Totton et al., 2018).

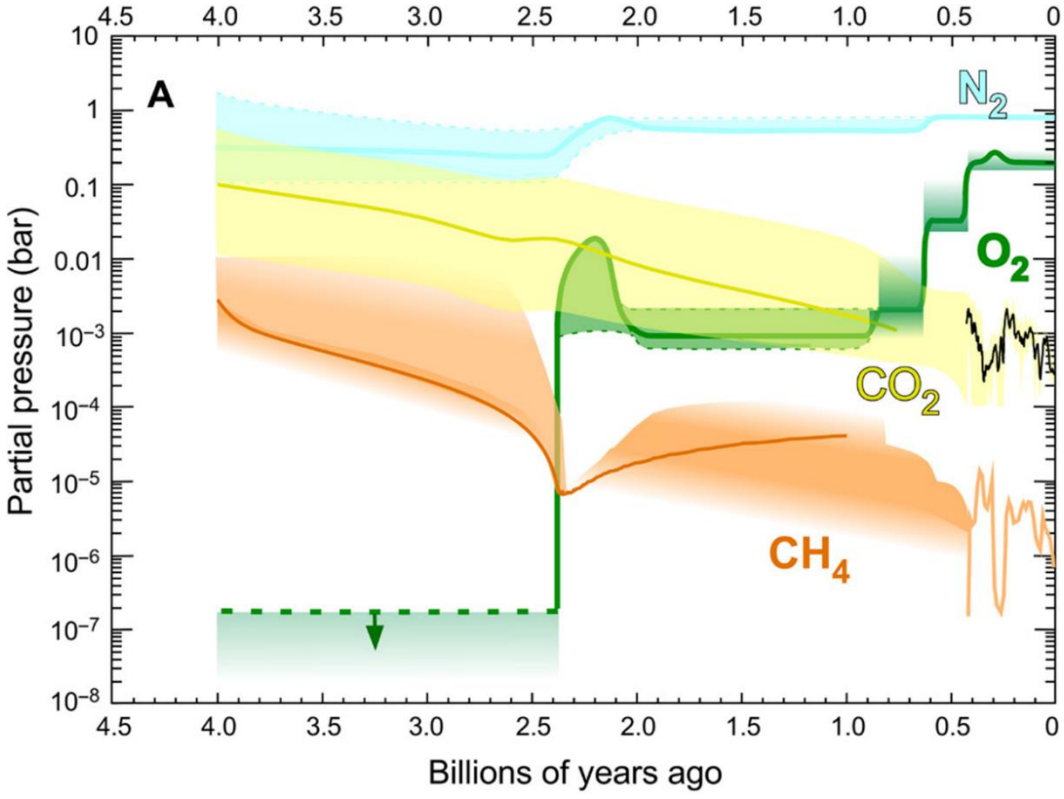

Figure 53: Model of atmospheric composition including CH_4, CO_2, O_2 and N_2 dating back from the Archean to present. Image edited from Catling & Zahnle (2020).

What this report shows is that the size of baryte crystals increases with concentration. This was a pattern observed in all batches besides the one experiment at $\Delta\mu = 7$ (Ω = ~1000000) (Figure 24). The presence of organic substrates could also influence the nucleation and crystallisation at low concentrations of $\Delta\mu = 2$ (Ω = ~50) (Figure 24, Figure 26). The amount of twinning is highly variable, depending on stoichiometry, concentration, and ionic strength. In the case of the no BE batch, twinning was more abundant at higher concentration and higher $[Ba^{2+}]$:$[SO_4^{2-}]$. In the case of the added BE batches, the stoichiometry played a more significant role on the abundance of twinned baryte than concentration. Low and high concentrations of $\Delta\mu = 2$ and 5 resulted in little twinning in any additional BE batch. Concentrations of $\Delta\mu = 3$ and 4 exhibited the most twinning, which increased with $[Ba^{2+}]$:$[SO_4^{2-}]$. Using these observations to constrain the Archean environment, assuming baryte twinning was limited based on observation made by Canet et al. (2014), Heinrichs & Reimer. (1977), Sugitani et al. (2003), then if sulphate was present as a meteoric origin i.e. relatively low ionic strength, then $[Ba^{2+}]+[SO_4^{2-}]$ would have to be a low concentration (~$\Delta\mu = 2$). Alternatively, the depositional environment had a higher ionic strength (shallow marine environment), requiring the $[Ba^{2+}]+[SO_4^{2-}]$ to be at least ~$\Delta\mu = 4$ but lower than ~$\Delta\mu = 7$ to exhibit a low amount of twinning but a decent amount of individual crystal growth.

Whilst extensive work exists around Archean baryte petrography, isotopic fractionations and relationships between surrounding minerals and lithologies (Catling & Zahnle, 2020, Heinrichs & Reimer, 1977, Lambert et al., 1978), Archean baryte research requires more crystal analysis with high resolution microscopy including Atomic Force Microscopy (AFM), Scanning Electron Microscopy (SEM), Transmission Electron Microscopy (TEM) and X-ray Tomography, Energy-dispersive X-ray spectroscopy (EDS) to understand whether the morphology of Archean baryte can be correlated to laboratory synthesised baryte under specific conditions. In laboratory settings, baryte on the µm scale can nucleate and crystallise within hours, whereas Archean baryte had the potential to grow for potentially hundreds of years, resulting in wide, thick geological deposits. Nevertheless, understanding the morphology of the individual

crystals in these formations should, in future research, be compared to laboratory synthesised baryte to understand how the growth environments differ. Comparing these results with CG simulations, however, requires a deeper understanding of the thermodynamics regarding baryte nucleation and crystallisation. For example, models with growth modifiers representing salinity could be simulated to better understand the influence of BE on baryte nucleation and crystallisation.

6. Conclusion

Baryte crystals were simulated at different stoichiometries and concentrations using probability-calculating software, CG, recently developed for morphological analysis of crystalline material. The main determinant of morphology for CG simulations was the interaction energy between the counterions in a unit cell of baryte. Refinement of these energies showed that interactions with growth influencing thickness had to be limited due to the thin baryte crystals observed in SEM imagery. Different stoichiometries were simulated using a change in concentration rather than changing the ratio of seven different interaction energies as the seven different energies could not be constrained between a unit cell of baryte (4 Ba^{2+} + 4 SO_4^{2-}), only for a single ion.

Several batch experiments, growing baryte at different stoichiometries, concentrations and reagents were carried out. The different stoichiometries varied from 0.001 [Ba^{2+}]:[SO_4^{2-}] to 1000 [Ba^{2+}]:[SO_4^{2-}]. The concentrations varied from ~30 Ω to over 1000000 Ω. The reactions nucleating and crystallising baryte included: $BaCl_2$ + Na_2SO_4 (to which I was present), $BaCl_2$ + Na_2SO_4 (+ NaCl), $BaNO_3$ + Na_2SO_4 + ($NaNO_3$) and $BaCl_2$ + K_2SO_4 + (KCl).

The results of the CG simulations show a tabular/rhombic morphology representing previously observed AFM data (Pina et al., 1998). Clear planes were identified including the (001) and (100) plane, both growing at r = 1 between Δμ = 2 and 3, whilst all other simulations showed no growth of these planes. Other planes occasionally identified included the (210) and (101) planes. The (210) planes were only occasionally observed between Δμ = 3 and 5, between r = 0.1 and 10. The (101) planes were only observed at r = 0.001 and r = 1000.

The results of the laboratory experiments included the general patterns of increased twinning in [Ba^{2+}]>[SO_4^{2-}] batches. At lower concentrations, more tabular crystals were observed. As concentration increased, perpendicular growth was observed on the flat surfaces. At high concentrations, baryte

became overall more rounded as morphologies became more varied, especially when different reagents were used. A common morphology at high concentrations included a wheat sheaf crystal habit.

Potential constraints could be determined for the depositional environment of Archean baryte. If the assumptions that twinned Archean baryte is barely observed and that $[Ba^{2+}]>[SO_4^{2-}]$ hold true then Archean baryte could have nucleated and crystallised in either low salinity environments at low concentrations, potentially with the aid of organic substrates, or in a higher salinity environment at higher concentrations, below a non-stoichiometric ratio of r = 1000. Further constraining of the salinity, concentrations, and stoichiometry would require further laboratory experiments at different ionic strengths, non-stoichiometric ratios, and concentrations.

Further research regarding CG and SEM imagery could be to further constrain Archean baryte using high resolution microscopy, spectroscopy, X-ray tomography, and diffraction to determine the morphology of individual Archean baryte crystals and compare these results to laboratory synthesised baryte.

Acknowledgements

I would like to thank Dr. Mariette Wolthers, Dr. Paul Mason, and MSc Sergej Seepma for supervising me throughout this project and Sergej for supervising me during the laboratory experiments as well as independently providing more results. I am extremely grateful for all the time and effort you have given towards this project. I would also like to thank Dr. Adam Hill for helping me understand the theory behind CG as well as the time spent critiquing my work to make sure the CG background was well described and explained. Also thank you to Prof. Michael Anderson for aiding Dr. Hill with problems we came across during simulations.

References

Alpers, C. N., Jambor, J. L., & Nordstrom, D. (Eds.). (2018). Sulfate minerals: crystallography, geochemistry, and environmental significance (Vol. 40). Walter de Gruyter GmbH & Co KG.

Anand, R. R., & Paine, M. (2002). Regolith geology of the Yilgarn Craton, Western Australia: implications for exploration. Australian Journal of Earth Sciences, 49(1), 3-162.

Anderson, M. W., Gebbie-Rayet, J. T., Hill, A. R., Farida, N., Attfield, M. P., Cubillas, P., ... & Gale, J. D. (2017). Predicting crystal growth via a unified kinetic three-dimensional partition model. Nature, 544(7651), 456-459.

Antao, S. M. (2012). Structural trends for celestite (SrSO4), anglesite (PbSO4), and barite (BaSO4): Confirmation of expected variations within the SO4 groups. American Mineralogist, 97(4), 661-665.

Basavarajappa, H. T., Manjunatha, M. C., Rajendran, S., & Jeevan, L. (2017). Determination of Spectral Characteristics on Archaean Komatiites in Ghattihosahalli Schist Belt (Gsb) of Kumminagatta, Chitradurga District, Karnataka, India. International Journal, 6(1), 2416-2423.

Blake, R. E., Chang, S. J., & Lepland, A. (2010). Phosphate oxygen isotopic evidence for a temperate and biologically active Archaean ocean. Nature, 464(7291), 1029-1032.

Boon, M., & Jones, F. (2016). Barium sulfate crystallization from synthetic seawater. Crystal Growth & Design, 16(8), 4646-4657.

Bosbach, D., Hall, C., & Putnis, A. (1998). Mineral precipitation and dissolution in aqueous solution: in-situ microscopic observations on barite (001) with atomic force microscopy. Chemical Geology, 151(1-4), 143-160.

Bracco, J. N., Gooijer, Y., & Higgins, S. R. (2016). Hydrothermal atomic force microscopy observations of barite step growth rates as a function of the aqueous barium-to-sulfate ratio. Geochimica et Cosmochimica Acta, 183, 1-13.

Busigny, V., Marin-Carbonne, J., Muller, E., Cartigny, P., Rollion-Bard, C., Assayag, N., & Philippot, P. (2017). Iron and sulfur isotope constraints on redox conditions associated with the 3.2 Ga barite deposits of the Mapepe Formation (Barberton Greenstone Belt, South Africa). Geochimica Et Cosmochimica Acta, 210, 247-266.

Canet, C., Anadón, P., González-Partida, E., Alfonso, P., Rajabi, A., Pérez-Segura, E., & Alba-Aldave, L. A. (2014). Paleozoic bedded barite deposits from Sonora (NW Mexico): Evidence for a hydrocarbon seep environment of formation. Ore Geology Reviews, 56, 292-300.

Catling, D. C., & Zahnle, K. J. (2020). The Archean atmosphere. Science Advances, 6(9), eaax1420.

De Ronde, C. E., & de Wit, M. J. (1994). Tectonic history of the Barberton greenstone belt, South Africa: 490 million years of Archean crustal evolution. Tectonics, 13(4), 983-1005.

De Ronde, C. E., Channer, D. M. D., Faure, K., Bray, C. J., & Spooner, E. T. (1997). Fluid chemistry of Archean seafloor hydrothermal vents: Implications for the composition of circa 3.2 Ga seawater. Geochimica et Cosmochimica Acta, 61(19), 4025-4042.

Devaraju, T. C., Raith, M. M., & Spiering, B. (1999). Mineralogy of the Archean barite deposit of Ghattihosahalli, Karnataka, India. The Canadian Mineralogist, 37(3), 603-617.

Gustafsson, J. P. (2013). Visual MINTEQ version 3.1, department of sustainable development. Environmental Science and Engineering, KTH, Stockholm.

Gwiazda, R. H., Paull, C. K., Caress, D. W., Preston, C. M., Johnson, S. B., Lundsten, E. M., & Anderson, K. (2019). The Extent of Fault-Associated Modern Authigenic Barite Deposits Offshore Northern Baja California Revealed by High-Resolution Mapping. Frontiers in Marine Science.

Habicht, K. S., Gade, M., Thamdrup, B., Berg, P., & Canfield, D. E. (2002). Calibration of sulfate levels in the Archean ocean. Science, 298(5602), 2372-2374.

Hanor, J. S. (2000). Barite–celestine geochemistry and environments of formation. Reviews in Mineralogy and Geochemistry, 40(1), 193-275.

Heinrichs, T. K., & Reimer, T. (1977). A sedimentary barite deposit from the Archean Fig Tree Group of the Barberton Mountain Land (South Africa). Economic Geology, 72(8), 1426-1441.

Hill, A. R. (2018). Modelling Crystal Growth with Natural Tiles. Unpublished Doctoral Thesis. University of Manchester.

Jacobsen, S. D., Smyth, J. R., Swope, R. J., & Downs, R. T. (1998). Rigid-body character of the SO~ 4 groups in celestine, anglesite and barite. Canadian mineralogist, 36, 1053-1060.

Jayananda, M., Duraiswami, R. A., Aadhiseshan, K. R., Gireesh, R. V., Prabhakar, B. C., Kafo, K. U., ... & Namratha, R. (2016). Physical volcanology and geochemistry of Palaeoarchaean komatiite lava flows from the western Dharwar craton, southern India: implications for Archaean mantle evolution and crustal growth. International Geology Review, 58(13), 1569-1595.

Judat, B., & Kind, M. (2004). Morphology and internal structure of barium sulfate—derivation of a new growth mechanism. Journal of Colloid and Interface Science, 269(2), 341-353.

Knauth, L. P., & Lowe, D. R. (2003). High Archean climatic temperature inferred from oxygen isotope geochemistry of cherts in the 3.5 Ga Swaziland Supergroup, South Africa. Geological Society of America Bulletin, 115(5), 566-580.

Krissansen-Totton, J., Arney, G. N., & Catling, D. C. (2018). Constraining the climate and ocean pH of the early Earth with a geological carbon cycle model. Proceedings of the National Academy of Sciences, 115(16), 4105-4110.

Kossel, W. "Zur theorie des kristallwachstums." Nachrichten von der Gesellschaft der Wissenschaften zu Göttingen, Mathematisch-Physikalische Klasse 1927 (1927): 135-143.

Kucher, M., Babic, D., & Kind, M. (2006). Precipitation of barium sulfate: experimental investigation about the influence of supersaturation and free lattice ion ratio on particle formation. Chemical Engineering and Processing: Process Intensification, 45(10), 900-907.

Kunugiza, K., Kato, Y., Kano, T., Takaba, Y., Kuruma, I., & Sohma, T. (1996). An Archaean tectonic model of the Dharwar craton, southern India: the origin of the Holenarasipur greenstone belt (Hussan district, Karnataka) and reinterpretation of the Sargur-Dharwar relationship. Journal of Southeast Asian Earth Sciences, 14(3-4), 149-160.

Lambert, I. B., Donnelly, T. H., Dunlop, J. S. R., & Groves, A. D. (1978). Stable isotopic compositions of early Archaean sulphate deposits of probable evaporitic and volcanogenic origins. Nature, 276(5690), 808-811.

Lehmann, H. P., Fuentes-Arderiu, X., & Bertello, L. F. (1996). Glossary of terms in quantities and units in Clinical Chemistry (IUPAC-IFCC Recommendations 1996). Pure and Applied Chemistry, 68(4), 957-1000.

Lowe, D. R., Drabon, N., & Byerly, G. R. (2019). Crustal fracturing, unconformities, and barite deposition, 3.26–3.23 Ga, Barberton Greenstone Belt, South Africa. Precambrian Research, 327, 34-46.

Macdonald, R. W. (1982). An examination of metal inputs to the Southern Beaufort Sea by disposal of waste barite in drilling fluid. Ocean Management, 8(1), 29-49.

Macfarlane, A. W., Danielson, A., & Holland, H. D. (1994). Geology and major and trace element chemistry of late Archean weathering profiles in the Fortescue Group, Western Australia: implications for atmospheric PO2. Precambrian Research, 65(1-4), 297-317.

Monnin, C., & Galinier, C. (1988). The solubility of celestite and barite in electrolyte solutions and natural waters at 25 C: A thermodynamic study. Chemical Geology, 71(4), 283-296.

Morris, A. W., & Riley, J. P. (1966). The bromide/chlorinity and sulphate/chlorinity ratio in sea water. In Deep sea research and oceanographic Abstracts. Elsevier, 13(4), 699-705.

Mukherjee, S., Ghosh, G., Das, K., Bose, S., & Hayasaka, Y. (2018). Geochronological and geochemical signatures of the granitic rocks emplaced at the north-eastern fringe of the Eastern Dharwar

Craton, South India: Implications for late Archean crustal growth. Geological Journal, 53(5), 1781-1801.

Muller, É., Philippot, P., Rollion-Bard, C., Cartigny, P., Assayag, N., Marin-Carbonne, J., ... & Sarma, D. S. (2017). Primary sulfur isotope signatures preserved in high-grade Archean barite deposits of the Sargur Group, Dharwar Craton, India. Precambrian Research, 295, 38-47.

Nabhan, S., Marin-Carbonne, J., Mason, P. R., & Heubeck, C. (2020). In situ S-isotope compositions of sulfate and sulfide from the 3.2 Ga Moodies Group, South Africa: A record of oxidative sulfur cycling. Geobiology.

Nijman, W., & Valkering, M. E. (1998). Growth fault control of Early Archaean cherts, barite mounds and chert-barite veins, North Pole Dome, Eastern Pilbara, Western Australia. Precambrian Research, 88(1-4), 25-52.

Patel, A. R., & Koshy, J. (1968). Cleavage and etching of barite. The Canadian Mineralogist, 9(4), 539-546.

Pavlov, A. A., & Kasting, J. F. (2002). Mass-independent fractionation of sulfur isotopes in Archean sediments: strong evidence for an anoxic Archean atmosphere. Astrobiology, 2(1), 27-41.

Pina, C. M., Becker, U., Risthaus, P., Bosbach, D., & Putnis, A. (1998). Molecular-scale mechanisms of crystal growth in barite. Nature, 395(6701), 483-486.

Riedinger, D. J. (2020). Barite nucleation-Measuring effects of solution stoichiometry on crystal population and critical nuclei size (Master's thesis).

Risthaus, P., Bosbach, D., Becker, U., & Putnis, A. (2001). Barite scale formation and dissolution at high ionic strength studied with atomic force microscopy. Colloids and Surfaces A: Physicochemical and Engineering Aspects, 191(3), 201-214.

Roerdink, D. L., Mason, P. R., Farquhar, J., & Reimer, T. (2012). Multiple sulfur isotopes in Paleoarchean barites identify an important role for microbial sulfate reduction in the early marine environment. Earth and Planetary Science Letters, 331, 177-186.

Roerdink, D. L., Mason, P. R., Whitehouse, M. J., & Brouwer, F. M. (2016). Reworking of atmospheric sulfur in a Paleoarchean hydrothermal system at Londozi, Barberton Greenstone Belt, Swaziland. Precambrian Research, 280, 195-204.

Sánchez-Pastor, N., Pina, C. M., Fernández-Díaz, L., & Astilleros, J. M. (2006). The effect of CO32-on the growth of barite {0 0 1} and {2 1 0} surfaces: An AFM study. Surface Science, 600(6), 1369-1381.

Schlegel, T. U., Wagner, T., Wälle, M., & Heinrich, C. A. (2018). Hematite breccia-hosted iron oxide copper-gold deposits require magmatic fluid components exposed to atmospheric oxidation: evidence from Prominent Hill, Gawler Craton, South Australia. Economic Geology, 113(3), 597-644.

Schwarzer, H. C., & Peukert, W. (2002). Experimental investigation into the influence of mixing on nanoparticle precipitation. Chemical engineering & technology, 25(6), 657-661.

Stack, A. G., Raiteri, P., & Gale, J. D. (2012). Accurate rates of the complex mechanisms for growth and dissolution of minerals using a combination of rare-event theories. Journal of the American Chemical Society, 134(1), 11-14.

Sugitani, K., Mimura, K., Suzuki, K., Nagamine, K., & Sugisaki, R. (2003). Stratigraphy and sedimentary petrology of an Archean volcanic–sedimentary succession at Mt. Goldsworthy in the Pilbara Block, Western Australia: implications of evaporite (nahcolite) and barite deposition. Precambrian Research, 120(1-2), 55-79.

Suito, E., & Takiyama, K. (1952). Morphology of Barium Sulfate Precipitate by Electron Microscope. Proceedings of the Japan Academy, 28(3), 133-138.

Uchida, A., Toyoda, S., & Ishibashi, J. (2012). Radon loss from barite in submarine hydrothermal sulfide deposits. AGUFM, 2012, OS13A-1708.

van Kranendonk, M. J., & Pirajno, F. (2004). Geochemistry of metabasalts and hydrothermal alterat*ion zones associated with c. 3.45 Ga chert and barite deposits: implications for the geological setting

of the Warrawoona Group, Pilbara Craton, Australia. Geochemistry: Exploration, Environment, Analysis, 4(3), 253-278.

Vital, M., Daval, D., Morvan, G., Martinez, D. E., & Heap, M. J. (2020). Barite Growth Rates as a Function of Crystallographic Orientation, Temperature, And Solution Saturation State. Crystal Growth & Design, 20(6), 3663-3672.

Weber, J., Bracco, J. N., Poplawsky, J. D., Ievlev, A. V., More, K. L., Lorenz, M., ... & Stack, A. G. (2018). Unraveling the effects of strontium incorporation on barite growth—In situ and ex situ observations using multiscale chemical imaging. Crystal Growth & Design, 18(9), 5521-5533.

Widanagamage, I. H., Waldron, A. R., & Glamoclija, M. (2018). Controls on barite crystal morphology during abiotic precipitation. Minerals, 8(11), 480.